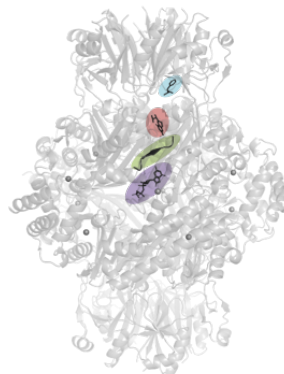


DISSERTATION

ZUR ERLANGUNG DES DOKTORGRADES
DER NATURWISSENSCHAFTEN

Using hybrid approaches to study the allosteric regulation of GTP Cyclohydrolase I



Vorgelegt beim Fachbereich 14

Biochemie, Chemie und Pharmazie
der Johann Wolfgang Goethe - Universität
in Frankfurt am Main

Eingereicht von:

Rebecca Ebenhoch

aus Biberach

Biberach, November 2020

Vom Fachbereich Biochemie, Chemie und Pharmazie der Johann Wolfgang Goethe-Universität als Dissertation angenommen.

Dekan:	Prof. Dr. Clemens Glaubitz
Gutachter:	Prof. Dr. Stefan Knapp
Zweitgutachter:	Prof. Dr. Robert Tampé

Datum der Disputation:

The research reported in this thesis was carried out at at the Medicinal Chemistry Department (Structural Research Group) at Boehringer Ingelheim Pharma GmbH & Co. KG under supervision of Dr. Herbert Nar, Dr. Alexander Pautsch and Dr. Martin Lenter. University supervision and examination was conducted by Prof. Dr. Stefan Knapp & Prof. Dr. Robert Tampé.

Declaration

Except where stated otherwise by reference or acknowledgment, the work presented was generated by myself under the supervision of my advisors during my doctoral studies. All contributions from colleagues are explicitly referenced in the thesis. The material listed below was obtained in the context of collaborative research:

Figure 21: hGFRP-FL-NHis overexpression, lysis and purification. (Figures generated by Lisa Weixler under supervision of Rebecca Ebenhoch)

Figure 22: Overexpression, lysis and purification of hGCH1-D42-NHis construct. (Figures generated by Lisa Weixler under supervision of Rebecca Ebenhoch)

Figure 23: Overexpression, lysis and purification of hGCH1-FL-NMBP construct. (Figures generated by Lisa Weixler under supervision of Rebecca Ebenhoch)

Figure 37: KD determination of 7-deaza-GTP using protein NMR. (NMR experiments performed by Markus Zeeb, Martin Rübhelke and Robert Meinecke)

Figure 38: Determination of binding kinetics using STD-NMR. (NMR experiments performed by Markus Zeeb, Martin Rübhelke and Robert Meinecke)

Whenever a figure or table is identical to a previous publication, it is stated explicitly in the thesis that copyright permission and/or co-author agreement has been obtained. The following parts of the thesis have been previously published:

Figure 26: Relevant structural features on GCH1. (Published November 2020 [21])

Figure 29: Overview of the architecture of the GCH1-GFRP complex and details of the EM maps of the stimulatory and inhibitory complexes. (Published November 2020 [21])

Figure 30: Details of the stimulatory and inhibitory EM structures reveal dramatic quaternary conformational changes and order-disorder transitions. (Published November 2020 [21])

Figure 31: Overall conformational changes upon binding of compounds. (Published November 2020 [21])

Figure 32: Details of conformational rearrangement upon binding of AXSP0056BS to GCH1. (Published November 2020 [21])

Figure 37: KD determination of 7-deaza-GTP using protein NMR. (Published November 2020 [21])

Figure 38: Determination of binding kinetics using STD-NMR. (Published November 2020 [21])

Chapter 3.3.1: Determination of hGCH-hGFRP complexes by cryo-EM. (Published November 2020 [21])

Chapter 3.3.2: hGCH1 crystal structures. (Published November 2020 [21])

Chapter 3.4: GCH mutagenesis study. (Published November 2020 [21])

Chapter 3.5: Determination of binding affinities and kinetics using STD-NMR. (Published November 2020 [21])

Chapter 4.9: Combination of cryo-EM and Xray structures help to develop a model of allosteric inhibition. (Published November 2020 [21])

Chapter 4.10: Novel dissociations rate controlled allosteric inhibition of GCH1. (Published November 2020 [21])

(signature:)

(place, date:)

List of publications

The publications which were generated in the context of this dissertation are marked with a *. In written form only the research on GCH1 is shown here, these are marked with a **.

Crystal structure and receptor-interacting residues of MYDGF - a protein mediating ischemic tissue repair*

Authors: **Rebecca Ebenhoch**, Abbas Akhdar, Marc R. Reboll, Mortimer Korf-Klingebiel, Priyanka Gupta, Julie Armstrong, Yining Huang, Lee Frego, Irina Rybina, John Miglietta, Anton Pekcec, Kai C. Wollert, Herbert Nar

Status: published on 26.11.2019 at *Nature Communications*

Contribution: First author, all experiments (besides activity data) planned, performed and all figures generated.

A hybrid approach reveals the allosteric regulation of GTP cyclohydrolase I**

Authors: **Rebecca Ebenhoch**, Simone Prinz, Susann Kaltwasser, Deryck J. Mills, Robert Meinecke, Martin Rübhelke, Dirk Reinert, Margit Bauer, Lisa Weixler, Markus Zeeb, Janet Vonck, Herbert Nar

Status: published on 23.11.2020 at *PNAS*

Contribution: First author, all experiments (besides NMR experiments) planned, performed and all figures generated.

Biophysical and structural investigation of the regulation of human GTP Cyclohydrolase I by GFRP**

Authors: **Rebecca Ebenhoch**, Margit Bauer, Dirk Reinert, Anja Kersting, Sylwia Huber, Angela Schmid, Ingo Hinz, Marisa Feiler, Kathrin Müller, Herbert Nar

Status: submitted on 20.10.2020 to *Journal of Structural Biology*; The reviewers have proposed only minor changes to the text

Contribution: First author, all experiments planned, performed and all figures generated.

Antibody recognition of the GARP-latTGF β complex*

Authors: Frederik Igney, **Rebecca Ebenhoch**, Felix Schiele, Herbert Nar

Status: Manuscript under preparation.

Contribution: Second author, Cryo-EM structures of the GARP-latTGF β .

Structural insights into phospho-regulation, nucleotide binding and control of intracellular ion access of K-Cl cotransporters

Authors: Gamma Chi; **Rebecca Ebenhoch**; Henry Man; Haiping Tang; Laurence E. Tremblay; Gabriella Reggiano; Xingyu Qiu; Tina Bohstedt; Idir Liko; Fernando G. Almeida; Alexandre P. Garneau; Dong Wang; McKinley Gavin; Patrizia Abrusci; Shubhashish M.M. Mukhopadhyay; Alejandra Fernandez-Cid; Samira Slimani; Julie L. Lavoie; Nicola Burgess-Brown; Ben Tehan; Frank DiMaio; Ali Jazayeri; Paul Isenring; Carol V. Robinson; Katharina Luise Duerr

Status: submitted on 02.10.2020 to *Cell*

Contribution: Shared first authorship, KCC1 cryo-EM structure.

Crystal structures hKHK-C, hKHK-A and mKHK-C provide a structural basis for species- and isoform-selective inhibitor design

Authors: **Rebecca Ebenhoch**, Margit Bauer, Helmut Romig, Dirk Gottschling, Jörg Kley, Niklas Heine, Alexander Weber, Ingo Uphues, Herbert Nar, Alexander Pautsch

Status: Manuscript ready for submission.

Contribution: First author, all experiments planned, performed and all figures generated.

Structural and Functional Features of the Reovirus sigma 1 Tail

Authors: Melanie Dietrich, Kristen Ogden, Jacob Long, Rebecca Ebenhoch, Alexandra Thor, Terence Dermody, Thilo Stehle

Status: published on 15.07.2018 at *Journal of Virology*

Contribution: Experimental phasing and structure solution of the sigma 1 Tail domain.

Summary

GTP Cyclohydrolase I (GCH1) is a homodecameric protein complex of approximately 270 kDa molecular weight. GCH1 catalyses the conversion of guanosine triphosphate (GTP) to dihydroneopterin triphosphate (H₂NTP), the initiating step in the biosynthesis of tetrahydrobiopterin (BH₄). BH₄ functions as a co-factor in neurotransmitter biosynthesis.

The BH₄ biosynthesis pathway and GCH1 have been identified as promising targets to treat pain disorders in patients. The function of mammalian GCH1 is regulated by a metabolic sensing mechanism involving a regulator protein, GCH1 feedback regulatory protein (GFRP). GFRP forms a pentamer of five 10-kDa subunits, which binds to GCH1 to form inhibitory or stimulatory complexes dependent on availability of co-factor ligands, BH₄ and phenylalanine, respectively.

Since the modulation of GCH activity is a very promising approach in the treatment of pain patients, research on GCH1 has been going on for over 20 years. However, previous studies, which have mostly worked with bacterial or rat protein, could not conclusively explain the mechanism of allosteric regulation [65]. The work presented here shows for the first time structures of human GCH1-GFRP complexes, structures of human GFRP and numerous human GCH1 structures in different ligand-induced states and sets a milestone in the study of human GCH1 and the understanding of the complex allosteric regulation through analysis with numerous orthogonal structural and biophysical methods.

We determined high resolution structures of human hGCH1-hGFRP complexes by cryo-EM. Cryo-EM revealed structural flexibility of specific and relevant surface lining loops, which were unresolved by X-ray crystallography due to crystal packing. In particular, loop F122, which is located directly above the substrate-binding site, is well ordered in the active, stimulatory complex, while it offers enhanced flexibility in the inhibitory GCH1-GFRP complex. The overall resolution of the cryo-EM structures of 2.9 and 3.0 Å allows for visualization of ligand binding to

functional sites of the regulated complexes.

Further, we studied the allosteric regulation of isolated hGCH1 and hGFRP and the ligand bound complexes by X-ray crystallography. We observed a crystal structure of the apo GCH1 enzyme and a co-structure of GCH1 in an active, substrate analog 7-deaza-GTP bound state. We further determined structures of GCH in presence of allosteric inhibitors, of which one structure shows a non-fully occupied intermediate state, while another structure resolves a state, in which all allosteric sites are occupied by an inhibitor. Additionally this work shows the structures of the inhibitory and stimulatory hGCH1-hGFRP complex in presence of the substrate analogue 8-oxo-GTP. Contrary to the published hypotheses [65], we can show that the recognition of the substrate in the active and inhibited state is indifferent and therefore cannot be the cause of the reduced activity.

Using the combined structural information, obtained by Cryo-EM and X-ray crystallography, we are able to generate a comprehensive picture of the mechanism of allosteric regulation: Local rearrangements in the allosteric pocket upon BH4 binding result in drastic changes in the quaternary structure of the enzyme leading to a more compact, tense form of the inhibited protein and translocate to the active site, leading to an open, more flexible structure of its surroundings. Inhibition of the enzymatic activity is not a result of hindrance of substrate binding, but rather a consequence of accelerated substrate binding kinetics as shown by STD-NMR and site-directed mutagenesis. We propose a novel kinetically controlled mechanism of allosteric inhibition that prevents substrate conversion by reducing the residence time of the substrate in the active site below the time required for substrate conversion.

In addition to the already published structure of rat GFRP, we were able to solve the first human GFRP structures in the presence and absence of phenylalanine. The binding of phenylalanine induces conformational changes in the region of GFRP

that is responsible for the recognition of GCH1. Comparison with stimulatory GCH1-GFRP structures suggest, that the observed conformational changes are induced solely by the binding of phenylalanine. In general, GFRP appears to be a very stable protein, showing only minor changes in loop 37-45 upon binding of GCH1. This is in line with the discussed role of GFRP as scaffolding protein.

Further the elaborate SPR analysis, together with the structural data, show that the two proteins hGFRP and hGCH1 only have affinity to each other, in presence of effector molecules. In the presence of the small molecules BH4 and phenylalanine, the two proteins have picomolar affinity to each other, while the complex falls apart when this small molecule is removed. This small molecule induced association and dissociation of the GCH1-GFRP complex is extremely rapid. Thus, the effector molecules BH4 and phenylalanine act as molecular glues facilitating high-affinity recognition of two proteins.

These observations strengthen the hypothesis of GFRP's role as a metabolic sensor protein that functions as a scaffolding protein by either stabilizing the apo or BH4 bound states of GCH1. The stabilization of the inactive state of GCH1 in the presence of GFRP causes an increase of BH4 affinity and a boost of its inhibitory potency. This supports GFRP's biological role as metabolic sensor and enables rapid and effective modulation of GCH's activity.

This work also includes the characterization of allosteric small molecules, which were identified in the course of an FBS in the run-up to this work. Binding of the fragments to GCH was previously determined by NMR.

Enzymatic data generated here clearly show, that some compounds have an inhibitory effect, while others do not have an influence on enzyme activity. In addition, we were able to analyze the formation of the GCH1-GFRP complex using DSF. The inhibitory compounds, analogous to BH4, induce the complex formation, while the inactive fragments do not form a GCH1-GFRP complex.

Crystal structures of this fragments reveal the binding mode and therefore help to

understand the mode of action of these compounds. Here, the formation of a salt bridge between Arg235 and Asp127 is prevented by sterically demanding fragments, thus disturbing the integrity of the inhibitory conformation.

In summary, we were able to distinguish between binders and inhibitory fragment-like molecules. This generates promising starting points for the development of positive and negative GCH1 modulators and could lead to the development of drugs that control BH4 homeostasis.

Contrary to the in-vivo studies showing that, the N-terminal peptide of hGCH is an autoinhibitory control element and contributes to binding the allosteric regulatory protein GFRP [41, 42, 110], the here presented work shows using SPR and classical enzyme kinetics, that in-vitro enzymatic activity and the binding affinity and kinetics are indifferent in full-length and $\Delta 42$ -hGCH1.

BH4 is involved as an essential cofactor for the aromatic amino acid hydroxylases, which catalyze the conversion of L-phenylalanine to L-tyrosine, L-tyrosine to L-DOPA and L-tryptophan to 5-hydroxy-L-tryptophan [47]. So far, it was known that phenylalanine can bind to GFRP, which triggers the formation of the stimulatory complex and thereby leads to a reduction in cooperativity and thereby to an increase in the activity of GCH1. It was unknown whether other aromatic amino acids like tyrosine or tryptophan also address the same feedback mechanism and can bind GFRP, allow formation of GCH1-GFRP complexes and thus stimulate GCH1. In this study we show by DSF experiments that the stimulatory complex is only formed in presence of phenylalanine but not upon addition of tyrosine or tryptophan. Therefore, feedback stimulation seems to be exclusively triggered by phenylalanine.

In conclusion, this comprehensive structural and biophysical study shows GCH1 in an ensemble of compound and regulator protein induced states from active to inactive and thereby provides insights into the mechanism of allosteric regulation

of GCH1 in presence and absence of GFRP in unprecedented detail.

Therefore, this work contributes immensely to the general understanding of allosteric proteins. Since the BH4 pathway is currently perceived as an attractive target to treat pain disorders [53, 75, 114] with GCH1 being the target with human genetics validation, the understanding of the details of allosteric GCH1 inhibition as well as the methods used here will prove highly useful to identify potential drug candidates that selectively modulate its activity.

To our knowledge, no mechanism of allosteric inhibition has been postulated which is kinetically controlled and reduces the substrate retention time in the active pocket below the time required for substrate conversion. Therefore, this work contributes immensely to the general understanding of allosteric proteins and has the potential to stimulate further studies to explore allosteric mechanisms.

Zusammenfassung

GTP Cyclohydrolase I (GCH1) ist ein homodekamerischer Proteinkomplex mit einem Molekulargewicht von etwa 270 kDa. GCH1 katalysiert die Umwandlung von Guanosintriphosphat (GTP) in Dihydroneopterintriphosphat (H₂NTP), den ersten Schritt in der Biosynthese von Tetrahydrobiopterin (BH₄). BH₄ fungiert als Co-Faktor in der Neurotransmitter-Biosynthese.

Der BH₄-Biosyntheseweg und GCH1 wurden als vielversprechende Ansatzpunkte für die Behandlung von Schmerzerkrankungen bei Patienten identifiziert. Die Aktivität von GCH1 in Säugetieren wird durch einen metabolischen Sensormechanismus reguliert, an dem ein Regulatorprotein, das GCH1 Feedback Regulatory Protein (GFRP), beteiligt ist.

GFRP ist ein Pentamer aus 10-kDa-Untereinheiten, welches an GCH1 bindet und in Abhängigkeit von der Verfügbarkeit von Co-Faktor-Liganden, BH₄ bzw. Phenylalanin, inhibierte oder aktivierte Komplexe bildet.

Da die Modulation der GCH Aktivität ein sehr vielversprechender Ansatz bei der Therapie von Schmerzpatienten ist, wird an GCH1 seit über 20 Jahren geforscht. Diese Studien, welche meist mit Bakteriellen oder Ratten Protein gearbeitet haben, konnten den Mechanismus der allosteren Regulation allerdings nicht schlüssig erklären [65]. Die hier dargelegte Arbeit zeigt zum ersten mal Strukturen der humanen GCH1-GFRP Komplexe, Strukturen des humanen GFRP und zahlreiche humane GCH1 Strukturen in unterschiedlichen Ligand induzierten Zuständen und setzt durch die Analyse mit zahlreichen orthogonalen strukturellen- und biophysikalischen Methoden einen Meilenstein in der Erforschung der humanen GCH1 und dem Verständnis der komplexen allosteren Regulation.

Wir konnten hochauflösende Strukturen von menschlichen hGCH1-hGFRP-Komplexen mittels Kryo-EM bestimmen. Die Kryo-EM zeigte die strukturelle Flexibilität spezifischer und relevanter Oberflächenstrukturen, die aufgrund der Kristallpackung durch die Röntgenkristallographie nicht aufgelöst werden konnten. Insbesondere der

Loop F122, der direkt über der Substratbindestelle sitzt, ist im aktiven, stimulierenden Komplex gut geordnet, während er im inhibitorischen GCH1-GFRP-Komplex eine erhöhte Flexibilität aufweist.

Die hohe Auflösung der Kryo-EM-Strukturen von 2,9 und 3,0 Å erlaubt zudem die Visualisierung der Ligandenbindung in der Substratbindetasche sowie in der allosteren Tasche der regulierten Komplexe.

Weiterhin wurde die allosterische Regulation von isoliertem hGCH1 und hGFRP und den ligandgebundenen Komplexen mittels Röntgenkristallographie untersucht. Wir konnten eine Kristallstruktur des apo-GCH1-Enzyms und eine Co-Struktur von GCH1 in einem aktiven, substratanalogen 7-Deaza-GTP-gebundenen Zustand generieren.

Zudem konnten wir Strukturen von GCH in Gegenwart von allosterischen Inhibitoren lösen, von denen eine Struktur einen nicht vollständig besetzten Zwischenzustand zeigt, während eine andere Struktur den Zustand auflöst, in dem alle allosterischen Stellen von einem Inhibitor-Molekül besetzt sind.

Des Weiteren werden im Rahmen dieser Arbeit auch Strukturen vom inhibitorischen und stimulatorischen hGCH1-hGFRP Komplex in Anwesenheit von dem Substratanalog 8-oxo-GTP gezeigt. Im Gegensatz zu den Thesen anderer publizierten Studien [65], können wir hier zeigen, dass die Erkennung des Substrats im aktiven und inhibierten Zustand indifferent ist und somit nicht Ursache der verminderten Aktivität sein kann.

Durch Kombination der diversen strukturellen Informationen, die wir mittels Cryo-EM und Röntgenkristallographie gewonnen haben, sind wir in der Lage, ein umfassendes Bild des Mechanismus der allosterischen Regulation zu formen: Lokale Umlagerungen in der allosterischen Tasche bei der BH4-Bindung führen zu drastischen Veränderungen in der quaternären Struktur des Enzyms, die zu einer kompakteren, gespannten Form des inhibierten Proteins führen und an das aktive Zentrum translozieren, was dort lokal zu einer offenen, flexibleren Umgebung führt. Die Hemmung der enzymatischen Aktivität ist nicht eine Folge der Blockierung

der Substratbindung, sondern vielmehr eine Folge der beschleunigten Substratbindungskinetik. Dies wurde durch durch STD-NMR und Mutagenese Studien gezeigt. Mittels STD-NMR sehen wir indifferente KDs für das Substrat im inhi- bierten und aktiven Protein aber eine starke Beschleunigung der Bindekinetik für den inhibierten Zustand.

Wir schlagen einen neuartigen kinetisch kontrollierten Mechanismus der allosterischen Hemmung vor, der die Substratumwandlung verhindert, indem die Verweilzeit des Substrats im aktiven Zentrum unter die für die Substratumwandlung erforderliche Zeit herabsetzt.

Zusätzlich zu der bereits publizierten Struktur des GFRP 's der Ratte, konnten wir die ersten humanen GFRP Strukturen in An- und Abwesenheit von Phenylalanin lösen. Die Bindung von Phenylalanin induziert Konformationsänderung in dem Bereich von GFRP, welcher für die Erkennung von GCH1 zuständig ist. Daraufhin haben wir die Komplementarität der Oberflächen von den unterschiedlichen apo und Ligand gebundenen GCH und GFRP Strukturen verglichen. Der Vergleich mit GCH1-GFRP-Strukturen legt nahe, dass die beobachteten Konformationsänderungen allein durch die Bindung von Phenylalanin induziert werden.

Im Allgemeinen scheint GFRP ein sehr stabiles Protein zu sein, das nur geringe Veränderungen im Loop 37-45 bei Bindung von GCH1 zeigt. Dies steht im Einklang mit der diskutierten Rolle von GFRP als Gerüstprotein.

Weiter zeigt die SPR-Analyse zusammen mit den Strukturdaten, dass die beiden Proteine, hGFRP und hGCH1, nur in Gegenwart von Effektormolekülen Affinität zueinander besitzen. In Anwesenheit der Kleinmoleküle BH4 und Phenylalanin besitzen die beiden Proteine picomolare Affinität zueinander, während der Komplex bei Entzug dieses Kleinmoleküls schlagartig auseinanderfällt.

Diese durch Kleinmoleküle induzierte Assoziation und Dissoziation des GCH1-GFRP-Komplexes verläuft extrem schnell. So wirken die Effektormoleküle BH4 und Phenylalanin als molekulare Klebstoffe, die eine hochaffine Erkennung zweier Proteine ermöglichen.

Diese Beobachtungen bestärken die Hypothese der Rolle von GFRP als metabolisches Sensorprotein, das als Gerüstprotein fungiert, indem es entweder die apo- oder BH4-gebundenen Zustände von GCH1 stabilisiert. Die Stabilisierung des inaktiven Zustands von GCH1 in Gegenwart von GFRP bewirkt eine Erhöhung der BH4-Affinität und eine Steigerung seiner Hemmwirkung.

Dies unterstützt die biologische Rolle von GFRP als Stoffwechselsensor und ermöglicht eine schnelle und effektive Modulation der Aktivität von GCH.

Diese Arbeit umfasst zudem die Charakterisierung allosterer Kleinmoleküle, welche im Rahmen eines FBS im Vorlauf dieser Arbeit identifiziert wurden. Die Bindung der Fragmente an GCH wurde zuvor über NMR nachgewiesen.

Die hier generierten enzymatischen Daten zeigen deutlich, dass einige Verbindungen inhibitorisch wirken, während andere keinen Einfluss auf die Enzymaktivität haben. Zudem konnten wir mittels DSF die Bildung des GCH1-GFRP Komplexes analysieren. Die Substanzen, welche analog zu BH4 inhibitorisch wirken, induzieren die Komplexbildung, während die inaktiven Fragmente keinen GCH1-GFRP Komplex formen.

Außerdem konnten wir mittels Kristallstrukturen den Wirkungsmechanismus dieser Verbindungen erklären. Hier wird die Ausbildung einer Salzbrücke zwischen Arg235 und Asp127 durch steirisch anspruchsvolle Fragmente unterbunden und somit die Integrität der inhibitorischen Konformation gestört.

Zusammenfassen waren in der Lage, zwischen Bindern und inhibitorischen fragmentartigen Molekülen zu unterscheiden. Dies liefert vielversprechende Ansatzpunkte für die Entwicklung positiver und negativer GCH1-Modulatoren und könnte zur Entwicklung von Medikamenten führen, die die BH4-Homöostase kontrollieren.

Die publizierten in-vivo-Studien zeigen, dass das N-terminale Peptid von hGCH ein autoinhibitorisches Kontrollelement ist und zur Bindung des allosterischen regulatorischen Proteins GFRP [41, 42, 110] beiträgt.

Im Gegensatz dazu zeigt die hier vorgestellte Arbeit, dass die in-vitro-enzymatische

Aktivität und die Bindungsaffinität und -kinetik des Vollängenproteins und den verkürzten $\Delta 42$ -hGCH1 Proteins indifferent sind. Dies wurde mittels enzymatischen und SPR basierten Methoden gezeigt.

BH4 ist als wesentlicher Co-Faktor für die aromatischen Aminosäure-Hydroxylasen beteiligt, die die Umwandlung von L-Phenylalanin zu L-Tyrosin, L-Tyrosin zu L-DOPA und L-Tryptophan zu 5-Hydroxy-L-Tryptophan [47] katalysieren. Bislang war bekannt, dass Phenylalanin an GFRP binden kann, was die Bildung des stimulierten Komplexes triggert und dadurch zu einer Verminderung der Kooperativität und damit zu einer Erhöhung der Aktivität von GCH1 führt. Es war unbekannt, ob auch andere aromatische Aminosäuren wie Tyrosin oder Tryptophan den gleichen Feedbackmechanismus ansprechen und GFRP binden, die Bildung von GCH1-GFRP-Komplexen ermöglichen und damit GCH1 stimulieren können. In dieser Studie zeigen wir durch DSF-Experimente, dass der stimulierte Komplex nur in Gegenwart von Phenylalanin, nicht aber bei Zugabe von Tyrosin oder Tryptophan gebildet wird. Daher scheint die Feedback-Stimulation ausschließlich durch Phenylalanin ausgelöst zu werden.

Zusammenfassend lässt sich sagen, dass diese umfassende strukturelle und biophysikalische Studie GCH1 in einem vollständigen Ensemble von Compound- und Regulatorprotein induzierten Zuständen von aktiv zu inaktiv zeigt und dadurch Einblicke in den Mechanismus der allosterischen Regulation von GCH1 in An- und Abwesenheit von GFRP in noch nie dagewesener Detailliertheit gewährt.

Der BH4-Signalweg wird derzeit als attraktives Ziel für die Behandlung von Schmerz-erkrankungen [53, 75, 114] angesehen. Zudem ist GCH1 ein Target mit human-genetischer Validierung, daher ist das hierdurch gewonnene Verständnis über die allosterische Inhibition von hGCH, sowie die hier angewandten Methoden sehr nützlich, um potenzielle Arzneimittelkandidaten zu identifizieren, welche die Aktivität von hGCH selektiv modulieren können.

Außerdem wurde bislang noch kein Mechanismus der Allostereninhibitopn postuliert, welcher kinetisch kontrolliert ist und die Substrat verweildauer in der

Aktiven Tasche unter die benötigte Zeit für die Substratumsetzung herabsetzt. Daher trägt diese Arbeit ungemein zum generellen Verständnis allosterer Proteine bei und hat das Potential weitere Studien zur Erforschung allosterer Mechanismen anzuregen.

Contents

1	Introduction	1
1.1	GTP-cyclohydrolase 1	1
1.2	GCH1 structural features	1
1.2.1	Monomer structure	1
1.2.2	Tertiary structure	2
1.2.3	Active site location, architecture and substrate binding . . .	3
1.2.4	GCH1 Reaction mechanism	5
1.2.5	GCH1 sequential conservation	6
1.3	GCH1 therapeutic interest	6
1.4	GCH1 regulation	7
1.4.1	PTMs and N-terminus modulate GCH1's activity	7
1.4.2	GFRP dependent allosteric regulation by BH4 and Phenylalanine	8
1.4.3	GFRP and GFRP-GCH1 structural features	9
1.5	Allosteric sites on GCH1 and GFRP	10
1.6	Previous structural studies and knowledge on allosteric regulation .	11
1.7	Objectives	14
2	Methods	17
2.1	Protein Characterization and Biochemical Methods	17
2.1.1	Discontinuous SDS-polyacrylamide gel electrophoresis (SDS-PAGE)	17
2.1.2	Determination of protein concentration	17
2.1.3	Mass spectrometry	17
2.1.4	N-terminal Sequencing	18
2.1.5	Enzyme kinetic assay	18
2.2	Protein production	19
2.2.1	Molecular Cloning	19
2.2.2	Site-Directed Mutagenesis	19
2.2.3	Transformation of chemically competent <i>E. coli</i> cells by heat shock	20

2.2.4	Expression and lysis	21
2.2.5	Expression and lysis of GFRP and GCH	21
2.2.6	Purification	23
2.3	Biophysical methods	26
2.3.1	Differential scanning fluorimetry	27
2.3.2	Surface plasmon resonance	29
2.3.3	Nuclear magnetic resonance spectroscopy	30
2.4	Crystallization	33
2.4.1	Crystal symmetry	33
2.4.2	Protein crystal growth	35
2.4.3	Crystallization and crystal optimization strategy	37
2.4.4	Soaking	39
2.4.5	Co-crystallization	40
2.4.6	Crystal freezing	40
2.5	X-ray crystallography	41
2.5.1	Data collection	41
2.5.2	Diffraction	42
2.5.3	Data processing	43
2.5.4	Calculating the electron density and MR Phasing	45
2.5.5	Structure refinement and ligand fitting	47
2.6	Single-particle cryo-electron microscopy	48
2.6.1	The Electron Microscope	49
2.6.2	Optical aberrations	55
2.6.3	Image and contrast formation	56
2.6.4	Sample preparation under cryo conditions	59
2.6.5	Single particle data processing	60
2.6.6	EM sample preparation for GCH1-GFRP complex	66
2.6.7	Data acquisition and processing of GCH1-GFRP EM datasets	66
3	Results	69
3.1	Expression, lysis and purification of hGCH and hGFRP proteins	69
3.1.1	hGFRP	69
3.1.2	Δ 42-hGCH1	72

3.1.3	Full-length GCH1	73
3.2	hGCH1-hGFRP complex formation	75
3.2.1	Optimization of the hGCH1-hGFRP complex	75
3.2.2	Formation and purification of the hGCH1-hGFRP complex	78
3.3	Structural studies	79
3.3.1	Determination of hGCH-hGFRP complexes by cryo-EM	80
3.3.2	hGCH1 crystal structures	89
3.3.3	X-ray structures of hGCH1-hGFRP ligand bound complexes	97
3.3.4	X-ray structures of hGFRP	102
3.4	GCH mutagenesis study	106
3.5	Determination of binding affinities and kinetics using NMR.	110
3.6	Formation of the stimulatory hGCH1-hGFRP complex upon binding of aromatic amino acids	113
3.7	SPR analysis of hGCH1-hGFRP complex formation	114
3.8	Role of GCH1's N-terminus on enzyme activity and complex formation	117
3.9	Small molecule effectors change conformations of GCH1 or GFRP	121
3.10	Characterization of allosteric binders	123
4	Discussion and Conclusions	127
4.1	Preparation of high quality proteins	127
4.2	Novel structures and hybrid approaches	127
4.3	Identification of allosteric binders and inhibitors	128
4.4	Stimulation of GCH1-GFRP is exclusively triggered by L-Phenylalanine	129
4.5	The N-terminus of hGCH1 does not influence hGFRP binding and enzymatic activity	129
4.6	Small molecule effectors facilitate pico-molar recognition of hGCH1 and hGFRP	131
4.7	GFRP acts as a scaffolding protein that sensitizes GCH1 to react to physiological levels of effector molecules BH4 and phenylalanine	132
4.8	Allosteric inhibition of GCH1-GFRP does not alter substrate recog- nition	133
4.9	Combination of cryo-EM and Xray structures help to develop a model of allosteric inhibition	134

4.10 Novel dissociation rate controlled allosteric inhibition of GCH1 . . .	135
4.11 Outlook and concluding words	139
Appendices	161
5 Curriculum Vitae	164
6 Acknowledgement/Danksagung	167

List of Figures

1	GCH1 catalysis the conversion of GTP to DHNTP	1
2	GCH1 monomer topology and quaternary structure	2
3	Active site and substrate recognition	4
4	Hypothetical mechanism of the reaction catalysed by GCH1	5
5	Positive and negative regulation of GCH1 by phenylalanine and BH4	8
6	GCH1-GFRP stimulatory and inhibitory complexes	9
7	Architecture of allosteric sites and effector molecule coordination	13
8	Principle of differential scanning fluorimetry.	28
9	The Surface plasmon resonance detection principle	30
10	Example of a 3-dimensional (triclinic) unit cell.	34
11	The 3-dimensional primitive crystal lattice systems.	34
12	Schematic figures of vapor diffusion based crystallization techniques.	36
13	Phase diagram describing the vapor diffusion experiment.	37
14	Bragg's law.	42
15	Ewald sphere and reflection condition.	43
16	Workflow of offline data-processing steps in autoPROC.	45
17	Scheme of a typically used TEM is shown with all essential components.	50
18	Most Important Aberrations for a TEM.	56
19	The effect of defocus.	58
20	3D reconstruction in real- and fourier space.	63
21	hGFRP-FL-NHis overexpression, lysis and purification	71
22	Overexpression, lysis and purification of hGCH1- Δ 42-NHis construct	73
23	Overexpression, lysis and purification of hGCH1-FL-NMBP construct	74
24	Buffer optimization of the hGCH-hGFRP complex buffer	77
25	Formation and purification of the hGCH-hGFRP complex using SEC	79
26	Relevant structural features on GCH1.	80
27	Exemplary micrograph and 2D classes of the inhibitory complex	82
28	Local resolution estimation and FSC fourier shell correlation of hGCH1-hGFRP complex structures	85
29	Overview of the architecture of the GCH1-GFRP complex and details of the EM maps of the stimulatory and inhibitory complexes.	87

30	Details of the stimulatory (blue) and inhibitory (red) EM structures reveal dramatic quaternary conformational changes and order-disorder transitions.	89
31	Overall conformational changes upon binding of compounds	95
32	Details of conformational rearrangement upon binding of AXSP0056BS to GCH1.	97
33	Substrate binding in the active and inactive GCH1-GFRP complex.	101
34	Conformational rearrangements in free and complexed GFRP.	106
35	Characterization of F122A mutant using DSF and analytical SEC.	108
36	Substrate binding in the active and inactive GCH1-GFRP complex.	109
37	K_D determination of 7-deaza-GTP using protein NMR	110
38	K_D determination using initial slopes from STD NMR build up curves.	111
39	DSF analysis of the GCH1-GFRP complex formation induced by aromatic amino acids.	114
40	hGCH1-hGFRP complex formation in dependence of the effector molecules Phenylalanine and BH4	116
41	SPR analysis of the complex formation using different hGFRP concentrations and full-length hGCH1	117
42	SPR analysis of the complex formation using different hGFRP concentrations and Δ 42-hGCH1	119
43	Specific activity of full-length and Δ 42-hGCH1	120
44	Surface representation of different conformational states in GCH1 and GFRP colored by electrostatics	122
45	Characterization of allosteric binder using an enzyme assay and DSF.	124
46	Co-structures of hGCH1-hGFRP complexes with cpd-2 and cpd-3.	125
47	Schematic representation of proposed mechanism of allosteric regulation of GCH1	138

List of Tables

1	Buffers used for lysis and protein purification of hGCH1- Δ 42-NHis .	22
2	Buffers used for lysis and protein purification of hGCH1-FL-NMBP	22
3	Buffers used for lysis and protein purification of hGFRP-FL-NHis .	23
4	Table of crystallization conditions	38
5	Relevant structural features on GCH1.	80
6	Summary of obtained hGCH1-hGFRP EM structures.	81
7	Data collection and refinement statistics for the inhibitory and stimulatory hGCH1-hGFRP complexes determined by cryo-EM . .	84
8	Summary of obtained crystal hGCH1 crystal structures.	90
9	Data collection and refinement statistics for different hGCH1 co- and apo crystals	92
10	Summary of obtained hGCH1-hGFRP ligand bound complex crystal structures.	98
11	Data collection and refinement statistics for GCH1-hGFRP ligand bound complex crystals	100
12	Summary of obtained hGFRP crystal structures.	102
13	Data collection and refinement statistics for hGFRP co- and apo crystals	104
14	Differential scanning fluorimetry (DSF) measurement TM values of GCH1 and mutated GCH1 variants.	107
15	Determined values for k_{on} , k_{off} and K_D SPR measurements.	116
16	Summary of derived structures within this work.	127

Abbreviations

AEXC Anion exchange chromatography

ATP Adenosin-5'-Triphosphate

ATZ Anilinothiazolinon

ASU Asymmetric unit

BH2 Dihydrobiopterin

BH4 Tetrahydrobiopterin

CCD Charge coupled device

Cryo-EM Cryo-electron microscopy

CTF Contrast transfer function

Da Dalton

DEAE Diethylaminoethylcellulose

dGTP Deoxyguanosine triphosphate

DSF Differential scanning fluorimetry

DNA Deoxyribonucleic acid

DMSO Dimethylsulfoxid

DQE Detective quantum efficiency

ESI Electrospray ionization

FBS Fragment based screening

FSC Fourier shell correlation

GCH1 GTP cyclohydrolase 1

GFRP GTP cyclohydrolase feedback regulatory protein

GDP Guanosine-5'-diphosphate

GTP Guanosine-5'-triphosphate

H2NTP 7,8-dihydroneopterin triphosphate

hGCH1 human GTP cyclohydrolase 1

HPLC High performance liquid chromatography

His-tag Polyhistidin-Tag

HTS High-Throughput-Screening

IC50 half maximal inhibitory concentration

IEC Ion exchange chromatography

IMP Inosine monophosphate

IPTG Isopropyl- β -D-thiogalactopyranosid

K_M Michaelis constant

K_D Dissociation constant

LaB6 Lanthanum hexaboride

LB Lysogeny broth

MBP Maltose binding protein

MPD 2-Methyl-2,4-pentanediol

MES 2-(N-morpholino)ethanesulfonic acid

MR Molecular replacement

MS Mass spectrometry

mRNA Messenger ribonucleic acid

NCS Non-crystallographic symmetry

NOS Nitric oxide synthases

NMR Nuclear magnetic resonance

NTA Nitrilotriacetic acid

OD Optical density

PAGE Polyacrylamide gel electrophoresis

PBS Phosphate-buffered saline

PCR Polymerase chain reaction

PDB Protein data bank

PEG Polyethylene glycol

Phe Phenylalanine

pI Isoelectric point

PO₄ Phosphate

PITC Phenylisothiocyanate

PTC Phenylthiocyanate

PTH Phenylthiohydantoin

PTMs post-translational modifications

rGCH1 rat GTP cyclohydrolase 1

rpm Revolutions per minute

SD Superdex

SDS Sodium dodecyl sulfate

SEC Size-exclusion chromatography

SLS Swiss Light Source

SPR Surface plasmon resonance

STD Saturation transfer difference

STD-NMR Saturation transfer difference nuclear magnetic resonance

SNR Signal to noise ratio

ssDNA Single stranded deoxyribonucleic acid

TEM Transmission electron microscope

TEV Tobacco etch virus

TOF Time-of-flight

T_M Melting temperature

UV Ultraviolet light

V_{max} Maximum reaction velocity

1 Introduction

1.1 GTP-cyclohydrolase 1

GTP cyclohydrolase I (GCH1) (EC:3.5.4.16) is a ubiquitously expressed enzyme, which catalyzes the conversion of Guanosine Triphosphate (GTP) to 7,8-dihydroneopterin 3'-triphosphate (DHNTP) (Figure 1). This reaction is the first and rate-limiting step involved in the de novo synthesis of tetrahydrobiopterin (BH4) [89], the required cofactor for tyrosine and tryptophan hydroxylases [46].

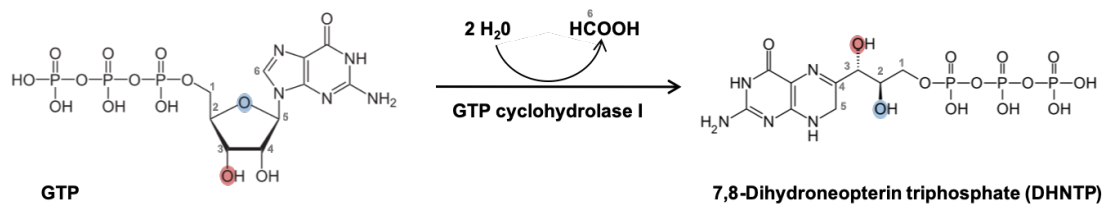


Figure 1: GCH1 catalysis the conversion of GTP to DHNTP: GCH1 catalyzes the opening of the imidazole ring of GTP and the hydrolytic release of formate followed by Amadori rearrangement of the ribosyl moiety resulting in 7,8-Dihydroneopterin triphosphate.

1.2 GCH1 structural features

1.2.1 Monomer structure

The human GCH1 sequence comprises 250 amino acids and folds into a α - β structure [85]. The N-terminal part is predominantly α -helical and consists of an antiparallel α -helix pair (α -helix h2 and α -helix h3; residues 60 - 106), which is located remote from the main body of the structure (Figure 2AB). The first 50-60 amino acids seem to be flexible and remain unresolved in the so far published mammalian GCH1 structures (1FB1,1WPL, 1IS7, 1IS8) [4, 65, 66]. The C-terminal core domain (residues 121 to 250) comprises a sequential four-strand antiparallel β -sheet with an insertion of 45 residues between β -sheet b3 and b6 [85]. This insertion contains two antiparallel α -helices (h4 and h5) arranged on one side of the β -sheet [87]. The C-terminus is formed by a α -helix, positioned on the opposing side of the β -sheet.

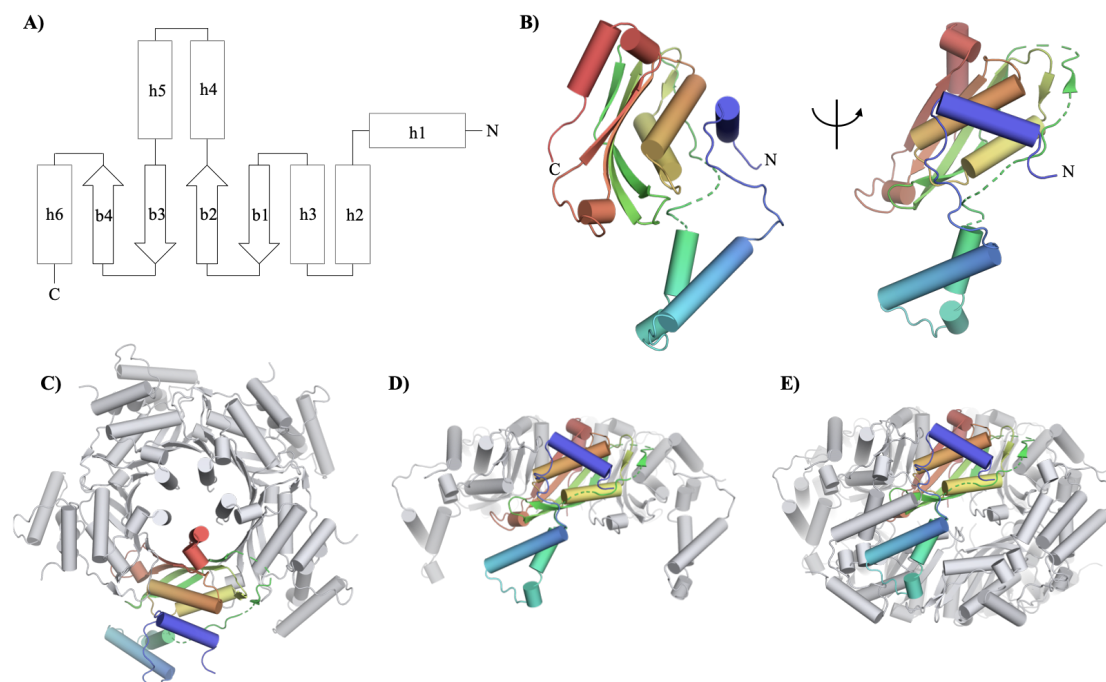


Figure 2: GCH1 monomer topology and quaternary structure: **A)** GCH1 topology plot. Helices are shown as cylinders and β -sheets as arrows. **B)** Cartoon representation of the GCH1 monomer rotated by 90° along the x axis. The chain trace is colored by rainbow colors. **C)** Top view of GCH1 pentamer. **D)** Side view of GCH1 pentamer. **E)** Side view of GCH1 decamer.

1.2.2 Tertiary structure

GCH1 forms a D5-symmetric homodecamer of 270 kDa, which is the functional enzyme complex in solution [36, 85], which can be described by the association of two pentamers.

A 20-stranded antiparallel β -barrel with a radius of 17 Å is formed by the symmetrical association of five GCH1 monomers along their β sheets. Hereby, the N-terminal β -strand (b2) of one monomer forms a hydrogen bond ladder with the C-terminal β -strand (b7) of the neighbouring monomer. This leads to the formation of a β -barrel (Figure 2C). The centre of the β -barrel is occupied by the C-terminal helices from each monomer, which form a parallel α -helix bundle with a diameter of about 15 Å. The pentamer has the overall shape of a crab with five legs composed of the N-terminal α -helix pairs of the individual monomers (Figure 2D).

The GCH1 homodecamer, which is the in solution occurring multimeric state, is

formed by face-to-face association of two pentamers. The GCH1 decamer is formed by combining two crab-shaped pentamers, whereby the 5 legs of both pentamers interact with each other (Figure 2E). In detail, the antiparallel α -helices h2 and h3 (legs) on one monomer are intertwined with those of another monomer, wedged in the gap between them and the C-terminal domain. GCH1 decamers feature a perfect D5 particle symmetry, as the arrangement of the two fivefold symmetric pentamers follows a twofold symmetry. The height of the GCH1 homodecamer is approximately 65 Å and the diameter is 100 Å. GCH1 encloses a cavity in the middle of the pentamers with the dimensions 30x30x15 Å, which is accessible through the pores formed by the five α -helix bundles in the middle of the pentamers. The GCH1 particle does not show any openings at the decamer equator.

1.2.3 Active site location, architecture and substrate binding

The cleft, forming the binding pocket for the substrate GTP, located at the interface of three subunits. Figure 3A) shows that GCH1's active site is spanned by two protomers (A and B) of the upper pentamer and one protomer of the lower pentamer (A'). Since GCH1 has a D5 particle symmetry, the decameric functional unit is composed of 10 equivalent active sites.

Each of the active sides comprises of a 18 Å long cavity with a depth of 10 Å and a varying width. All stated residue numbers listed below refer to the nomenclature of the human sequence unless otherwise indicated.

The active site is formed by the surrounding loops 142-146, 180-184, and 179-181, which are structurally stabilized by extensive short-range hydrogen bond interaction. The salt-bridge E142-R184 and the hydrogen bond interaction Q182-H210 further crosslink and stabilize the conformation of the active site. The existence of a catalytic zinc ion at the active site was discovered by the crystallographic analysis of human GCH in absence of chelating agents [4]. The metal binding site is located at the centre of the cavity (Figure 3B)). The Zn(II) ion is coordinated by two cysteine residues, namely C141(A) and C212(A), as well as H141(A). This tetrahedral coordination of the zinc ion further rigidifies the active side conformation. In combination, these features of the active site lead to a strictly limited conformational space available to the residues involved in substrate recognition and catalysis and

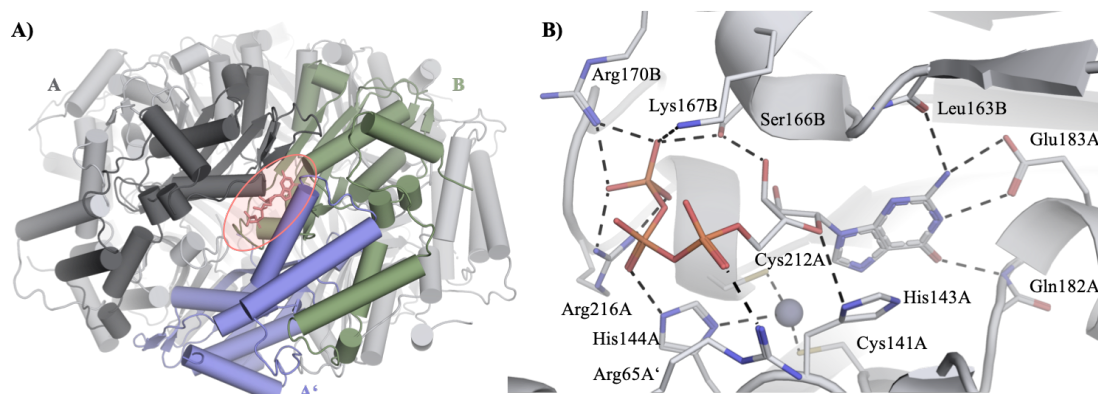


Figure 3: Active site and substrate recognition: All residue numbers refer to the human protein sequence. Residue numbers are preceded by A and B for subunits from one pentamer, A' for residues of the subunit on the other pentamer. **A)** Cartoon representation of GCH1. The active site (salmon) is formed by three GCH1 monomers (A,B,A'). **B)** Coordination of GTP and zink in the active site.

rigidify the GTP binding site. They further explain why the protein structure is hardly changed even when a substrate is bound, the metal is depleted from the protein or its binding site is mutated [96, 87, 84].

At the rim of the active site cavity, there is a cluster of basic residues (H144A, R216A R65A', R170B, and K167B) which coordinate the triphosphate moiety of GTP and compensate for the negative charges of the phosphates (Figure 3B)). Therefore, Mg(II) assisted binding to the protein, as found in other nucleotide binding proteins, is not needed for charge compensation.

The pyrimidine portion of GTP's purine ring system is recognized by the bottom of the active site cavity (Figure 3B)). Thereby E183A forms a salt-bridge with the guanidine moiety and Q183A backbone forms a hydrogen bond with its amide hydrogen to the C-4 oxo group of the purine ring. A additional hydrogen bond is formed between the carbonyl oxygen of residue L163B and the N-2 of the nucleobase. This distinctive pattern specifically recognizes guanine and explains the selectivity of the enzyme of GTP over to ATP. The ground of the pocket is lined with the residues V181A and L165B, which create a suitable hydrophobic environment for the pyrimidine ring. The affinity of GCH1 to its substrate GTP is $K_M=116 \mu\text{M}$ [106]. Known competitive inhibitors of GCH1 are guanosine-tetraphosphate ($K_i=0.13 \text{ mM}$), dGTP ($K_i=0.24 \text{ mM}$), GDP ($K_i=1.5 \text{ mM}$), and ATP ($K_i=0.24$

mM) [131].

1.2.4 GCH1 Reaction mechanism

The first committed step in the biosynthesis of tetrahydrofolate and BH₄ and is catalyzed by the enzyme GCHI [12]. GCH1 is a very tardy enzyme and the turnover of GTP to H₂NTP proceeds extremely slowly ($k_{cat} = 0.0035 \text{ s}^{-1}$) [12]. The enzymatic mechanism involves purine ring hydrolysis, Amadori rearrangement of ribose moiety and condensation to pteridine ring system. This reaction trajectory has been studied in considerable detail by NMR spectroscopy [9], presteady state kinetics [104], and site-directed mutagenesis [32, 84].

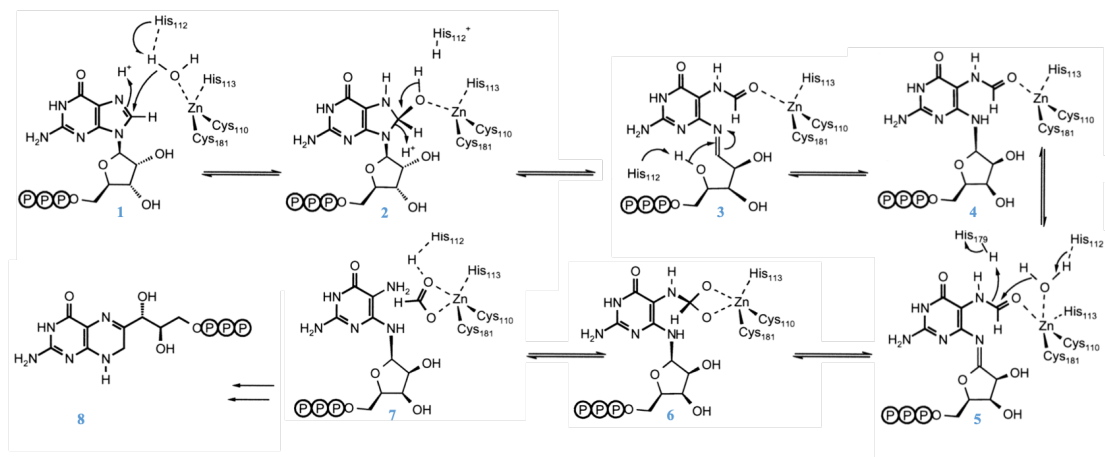


Figure 4: Hypothetical mechanism of the reaction catalysed by GCH1: Reaction steps of the hypothetical reaction mechanism for GCH1. Blue numbers indicate the respective reaction intermediates. (Figure adopted from [84]).

The reaction mechanism of GCH1 comprises the following steps and is depicted in Figure 4. First, the position C-8 from the imidazole ring of the nucleotide base is nucleophilically attacked by a zinc complexed water molecule (transition from state 1 to state 6) [84]. This is followed by the hydrolytic opening of the imidazole ring (transition from intermediate 2 to 3) with transient formation of a Schiff base (intermediate 3). Afterwards the formyl group of the 2-amino-5-formylamino-6-(ribosyl- amino)-4(3H)-pyrimidone 5'-tri-phosphate gets hydrated (transition from intermediate 4 to 5). The zinc ion functions primarily as a Lewis acid that activates water molecules for hydration of the GTP imidazole and for hydration of the

formyl group (intermediate 4) [111]. The Formamide hydrated tetrahedral state is supported by a pentacoordinated zinc (intermediate 6). Afterwards, the formate is released (transition from intermediate 6 to state 7)[84]. The last step in the reaction trajectory is the amadori rearrangement of the ribose ring and subsequent closure of the dihydropyrazine ring by intra-molecular condensation (transition from intermediate 7 to state 8)[84].

Kinetic studies have shown that the velocity of the ring opening reaction exceeds that of product formation by roughly one order of magnitude, [105, 104] the hydrolysis of the formamide bond being in turn faster than the ring opening. Thus, the hydrolytic opening of the imidazole ring of GTP is rapid by comparison with the overall reaction and therefore the ring opening is not the rate-limiting step in the reaction of GCH1 [104].

1.2.5 GCH1 sequential conservation

Based on the sequence homology the evolution of the the GCH1 family likely has been relatively conservative. Especially the C-terminal domain of approximately 120 residues is conserved exhibiting 60% identity between the *E. coli* and human GCH1. As the the conserved C-terminal domains that are responsible for oligomerisation of the protomers, it is likely that the quaternary structures of GCH1 are very similar across species. Greater sequence variability is found at the N-termini of known sequences, which also vary in length between species. All residues involved in metal binding and catalysis are highly conserved.

1.3 GCH1 therapeutic interest

GCH1's downstream product, BH4 plays key roles in phenylalanine catabolism and the biosynthesis of serotonin and catecholamine-type neurotransmitters like dopamine or norepinephrine by functioning as an essential cofactor for hydroxylases of the aromatic amino acids phenylalanine, tyrosine, and tryptophan [51, 112]. Further, BH4 is co-factor for the family of nitric oxide synthases (NOS) [58], which produce the cellular signaling molecule nitric oxide that helps to modulate vascular tone and insulin secretion and affects inflammation as well as in the regulation of immune responses [15]. Several lines of evidence, including human

genetic data that show that a GCH1 deficient haplotype is pain resistant, suggest that selective inhibition of GCH1 is an attractive target to treat neuropathic and inflammatory pain disorders [54, 91, 44]. Abnormalities in the control mechanisms of GCH1 or the activities in other enzymes of its biosynthetic pathway leads to BH4 deficiency, which is linked to a variety of vascular diseases such as diabetes, atherosclerosis and hypertension [127, 48, 73, 117, 108, 128] and to neurological disorders, including Parkinson's disease [82, 135]. Due to these severe effects of insufficient regulated GCH1, and especially its role in neuropathic and inflammatory pain makes GCH1 to an attractive pharmacologically target within pain modulation and drug development [115]. So further structural and functional studies of the regulatory complexes seem to be essential to get a deeper understanding of the mechanism of the allosteric regulation of GCH1.

1.4 GCH1 regulation

These examples impressively show the serious consequences of non-physiological levels of BH4. Nature therefore evolved highly regulated mechanisms of BH4 homeostasis. Besides the regulation on the transcriptional level, cells modulate GCH1's enzymatic activity by different approaches.

1.4.1 PTMs and N-terminus modulate GCH1's activity

It has been shown that GCH1 is regulated by multiple phosphorylation sites, both positively and negatively. 8 homologous phosphorylation sites were found in human GCHI that are able to modulate the GCH1 activity, biosynthesis of BH4 and BH2, and enzyme localization [20, 57]. Exemplary, it is postulated that phosphorylation is critical involved in GCH1 protein activity by enhancing its activity itself and reducing the feedback inhibition of GFRP by reducing its affinity in endothelia cells [57]. Further other reports suggest that the N-terminal peptide of GCH1 may also contain regulatory elements that modulate catalytic activity [41, 110]. In all structural studies GCH1's N-terminus is flexible, and disordered or truncated and therefore is not resolved in the published X-ray structures [4, 65, 66]. Therefore, there is a lack of comprehension of the structure-effect relationship between the topology and interactions of the N-terminus and the enzymatic activity. Further,

GCH1 is subject to genetic regulation. The enzyme is expressed upon stimulation of various cytokines [118]. Multiple mRNA forms have been detected in human, rat and *Drosophila* [33].

1.4.2 GFFP dependent allosteric regulation by BH4 and Phenylalanine

Further, GCHI's activity is mediated by its substrate GTP. Intracellular levels of GTP modulate GCH1 activity by changes of enzyme kinetics due to cooperative binding [36]. A high degree of cooperativity is a common feature highly symmetric, multimeric enzymes [1].

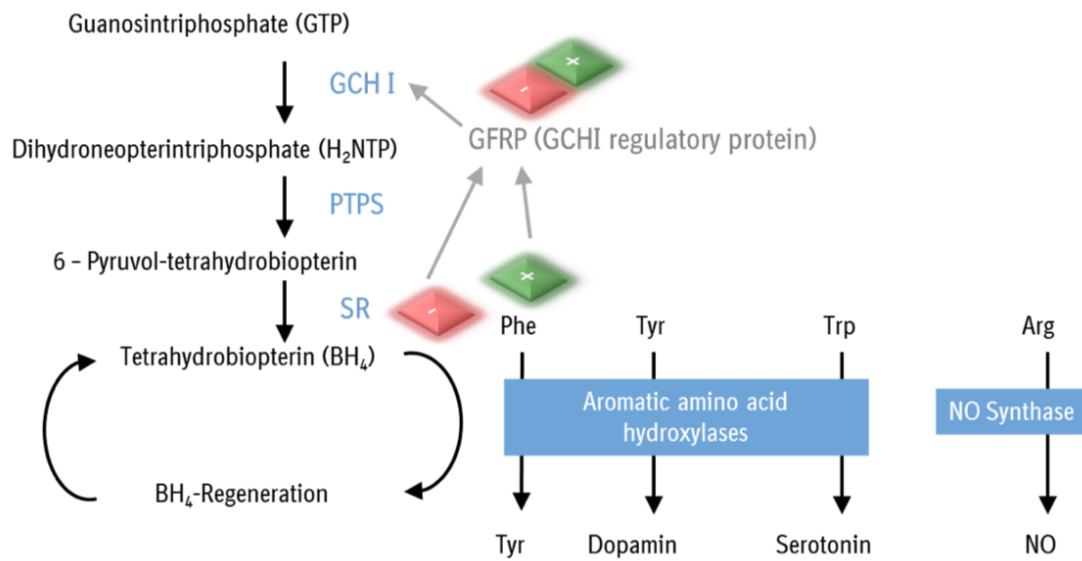


Figure 5: Positive and negative regulation of GCH1 by phenylalanine and BH4: Schematic representation of BH4 de-novo synthesis and phenylalanine catabolism. GCH1 is stimulated by feed-forward activation by phenylalanine and feedback inhibition by BH4.

In a seminal by Harada et al. the molecular basis of BH4 homeostasis was uncovered and shown to involve GCH1 and a regulatory protein, now known as GTP-cyclohydrolase-I-feedback-regulatory protein (GFRP), which simultaneously functions as a positive and negative regulator of GCH1 [133]. The effects of GFRP on GCH1 occur via formation of heteromeric protein complexes between GCH1 and GFRP, which are dependent on the presence of certain intracellular concentrations of the effector molecules phenylalanine or BH4. Elevated phenylalanine levels lead

to stimulation of GCH1 activity, whereas BH₄, the endproduct of the biosynthesis pathway, inhibits GCH1 in a feedback inhibition type mode [134]. Mammalian GCH1 show cooperative enzymatic activity. Complex formation with GFRP-Phe leads to increased activity at lower substrate concentrations and eliminates substrate cooperativity [35].

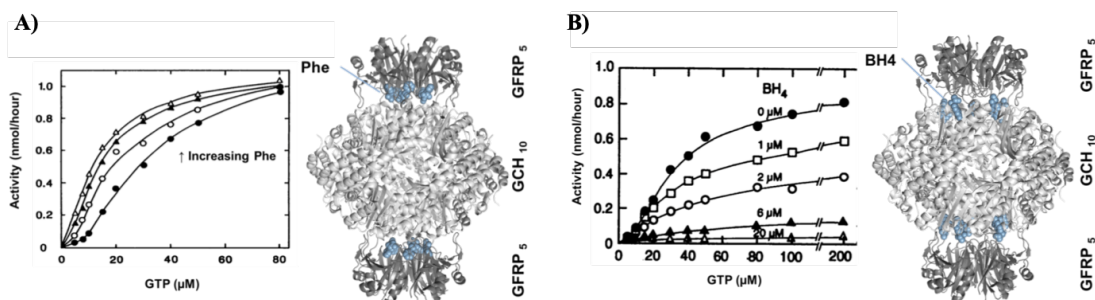


Figure 6: GCH1-GFRP stimulatory and inhibitory complexes: A) Effect of phenylalanine concentration on the substrate-velocity curve for GCH1 (Figure adopted from [35]). **B)** Cartoon representation of GCH1-GFRP stimulatory complex. GFRP is depicted in dark grey, while GCH1 is colored in light grey. Phenylalanine (blue) binds to the GFRP surface. **C)** Effect of BH₄ concentration on the substrate-velocity curve for GCH1 (Figure adopted from [35]). **D)** Cartoon representation of GCH1-GFRP inhibitory complex. GFRP is depicted in dark grey, while GCH1 is colored in light grey. BH₄ (blue) binds to the GCH1 surface.

Conversely, GCH1 alone is allosterically inhibited by BH₄ alone. In the absence of GFRP, the inhibitory effect of BH₄ is lower and occurs at higher, physiologically relevant BH₄ concentrations. Sigmoidal enzyme kinetics of GCH1 is changed to a hyperbolic behavior in the presence of GFRP by Phe in a dose dependent manner, indicating a loss cooperativity in presence of GFRP. The GCH1-GFRP system can therefore be regarded as a metabolic sensor that establishes BH₄ and aromatic amino acid homeostasis.

1.4.3 GFRP and GFRP-GCH1 structural features

GFRP occurs as a pentamer of 50 kDa (5 x 10 kDa). A monomer is folded into an α -/ β -structure with a dominant six-stranded antiparallel β -sheet. Two helices are inserted between the β -strands, both are located on the same side of the β -sheet [22]. Five monomers associate to a monomers and form a symmetrical

five-membered ring similar to β -propellers. The pentamer forms a bent disk with convex and concave surfaces. A potassium ion is coordinated to the back-bone carbonyl groups of Gln9, Arg11, Val14 and the side-chain oxygen atom of Thr8 [22]. GCH1-GFRP complexes consist of one GCH1 decamer flanked by two pentameric GFRP molecules. The association occurs along the particle fivefold axes and the complexes are approximately 370 kDa in size [66]. Size exclusion data shows that the GCH1-GFRP complex is not formed in absence of phenylalanine or BH4 [66, 132]. Ten BH4 or phenylalanine molecules are completely buried inside the GCH1-GFRP interfaces of the inhibitory or stimulatory complexes, respectively. The total buried accessible surface area of the GFRP-GCH1 interface is increased by binding of the effector molecules, thereby enhancing the association of GFRP with GCH1 by occupying the spaces at the interfaces to increase the contact area. In the stimulatory complex, phenylalanine is binding to the GFRP pentamers. However, the BH4-binding sites are located at the molecular surface of GCH1 rather than GFRP.

1.5 Allosteric sites on GCH1 and GFRP

The allosteric site for phenylalanine are found in the stimulatory complex on the GFRP pentamer. The phenylalanine binding cavities are located between two adjacent subunits and consists of residues 8-14 and residues 73-78 from one GFRP monomer and residues 73-78 from the neighboring monomer. A potassium bound to the loop region of residues 8-14, but although the ion has no direct interaction with the bound phenylalanine. The conformation of 8-14 loop seems to be stabilized by the bound potassium ion. The phenylalanine-binding cavity is tiled with hydrophobic residues to accommodate the hydrophobic phenyl group of phenylalanine. The amino and carboxyl groups of phenylalanine form multiple hydrogen bonds with GFRP residues Gln75 and Gln9. Glu-236 is the only residue of GCH1 which is directly interacting with phenylalanine and thereby is the key residue from GCH1 involved in the recognition of phenylalanine. No significant cooperativity of phenylalanine binding has been observed [134]. Phenylalanine binds to the GCH1-GFRP complex with a K_D of 94 μ M [134].

The BH4 allosteric binding site is formed by a cleft between two neighboring

GCH1 subunits. BH4 binds to the GCH1-GFRP complex with a K_D of 4 μM [citepRN52]. The BH4 binding pocket consists of residues 229-243, 127-129 and 157-159, respectively. The pterin ring of BH4 is located within the cleft and hydrogen bonds are formed between the pyrimidine part of the ring and Glu-234(B) located at the bottom of the cleft. These interactions are reminiscent of those between a heme carboxylate and the pyrimidine part of the pterin in the nitric oxide synthase pterin-binding site [126]. Asp-127(B) and Arg-241(A) form direct hydrogen bonds with BH4 while Arg-235(A) faces the BH4 ring system by Cation- π interaction. The main chain of Ser-219(A) and the side chain of Thr-231(B) participate in direct hydrogen bonds to BH4. This extensive interaction of GCH1 with the pyrimidine part of the pterin is consistent with the fact that inhibitory complex formation is induced by 2,4-diamino-6-hydroxypyrimidine (=DAHP) and analogs that contain a pyrimidine structure like that found in biopterin [134].

1.6 Previous structural studies and knowledge on allosteric regulation

Structural information on GCH1 was first obtained on the *E. coli* enzyme [86, 5, 84], later structures of the human GCH1 [4] was published. The structures revealed the subunit fold and quaternary structural arrangement of the functional complex and that GCH1 is a Zn(II)-dependent hydrolase. They give brought insights in the active site architecture and helped to shed light on the residues involved in the catalysis of GTP. X-ray structures of stimulatory and inhibitory rat GCH1-GFRP complexes are published [65, 66]. They show that phenylalanine binds to a surface pocket on GFRP close to the protein-protein-interaction interface with GCH1, whereas BH4 binds to an allosteric pocket on GCH1 close to the GFRP interface [65, 66, 67]. Strikingly, the structural differences between stimulatory and inhibitory complexes were found to be minor and the transmission of the allosteric signal towards the active site remains unraveled. The medium resolution of the studies and the circumstance that for this particular case folding and unfolding events play a major role, which are impacted by crystal packing artefacts, did not allow for detailed insights into the structural basis of allosteric control mechanisms. So far, no structures of the human GCH1-GFRP complexes, the human GFRP or GCH1

co-structures of allosterically inhibited GCH1 are available, which could help to find the missing link and gather further insights in the allosteric regulation.

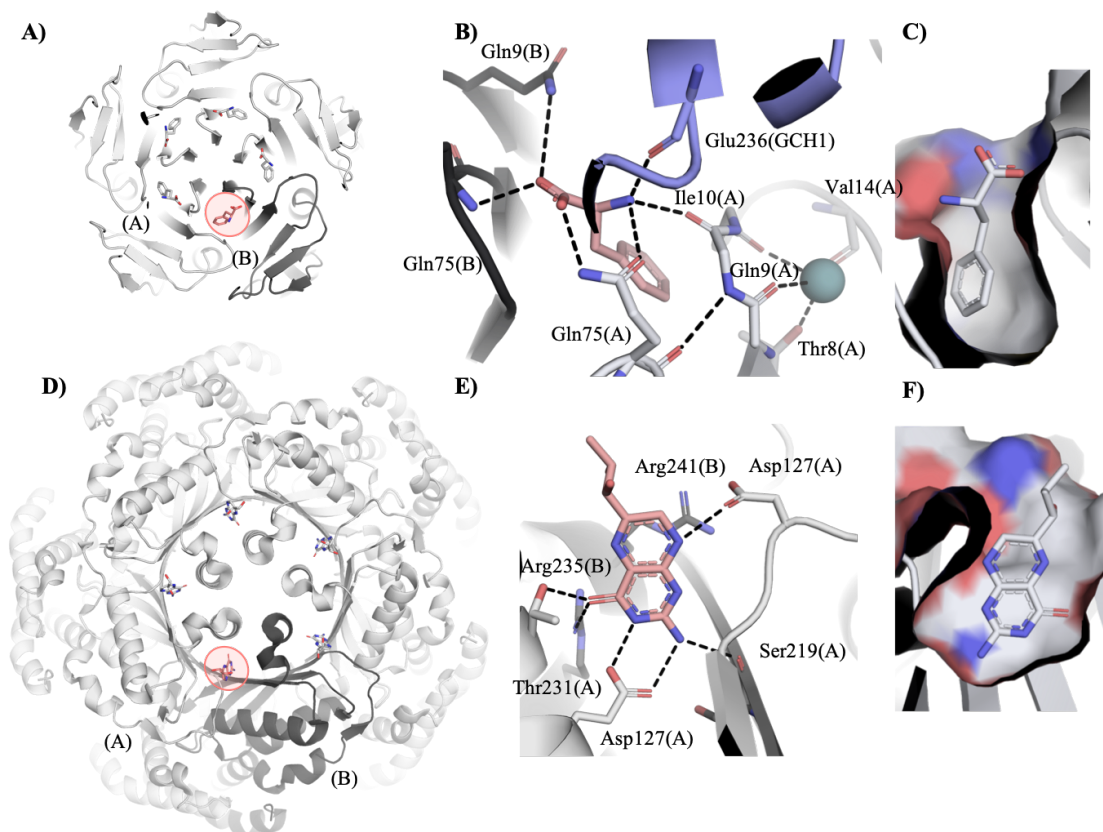


Figure 7: Architecture of allosteric sites and effector molecule coordination:
A) Five phenylalanine molecules are symmetrically arranged on the GCH facing side of a GFRP pentamer. **B)** Coordination of phenylalanine in the active site. Binding site is formed in the interface between two monomers (A) and (B). Two GFRP residues, Q75(A) and Q9(B), participate in the hydrogen-bonding interactions through their side chains; while I10(A), Q75(A) and GCH1 residue E236 are coordinating phenylalanine via their amino and carboxyl backbone groups. Loop 8-15 is coordinating a potassium ion (turquoise). **C)** Surface representation of the phenylalanine binding pocket colored by surface electrostatics (APBS; red: negative; blue: positive). The phenyl group is surrounded by hydrophobic residues. **D)** Five BH4 molecules are symmetrically arranged on the top of each GCH1 pentamer. The allosteric binding site is spanned by two GCH1 monomers. **E)** Coordination of the effector molecule BH4 in the allosteric site of GCH1. D127(A), T231(A), R235(B) and S219 coordinate the 2, 4-Diamino-6-hydroxypyrimidine (=DAHP) moiety of BH4. Further, cationic π -stacking of Arg241(B) and the pterin ring system is formed. **F)** Surface representation of the BH4 binding pocket colored by surface electrostatics (APBS; red: negative; blue: positive).

1.7 Objectives

This thesis aims to broaden the understanding of the allosteric regulation of human GCH1 using different approaches and methods.

The first aim is to elucidate all states in the trajectory from active to inactive enzyme, and in presence and absence of the regulatory protein GFRP or substrate analogs and inhibitors. These structural snapshots could help to delineate the consequences of ligand binding to the GCH1 allosteric site and their influence on the protein conformation, and therefore help to gain a better understanding of the regulation mechanisms of hGCH1. Other studies, dealing with rodent protein so far, failed to draw a conclusive and complete picture of the allosteric mechanism. Further structural and mechanistic information, especially on the human GCH1 protein and its regulatory complexes, may be very valuable in developing drugs that modulate the activity of GCH1 and thus control the de-novo synthesis of BH4.

In parallel, the next aim is to determine the structures of human stimulated and inhibited GCH1 complexes using cryo-EM. We suspect from the analysis of the rGCH1-rGFRP crystal structures that important functional regions on the protein surface undergo order-disorder transitions and could be impacted by crystal packing. Therefore, cryo-EM will be used as an orthogonal method for structure determination of the hGCH1-hGFRP complexes, which allows for structure determination under more physiological and aqueous conditions, and will deliver structural information, which is less biased by crystal artefacts.

Thirdly, to verify the hypotheses derived from the structural information at the molecular level, single point mutants of GCH1 will be generated and their activity and ability to be regulated by GFRP will be tested in an enzymatic assay that directly measures the formation of the end product H2NTP.

In order to see the impact of the formation of the inhibitory complex on the substrate affinity as well as on the substrate binding kinetics, STD-NMR will be used to determine values for K_D and measure STD enhancement of the activated and the inhibited enzyme complex.

Further, we will conduct biophysical studies based on surface plasmon resonance (SPR) and thermal shift assays (DSF), which analyze the formation of the complex between human GCH1 and GFRP and the allosteric regulation of GCH1 enzyme

activity. Moreover, we aim to present the first high-resolution crystal structures of human GFRP in the presence and absence of the effector molecule phenylalanine as well as substrate analog bound human GCH1-GFRP complex structures. This comprehensive structural and biophysical analysis will allow us to gain a better understanding of the impact and role of GFRPs in the allosteric regulation of GCH1. Additionally, we will analyze the effect of the disordered N-terminal 42 amino acids of GCH1 on GFRP complex formation and enzymatic activity to resolve contradicting literature data.

Lastly, we aim to analyze a set of allosteric GCH1 binding fragments, using X-ray crystallography, DSF and enzyme kinetics, in order to classify the fragments as 'binders' or 'inhibitors' and understand their molecular mode of action

2 Methods

2.1 Protein Characterization and Biochemical Methods

2.1.1 Discontinuous SDS-polyacrylamide gel electrophoresis (SDS-PAGE)

SDS-PAGE is a widely used technique to separate biological macromolecules, usually proteins, according to their electrophoretic mobility. Mobility is a function of the length, conformation and charge of the molecule. Protein sample homogeneity or composition was analyzed by discontinuous SDS-polyacrylamide gel electrophoresis (Laemmli, 1970). Sample aliquots were supplemented in 4 x Laemmli buffer before denaturation at 100°C for 5-10 minutes. Denatured samples were applied to 4-12% NuPAGE[®] Bis-Tris gels (Invitrogen Life Technologies). Protein fragment sizes were estimated according to the separation of either a Precision Plus Marker (BioRad) or a high-low Marker (Serva). Electrophoresis was carried out in XCell SureLockTM Mini-Cell gel chambers filled with 1 x MES SDS running buffer by applying a voltage of 200 mA for 35 minutes. To detect protein separation gels were transferred in 5 mL Instant Blue solution and destained in distilled water after about 20 minutes. Gels were dried with DryEaseTM for 30 minutes and DryEaseTM Mini Cellophan foils were used for long-term storage.

2.1.2 Determination of protein concentration

Quantification of protein concentrations were performed with the NanoDrop spectrophotometer ND-1000 by detecting aromatic amino acids in 2 nL of sample solution at an UV absorption of 280 nm. The protein concentration present in the sample is quantified by the measured UV absorption according to Lambert-Beer's law.

2.1.3 Mass spectrometry

Mass spectrometry (MS) is a high-sensitive technique to detect and quantify molecules. A mass spectrometer ionises the samples and separates them according to their mass-to-charge ratio. The mass spectrometer ionises the protein samples that are subsequently accelerated by an electric or magnetic field and recognised

by a detector according to their mass-to-charge ratio. Results are presented as spectrum of the ions signal intensity as function of their mass-to-charge ratio. Sample identification is performed by correlating known masses. MS to verify the protein identity was done in-house by the Analytical Development department, using time-of-flight mass spectrometry (TOF MS) and electrospray ionization (ESI). All protein samples were provided in solution with a concentration of 1 $\mu\text{g}/\mu\text{L}$.

2.1.4 N-terminal Sequencing

The amino-terminal (N-terminal) sequencing is a process involving the sequential cleavage of the N-terminal amino acids. It consists of repetitive cycles of Edman degradation followed by high-performance liquid chromatography (HPLC). Edman degradation includes three steps, 1) coupling of phenylisothiocyanate (PITC) to the protein α -amino group to generates phenylthiocarbamyl (PTC) groups, 2) cleavage of the N-terminal amino group by an acid induced nucleophilic attack on the peptide bond, and 3) conversion of the generated anilinothiazolinone (ATZ) amino acid to more stable phenylthiohydantoin (PTH) amino acids. PTH amino acids are detected and identified according to their retention times, compared to PTH amino acid standards, by reversed-phase HPLC using a C-18 column at 270nm. N-terminal sequencing was performed by Toplab GmbH (Martinsried, Germany) to identify phosphorylated amino acids of phosphatase treated wild type GCH1. Samples were provided in solution containing 1-50 pmol protein.

2.1.5 Enzyme kinetic assay

Enzyme kinetic assays are standardised experiments to measure the specific activity of proteins of interest, by measure the consumption of the protein substrate or its product over time. Product increase, or substrate decrease, can be monitored using different types of experimental approaches, like fluorescence, chemiluminescence, static light scattering or spectrophotometry. In this case, kinetic assays were performed to test GCH1 specific enzyme activity by spectrometric measuring the concentration of its direct product H2NTP under various conditions. SynergyTM H1 (BioTek Instruments) and Gen5 2.01 software was used to evaluate H2NTP concentration and the maximal turnover rate (V_{max}) within each measuring interval.

H2NTP concentration was measured at 330nm after a shaking period of 5 seconds over a measuring period of 2h with a measuring interval of 2-4 minutes at 37°C. Samples were prepared with 2 μ M GCH1, 3 μ M GFRP, various concentrations of GTP, Phenylalanine or BH4, and enzyme kinetic assay buffer (50 mM Tris/HCl, pH 7.5; 100 mM KCl). The specific enzyme activity (A) was calculated using the Lambert-Beer law, the path length of 0.15 cm and the extinction coefficient $\epsilon_{300\text{nm}} = 6300 \text{ M}^{-1}\text{cm}^{-1}$ of H2NTP. The resulted specific activity values were plotted against increasing substrate concentration (S) and fitted by means of Origin software using the Hill equation which was additionally used to determine the final V_{max} values, Hill coefficients (n) and Michaelis-Menten constants (K_m). Statistical analysis were performed using the Welch's t-test.

2.2 Protein production

This thesis is mainly based on an X-ray crystallography and cryo-EM based approaches. Structural studies are highly protein consuming techniques, which need large quantities of extremely pure and mono-disperse proteins. Therefore, highly optimized processes of protein production are keen.

2.2.1 Molecular Cloning

Molecular cloning refers to a set of experimental methods with the objective to generate and isolate recombinant DNA of any species for the introduction and reproduction within another species. Normally, cloning involves four main steps: Isolation and preparation of the target DNA fragments, insertion of the target DNA fragments into vector DNA to generate plasmid DNA, transformation of the generated recombinant plasmid DNA into an appropriate host organism for reproduction, and selection of organisms containing the desired recombinant DNA. DNA constructs for hGCH1, $\Delta 42$ -hGCH1 and hGFRP were synthetically produced at Invitrogen and inserted in pET17b or pET28a vectors.

2.2.2 Site-Directed Mutagenesis

DNA amplification includes three phases: denaturation, primer annealing and elongation. During denaturation, the PCR-mixture is heated up to 95°C, to break

the hydrogen bonds to obtain single-stranded DNA (ssDNA). The annealing-process enables primers hybridisation with the ssDNA and takes part at lower temperatures of 53-65°C, depending on length and nucleotide composition. During elongation, the temperature is adapted to the specific thermal optimum of the used polymerase, mostly at 68-72°C. While approximately 500 base pairs can be synthesized in 30 seconds, the duration of the elongation phase depends on length and composition of the amplified sequence, as well as on the used DNA-polymerase. To obtain an exponential number of duplicates of the desired sequence, several PCR-cycles were performed successively. After amplification, the PCR products were maintained at 4-8°C. PCR was done in purpose of the synthesis of the $\Delta 42$ -GCH1 point-mutant F122A, according the protocol of the QuikChange Lightning Site-Directed Mutagenesis Kit (Agilent Technologies) using specific mutagenesis primers.

2.2.3 Transformation of chemically competent *E. coli* cells by heat shock

Transformation is the process of genetic alteration by channelling foreign DNA into cells. One commonly used way of transformation induced by a heat shock. Positively charged calcium ions neutralize the negatively charged bacterial membrane and plasmid DNA, which is going to be introduced. Disruption of the electrostatic repulsion between membrane and DNA allows for the absorption of the exogenous DNA. To initiate this uptake, bacterial cells are exposed to a sudden rise in temperature, resulting in a pressure difference between outside and inside of the bacterial cells. To compensate this pressure gradient, cell membrane pores open and allow entering of the altering DNA.

For each transformation, 50 μ L of *Escherichia coli* BL21Star (DE3) competent cells (Novagen) were thawed on ice. 10 ng plasmid DNA was added and cells were mixed gently by tapping. After 30 minutes of incubation on ice, a heat shock was performed at 42°C for 30 seconds. Cells were immediately placed on ice and 250 μ L SOC medium was added. For growing, cells were incubated at 37°C for 60 minutes while shaking at 225 rpm. Finally, 50 μ L *E. coli* cells were plated out on LB plates, containing ampicillin (100 μ g/mL) or kanamycin (50 μ g/mL). After overnight incubation at 37°C, antibiotic containing LB medium (ampicillin: 100

$\mu\text{g}/\text{mL}$; kanamycin: $50 \mu\text{g}/\text{mL}$) was inoculated with selected colonies to generate bacterial stocks containing 25% glycerol, stored at -80°C .

2.2.4 Expression and lysis

Recombinant protein is a manipulated form of protein, which is generated in with the help of plasmid vectors to modify gene sequences. Protein sequences often need to be truncated, punctually mutated and additional residues or even complete protein sequences can be attached in order to make proteins more stable, soluble or to simplify purification. These recombinant proteins are produced in bacterial, insect or mammalian cell lines. Especially protein crystallization is a very protein consuming technique, therefore proteins need to be produced in high yields. Special DNA-sequences called promoters initiate transcription of particular genes and they are hence genetically engineered in upstream direction of the target protein sequence. The expression of recombinant protein was driven by the LacZ promoter through addition of IPTG. IPTG is not hydrolyzable by the cell and is therefore kept at a constant concentration during the entire expression. For most protein characterization methods, the protein needs to be extracted from the cell and separated from cell debris and bacterial proteins in order to get a homogeneous target protein solution. Required degree of purity depends on the applied technique. For structural studies the protein should be at least 85 % pure.

2.2.5 Expression and lysis of GFRP and GCH

Escherichia coli BL21Star (DE3) Competent Cells (Novagen) were used for the protein expression of human His-tagged GFRP and $\Delta 42$ -His-tag versions of human GCH1 and MBP-tagged full-length constructs. Sequences of protein constructs are listed in the Appendix. 25 mL LB-medium, containing $100 \mu\text{g}/\text{mL}$ ampicillin for GCH1 constructs or $30 \mu\text{g}/\text{mL}$ kanamycin for GFRP, were inoculated with bacterial glycerol cultures of transformed *E. coli* and incubated at 37°C overnight while shaking at 120 rpm. Following day, the pre-cultures were diluted in 1 L LB-medium and grown at 37°C until reaching an optical density at 600nm ($\text{OD}_{600\text{nm}}$) of 0.6-0.8. Protein expression was induced by adding 1 mM IPTG. Expression was stopped after 4 h for GFRP and 16 h for GCH1 constructs via harvesting by centrifugation

at 3000 g for 30 minutes at 4°C and stored at -80°C until further processing.

All buffers used for protein expression, lysis and purification are listed in Table 1,2 and 3. For cell lysis, bacteria pellets were re-suspended in 5 mL/g lysis buffer. Cell suspensions were sonicated on ice by means of the 7 Sonoplus Ultrasonic homogeniser HD 2200 (Bandelin ElectronicTM), using RZ 3 exposure vessels (Bandelin ElectronicTM). Depending on the expressed protein construct, period of sonication varied. For GFRP and Δ 42GCH1 constructs pulse cycle 5 at 100 % for 5 x 45 seconds were utilized while GCH1 full length constructs are sonicated for 3 x 30 seconds. The cell lysates were centrifuged at 45000 g for 45 minutes at 4°C, to separate cell debris. Supernatant was used for protein purification.

Table 1: Buffers used for lysis and protein purification of hGCH1- Δ 42-NHis

Lysis buffer		Ni-NTA elution buffer	
300 mM	NaCl	300 mM	NaCl
50 mM	TRIS pH 8.0	50 mM	TRIS pH 8.0
	DNase	300 mM	Imidazole
	Complete-protease inhibitor cocktail		
Ni-NTA wash buffer		EC and crystallization buffer	
300 mM	NaCl	150 mM	NaCl
50 mM	TRIS pH 8.0	20 mM	TRIS pH 8.0
10 mM	Imidazole		

Table 2: Buffers used for lysis and protein purification of hGCH1-FL-NMBP

Lysis buffer		Amylose resin elution buffer	
300 mM	NaCl	300 mM	NaCl
20 mM	TRIS pH 7.5	50 mM	TRIS pH 7.5
	DNase	8 mM	Maltose
	Complete-protease inhibitor cocktail		
	Lysozyme		
Amylose resin wash buffer		EC and crystallization buffer	
300 mM	NaCl	150 mM	NaCl
20 mM	TRIS pH 7.5	20 mM	TRIS pH 7.5

Table 3: Buffers used for lysis and protein purification of hGFRP-FL-NHis

Lysis buffer		Ni-NTA elution buffer	
300 mM	NaCl	300 mM	NaCl
50 mM	TRIS pH 8.0	50 mM	TRIS pH 8.0
	DNase	300 mM	Imidazole
	Complete-protease inhibitor cocktail		
Ni-NTA wash buffer		EC and crystallization buffer	
300 mM	NaCl	150 mM	NaCl
50 mM	TRIS pH 8.0	20 mM	TRIS pH 8.0
10 mM	Imidazole		
Dialysis and anion exchange application buffer		anion exchange elution buffer	
50 mM	TRIS pH 8.0	50 mM	TRIS pH 8.0
1 mM	DTT	1 mM	DTT
		1000 mM	NaCl

2.2.6 Purification

Affinity chromatography Affinity purification is based on specific reversible binding interactions between target molecules and matrix-coupled ligands. Binding to the solid phase is achieved either by column chromatography or by batch treatment. One example of affinity tags is the Polyhistidine-tag (His-tag). Histidine-tagged (His-tagged) proteins have a high selective affinity for Ni^{2+} and several divalent metal ions. Consequently, a protein containing a histidine tag binds strongly to a metal-ion charged medium while other cellular proteins bind only weakly. Histidine-tags are small and can therefore be less disruptive to the properties of the proteins to which they are attached. Elution is performed by competing out the interaction between the His-tag and the Ni^{2+} by increasing concentrations of imidazole. Another commonly used affinity chromatography makes use of the maltose binding protein (MBP) tag. MBP is a naturally occurring protein in E.coli that interacts with the carbohydrate maltodextrin. On the one hand, MBP is a solubility-enhancing tag that protects the target fusion-protein against proteolytic degradation; on the other hand, it facilitates as affinity purification tag and enables the isolation of the MBP-tagged proteins by binding to matrix-cross-linked amylose. Here, protein elution is typically done by competition with a maltose-containing buffer after unspecific bound components are washed up.

Ion exchange chromatography Ion exchange chromatography (IEC) was used for tag-free purification. It separates molecules on the basis of differences in their net surface charge. The charged groups within a molecule that contribute to the surface charge possess different pKa values depending on their structure, and chemical

microenvironment. Since all molecules with ionizable groups can be titrated, their net surface charge is highly pH dependent. IEC chromatography takes advantage of the fact that the relationship between net surface charge and pH is unique for a specific protein. A protein that has no net charge at a pH equivalent to its isoelectric point (pI) will not interact with a charged medium. An IEC medium contains a matrix of particles with ionic groups that can be negative (cation exchange) or positive (anion exchange). When the entire sample has been loaded, conditions are altered in order to elute the bound proteins. Proteins are normally eluted by increasing the salt concentration of the buffer or, occasionally, by changing the pH. As ionic strength increases the bound proteins begin to elute.

Size exclusion chromatography Size exclusion chromatography (SEC) is a useful technique for handling biomolecules that are sensitive to changes in pH, concentration of metal ions or co-factors and harsh environmental conditions. Gel filtration separates molecules according to differences in Stokes radius as they pass through the gel filtration medium. Large molecules elute from the column first, followed by smaller molecules. SEC can not only be used for purification steps. Buffer exchange and analytical SEC are additional practical implementations of this principle. Before setting up crystallization trials, it is strongly recommended to perform SEC in order to obtain a homogeneous sample without aggregates and unwanted oligomers.

For all hGCH1 and hGFRP proteins, Superdex 200 (SD200) column (26/600) from GE Healthcare was used. The column was previously equilibrated with the SEC buffer (Table 1 & 3). Then, 5 mL concentrated protein was loaded and pumped over the column using a flow-rate of 1 mL/min. The elution of protein was measured by UV detection at 280 and 260 nm wavelength and collected in 2 mL fractions in deep well blocks.

Protein purification of hGCH1 constructs All buffers used for protein purification were filtered through 0.45 μ m filters. Unless stated otherwise, all purification steps were carried out at 4 °C. Full length hGCH has a N-terminal His-tag and the Δ 42-hGCH1 is MBP-tagged. The proteins were purified using the respective affinity resins.

4 mL Ni-NTA (Machery-Nagel) or Amylose resin (New England Biolabs) was loaded onto an empty spin column. The column was equilibrated with lysis buffer (Table 1 & 2) before the lysate was loaded onto the column, incubated for 30 minutes and washed with five times the column volume. For the His-tagged proteins 10 mM imidazole was already used in the wash buffer, to reduce unspecific binding of non-tagged protein to the column. Afterwards elution buffer was added and incubated for 5 minutes. Further elution steps were performed until the protein concentration was no longer measurable. The GCH constructs were cleaved by adding TEV-protease at a ratio of 1:100 and incubation for 16-24 h at 4°C while dialysis in four litres of SEC buffer. Inverse affinity purification using the respective resin was performed to remove uncleaved proteins. The TEV-cleaved protein mixture were incubated for 1h at 4°C to enable for binding of uncleaved proteins to Ni-NTA or amylose resin. Flow-through was captured for further purification.

Δ 42-GCH1 constructs and full-length constructs were further purified by SEC, using the Äkta Avant 25 SR1 (GE Healthcare) and a Superdex 200 Increase 10/300 GL column (GE Healthcare) or the Äkta Explorer (GE Healthcare) with a HiLoad 26/600 Superdex 200 (GE Healthcare) column. For injection, Proteins were concentrated to an appropriate volume, using Ultra-15 Centrifugal Filter Unit, 50 kDa cutoff (Amicon). Protein purity of GCH1 constructs were verified by SDS-PAGE whereas the final protein concentrations were determined by Nanodrop at A280 nm. Proteins were snap frozen in liquid nitrogen and stored at -80°C until further processing.

Protein purification of hGFRP His-tagged GFRP was affinity purified in batch process, by incubating the supernatant for 1 h with equilibrated Protino® NiNTA Agarose resin (Macherey-Nagel) while rotating at 4°C, to enable His-tag. After transferring into column, resin was washed with 3-5 column volumes wash buffer until no protein was determined via nanodrop. Proteins were eluted in 3-4 steps by adding one column volume of elution buffer. Further purification was carried out by an anion exchange chromatography (AEXC), after desalting and re-buffering via dialysis. Simultaneously to the dialysis, GFRP His-Tag was cleaved by adding two times 1.5 U of Thrombin (Sigma T4648, 5 U/ μ L) and incubation at RT while stirring for 24 h. Desalted and His-tag cleaved protein solution was concentrated

by using Ultra-15 Centrifugal Filter Unit, 30 kDa cutoff (Amicon). Anion exchange chromatography was performed using HiTrap Q HP, 5 mL (GE Healthcare) column. To reach higher protein purity, SEC was carried out, using HiLoad 26/600 Superdex 200 (GE Healthcare) column with the Äkta Explorer (GE Healthcare). Protein purity of GFRP was verified by SDS-PAGE whereas the final protein concentration was determined by Nanodrop at A280nm. The protein was snap frozen in liquid nitrogen and stored at -80°C until further processing.

GCH1-GFRP complex formation The identification of suitable buffer conditions was key to the preparation of high quality grids and improved crystal growth. The final puffer composition was identified using the ProteoPlex technology [13]. 100 mM sodium phosphate pH 5.5, 80 mM NaCl and 20 mM phenylalanine was used to form the stimulatory complex and 100 mM sodium citrate pH 5.75 and 0.1 mM BH4 (Sigma Aldrich; T4425) was used for the formation of the inhibitory complex. For complex formation hGCH1 (6 mg/ml) and hGFRP (10 mg/ml stock) was mixed using a 1.3 x hGFRP molar excess. The mixed proteins were diluted by 1:10 in complex buffer (100 mM sodium phosphate pH 5.5, 80 mM NaCl, 20 mM phenylalanine or 100 mM sodium citrate pH 5.75, 0.1 mM BH4) and incubated for 30 min at 4°C. Afterwards, the complexes were concentrated using a 100 kDa Amicon Ultra Centrifugal Filters concentrator. The two distinct protein complexes were purified using a Superose 6 Increase 10/300 GL column and the respective complex buffers. The elution profile shows the complex peak eluting at a volume corresponding to the size the hGCH-hGFRP while the uncomplexed hGFRP elutes as a smaller peak. Only the three peak fractions from the complex peak were pooled in order to avoid the shoulder region. Afterwards the protein was concentrated to the desired concentration using a 100 kDa Amicon Ultra Centrifugal Filters concentrator.

2.3 Biophysical methods

Biophysical methods are helpful for further characterization of proteins and determination of ligand binding and complex formation. They are often used as preliminary-screen to filter for false-positive hits of e.g. biochemical assays and

complementary to structural information, to get further information of protein stabilization, ligand affinity and kinetics.

2.3.1 Differential scanning fluorimetry

Differential scanning fluorimetry (DSF) is a method to determine thermal denaturation temperature of a protein in changing conditions or in presence of ligand molecules. The fluorescence dye, SYPRO Orange, binds non specifically to hydrophobic surfaces residues, and water strongly quenches its fluorescence. When the protein unfolds, the exposed hydrophobic surfaces residues bind the dye. This results in an increase in fluorescence by excluding water. The stability curve and its melting temperature (T_M) obtained by gradually increasing the temperature to unfold the protein and measuring the fluorescence at each point. Stability curves are measured for protein and protein complexed with ligand. The ΔT_M is calculated by subtracting both melting temperatures.

Determination of small molecule binding Differential scanning fluorimetry measurements were set up using 2 μ M protein (GFRP of GCH1) and 20 mM phenylalanine, tryptophan and tyrosine or 0.1 mM allosteric (BH4-like) inhibitors and 5x SYPRO Orange protein dye (stock 5000x). Protein, ligand and fluorescent dye were diluted in a way that equal, pipettable amounts would result in the desired end-concentration. Total sample volume was 10 μ L. Each sample was at least run in triplicates. The CFX384 Touch™ Real-Time PCR Detection System was used to run the temperature gradient. Temperature was altered from 15-95 °C with increment of 0.5 °C, holding each temperature for 30 sec before taking a readout.

Monitoring of complex formation 2 μ M GFRP and GCH1 was used for complex formation experiments. 0.1 mM BH4 or 20 mM Phe were used to initiate the complex formation. Protein effector molecules and controls were incubated for 30 minutes in ice before supplementing with 5x SYPRO Orange protein dye (stock 5000x). Total sample volume was 10 μ L. Each sample was at least run in triplicates. The CFX384 Touch™ Real-Time PCR Detection System was used to run the temperature gradient. Temperature was altered from 15-95 °C with increment of 0.5 °C, holding each temperature for 30 sec before taking a readout.

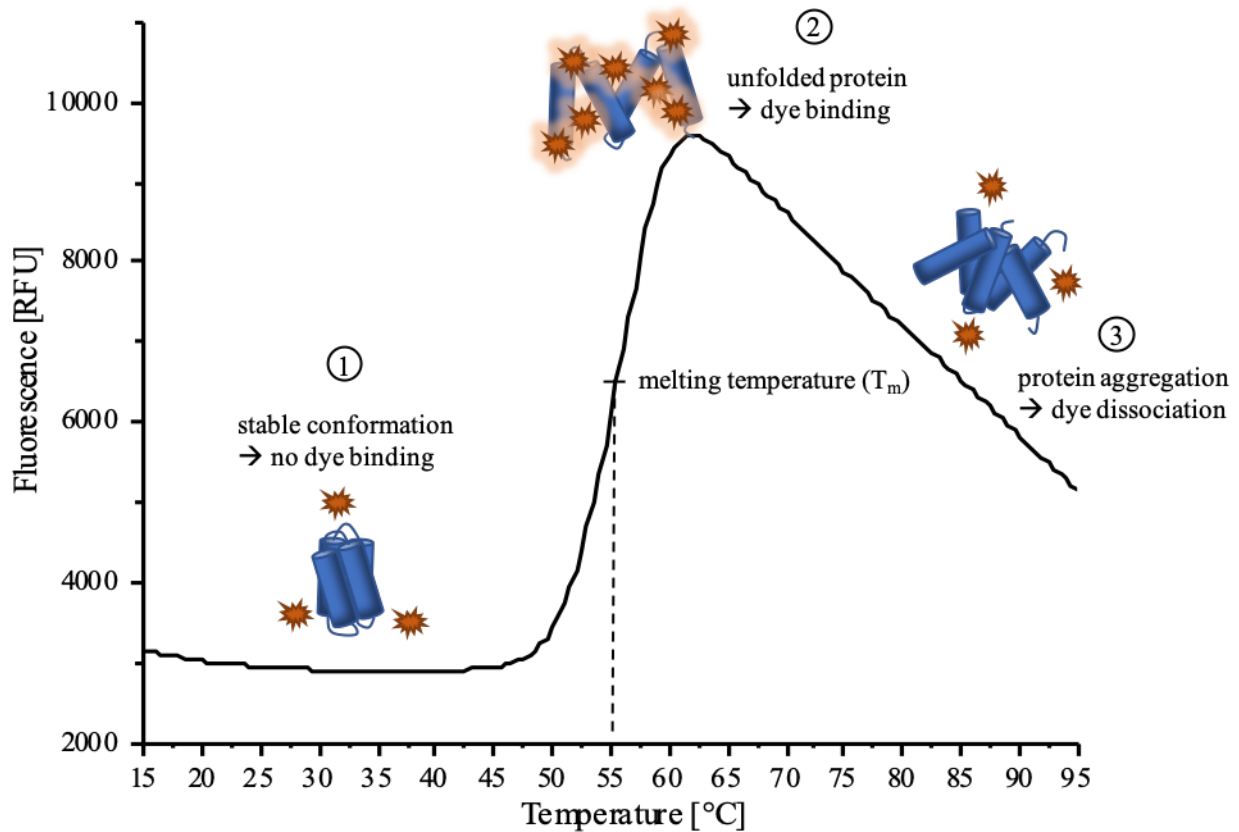


Figure 8: Principle of differential scanning fluorimetry: Determination of the thermal stability of proteins by means of a hydrophobic dye and fluorescence measurements. (1) The hydrophobic dye is quenched in aqueous solution. (2) Temperature increase induces thermal unfolding of the proteins, leading to explosion of their hydrophobic core regions. The dye binds, becomes unquenched and effects an increase in the fluorescence signal. (3) Denatured proteins aggregates and the dye dissociates.

Buffer screening To improve the stability of the GCH1-GFRP complex a 96-well formate sparse-matrix screening, monitoring the thermal unfolding behavior in the presence of various buffers and small molecules, was conducted. The tested buffers were chosen in analogy to the published ProteoPlex method [13]. Equimolar ratios of 2 μM GFRP and 2 μM GCH1 were mixed and supplemented with 0.1 mM BH4 or 20 mM Phenylalanine. 10x concentrated buffers socks were added to the protein resulting in 100 mM of the respective buffer in each well. In the same manner, further additives and salts were tested. 5x SYPRO Orange protein dye

(stock 5000x) was supplemented. The total sample volume was 10 μ L. Each sample was at least run in triplicates. The CFX384 TouchTM Real-Time PCR Detection System was used to run the temperature gradient. Temperature was altered from 15-95 °C with increment of 0.5 °C, holding each temperature for 30 sec before taking a readout. For the comparison of the melting curves, the melting temperature, the simultaneous melting of both complex components and the steepness of the melting transition were evaluated as main criteria to evaluate the stabilization of the protein complex in each buffers. For this analysis no software was used, the curves were simply compared by eye.

2.3.2 Surface plasmon resonance

Surface plasmon resonance (SPR) monitors molecular interactions of metal surface-bound molecules by measuring the refractive index-changes of surface plasmon polarities. This allows determining kinetic and affinity parameters like association and dissociation constants of chip-captured biomolecules interacting with molecules provided in solution and floating through the chip flow cells. Specific binding interactions change the surface volume that leads to changes in the SPR refracting index, which are measured and plotted against the time (Figure 9). The signal response is proportional to the number of surface bound molecules in accordance to their molecular weight and measured in resonance units (RU). This way, SPR is used to study various types of interactions, reaching from protein-protein interactions, small-molecule binding or even interaction of viruses and whole cells.

Kinetic and thermodynamic characterization of interaction and allosteric regulation of human GTP cyclohydrolase I with its regulatory protein hGFRP was performed on the SPR instrument biacore T100 (GE Healthcare). Human GTP-CH-I was immobilized using standard amino coupling chemistry on the CM5 biosensor. HEPES buffer (HBS-N, pH 7.2) and 10 mM acetate buffer pH 5.5 supplemented with 1 μ M ZnCl₂ were used as a running and a coupling buffer, respectively. Activated and deactivated flow cell served as the reference flow channel. Allosteric regulation of the regulatory and stimulatory complexes of the hGCH1 with hGFRP was analyzed in Tris buffer (50 mM Tris, 200 mM NaCl, 0.01 % (v/v) Tween 20, pH 7.2). Analysis buffer complemented with 1 mM BH₄ or 10 mM l-Phe was used

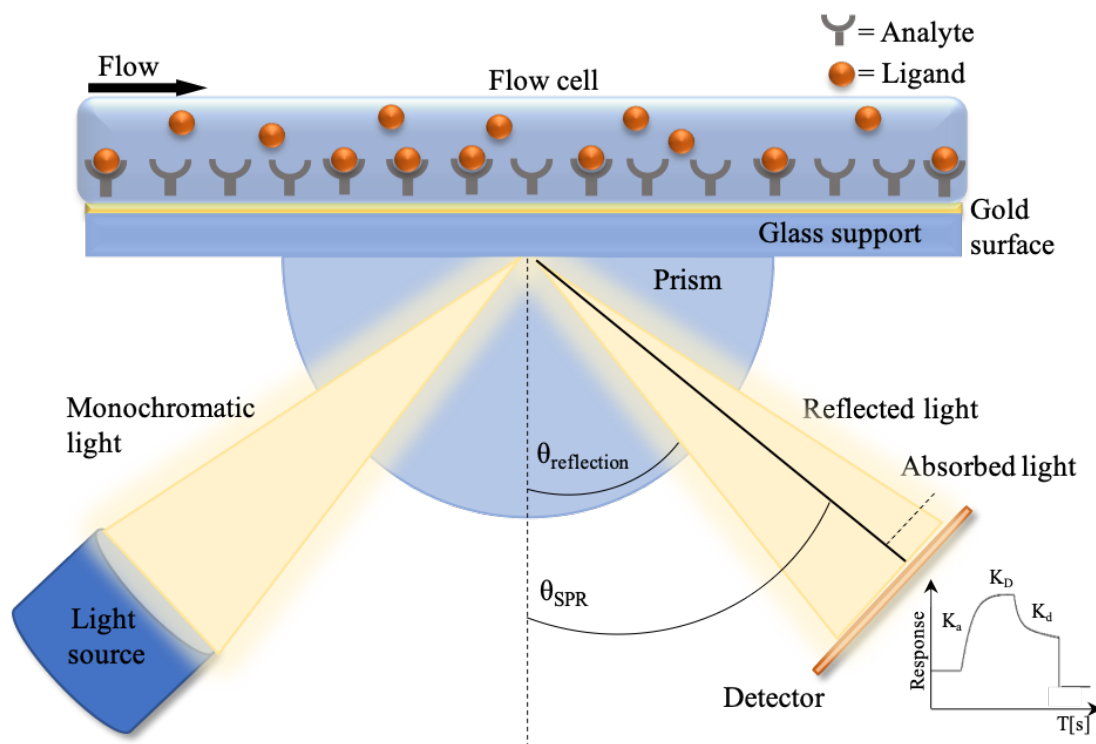


Figure 9: The Surface plasmon resonance detection principle: Surface plasmon resonance is produced within a gold layer by incident, polarized light that is totally reflected. The binding of biomolecules to the sensor surface coupled analytes, increase the refractive index, which induces a shift of the SPR angle that is directly proportional to the mass increase on the surface. Binding interactions are detected in real-time and are processed and plotted against time.

to study the kinetic and thermodynamic of stimulatory and inhibitory complexes, respectively. Binding analysis was performed at 25°C and the flow rate of 50 $\mu\text{l min}^{-1}$. Every single concentration was analyzed in duplicate and analyzed samples were diluted with factor 2 in the appropriate running buffer. Regeneration of the active surface was performed in the analysis buffer exclusive of any allosteric regulator. Analysis of allosteric regulation of both complexes was carried out on the same protein surface with immobilized human GTP-CH-I.

2.3.3 Nuclear magnetic resonance spectroscopy

NMR experiments and data analysis was carried out by Dr. Martin Rübhelke and Dr. Robert Meinecke in the lab of Dr. Markus Zeeb and Materials and Methods

were kindly provided by them (Boehringer Ingelheim, Germany).

NMR titrations and production of isotope labelled protein. Perdeuterated protein with selectively labelled protonated and ^{13}C -labelled alanine, isoleucine, leucine and valine methyl groups {Ala $^{\beta}$ -[^{13}C CH $_3$]; Ile $^{\delta 1}$ -[^{13}C CH $_3$]; Leu $^{\delta}$, Val $^{\gamma}$ -[^{12}C D $_3$ / ^{13}C CH $_3$]} was expressed as described in the literature [31]. Purification was done as described for the unlabeled protein. All spectra were recorded on a Bruker Avance III 800 MHz NMR spectrometer equipped with a cryogenic triple resonance probe at 298 K. 50 μM of perdeuterated GCH1 monomer with selectively labelled methyl groups was dissolved in 1x PBS in D $_2\text{O}$. ^1H , ^{13}C HMQC spectra of the protein were recorded with increasing concentration of the non-hydrolysable GTP analog 7 deaza GTP up to a final concentration of 3.5 mM. Spectra were processed with Bruker Topspin 3.5 and analyzed using CcpNmr [124] analysis version 2. Chemical shift perturbation (CSP) was calculated using formula (1) and the binding curve was fitted using formula (2).

$$CSP = \sqrt{(\delta_H - \delta_{Href})^2 + \frac{(\delta_N - \delta_{Nref})^2}{100}} \quad (1)$$

Where δ is the chemical shift of the spectrum in the apo (ref) or in presence of 7-deaza-GTP in the proton (H) and nitrogen (N) dimension.

$$y = \frac{CSP_{max} * (x + K_D + [P] - \sqrt{(x + K_D + [P])^2 - 4 * x * [P]})}{2 * [P]} \quad (2)$$

Where CSPmax is the fitted chemical shift of the saturated complex, K_D is the fitted dissociation constant and $[P]$ is the GCH1 concentration.

STD NMR titration assay All NMR experiments were performed at 25 °C on a Bruker HD 600 MHz spectrometer equipped with a cryogenic probe head. Deuterium oxide (D $_2\text{O}$) NMR-buffer solution containing 40 mM sodium hydrogen phosphate-phosphate-mixture (sodium phosphates, NaPi) with 150 mM sodium chloride (NaCl) was adjusted to a pD of 7.4 (corrected). Suppression of broad protein resonances was achieved by a T1 ρ -filter [103] formed by a 50 ms spin lock pulse. Saturation Transfer Difference (STD) NMR spectra were acquired with hard

pulse WATERGATE water suppression [95] using excitation the sculpting sequence [43] and W5 pulse trains for selective inversion [61].

Difference spectrum ligand signal intensities were divided by corresponding off resonance spectrum signal intensities resulting in relative STD intensity values. Multiplication by ligand excess factor yielded STD amplification factor (STD AF) values [70]. For selective protein signal saturation, a cascade of Gaussian-shaped pulses was applied. Series of measurements with different total saturation times (t_{sat}) covering a range between 1.2 seconds and 7.2 seconds were recorded for extraction of initial slopes from STD AF build up plots. An additional relaxation delay varying from 2.8 seconds to 0.4 seconds was inserted before the saturation cascade to keep constant the total time per scan. On resonance irradiation was set to 0.16 ppm, and off resonance irradiation was set to 66 ppm. Depending on the ligand concentration, 64 to 1024 scans were acquired for the STD experiments (32 to 512 scans for both on and off resonance). Considering the STD AF to be directly proportional to the fraction of bound receptor gives rise to a hyperbolic dose response curve (specific one site binding model) when STD AF values are measured with different ligand concentrations [?]. Apparent (saturation time dependent) dissociation constants for 7 deaza GTP were calculated by plotting all STD AF values of a single saturation time (e.g. 3.6 seconds) against the ligand concentration and fitting the data points to the Langmuir binding model [56]. To overcome the saturation time dependency additionally extrapolated K_D values were calculated from initial slope values (STD AF0) of the STD AF build up [90]. Fast protein ligand rebinding during t_{sat} and accumulation of saturated ligand molecules yields lower STD AF values predominantly for high ligand to protein excess factors and this results in higher apparent K_D values. These effects are minimized as t_{sat} approaches 0.

Functional assay with NMR detection For the functional assay each NMR sample was prepared with 10 M GCH1 and 170 M or 600 M test compound. The PBS NMR buffer additionally contained 300 M GTP (Cayman Chemical cat. no. 16060). After a reaction time of 45 minutes (25 °C) a certain amount of substrate molecules (GTP) has been converted by GCH1 into 7,8 Dihydroneopterin (H2NPT) and the by product formate (deprotonated formic acid). For product detection a

WATERGATE ^1H -NMR spectrum was recorded (128 scans). We used the integrated NMR signal of the formate α proton at 8.33 ppm as a relative enzyme activity readout. The formate integral of a negative control sample (DMSO) has been set to 100 %. An inhibitory active test compound decreases the GTP turnover and leads to a reduced relative formate signal integral (% inhibition). 2,4 Diamino-6 hydroxypyrimidine (DAHP) was used as a positive control.

2.4 Crystallization

2.4.1 Crystal symmetry

X-ray radiation with a wavelength of about 0.5 to 2.0 Å (0.05-0.2 nm) is used to obtain atomic resolution for macromolecules, this corresponds to the length of covalent bonds. Structure determination with X-rays depends on X-ray diffraction from a crystal lattice. One single molecule would not generate a measurable diffraction and it would be quickly destroyed by the X-rays. Therefore, X-ray crystallography depends on the growth of crystals in which the molecules are arranged regularly.

Protein crystals consist of a highly ordered three-dimensional array of molecules, which are held together by non-covalent interactions. The smallest identical repeating unit of a crystal is called unit cell. It can be viewed as the smallest building block of the crystal that can generate the entire crystal structure by means of translation operations in three dimensions. The unit cell is defined by six parameters: the lengths of the three cell axes (A, B, and C) and the three angles between them (α , β and γ) (Figure 10). Defined constraints on these lengths and angles of a unit cell gives rise to seven crystal systems (triclinic, monoclinic, orthorhombic, tetragonal, trigonal, hexagonal and cubic), with lattice points at each corner of the cell (Figure 11).

Besides these primitive (P) unit cells, there exist face (F), body (I) and side (C) centered unit cells in some crystal systems. Taking these centered unit cells into account, 14 Bravais lattices can be described. The smallest object needed to generate the whole unit cell by applying the crystallographic operations is called the asymmetric unit (ASU) of the unit cell. The ASU of a unit cell contains all the necessary information to generate the complete unit cell of a crystal structure by

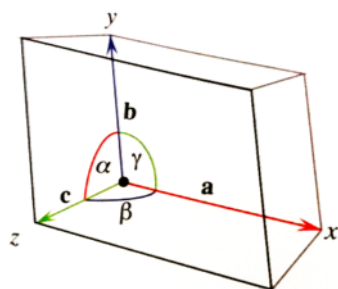


Figure 10: Example of a 3-dimensional (triclinic) unit cell: The unit cell vectors a (red), b (blue), c (green), which extend from the origin, and the angles α , β , γ between two axes are shown.

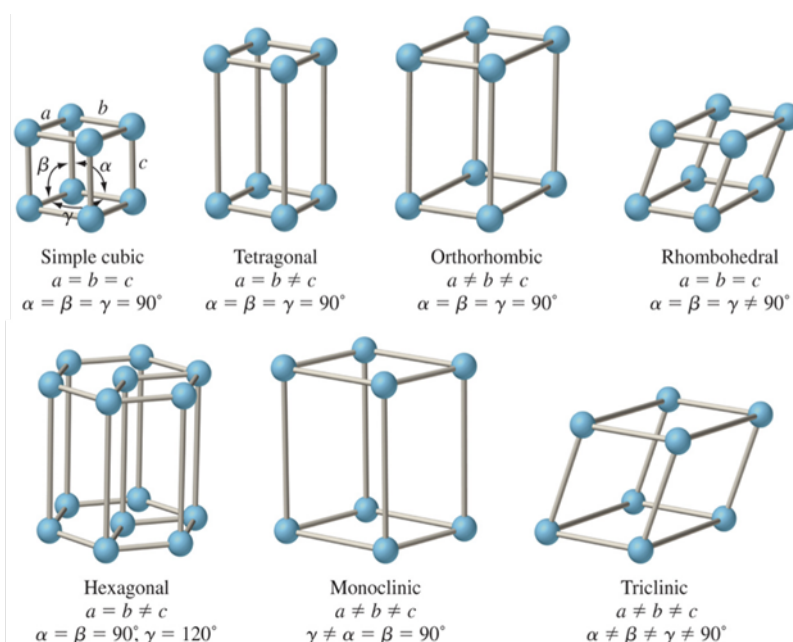


Figure 11: The 3-dimensional primitive crystal lattice systems: The most symmetric (simple cubic, upper left) lattice is shown first, followed by lattices with decreasing internal symmetry ending with the least symmetric one (triclinic, lower right).

applying its symmetry operations to the asymmetric unit. Because of the chiral nature of proteins, the only symmetry operations allowed and found in protein crystals are translations, rotations and combinations of both (screw axes).

Combining the 11 point groups allowed in protein crystals with translations and centering operations gives rise to 65 chiral space groups in which proteins may crystallize. A Space group is designated by a cryptic symbol (such as $P2_12_12_1$) in

which a capital letter indicates the lattice type (P for primitive) and the other symbols represent symmetry operations that can be carried out on the unit cell, without changing its appearance.

2.4.2 Protein crystal growth

A fundamental requirement to solve the three dimensional structure of a molecule by usage of X-ray crystallography is the availability of protein crystals of good quality and size. The size matters as very small crystals consist of a relatively small number of scatterers that usually lead to weak signals of the diffracted X-ray beams. The objective of most crystallization methods is to crystallize proteins by slowly increasing the concentration of a precipitant and the protein itself. The precipitants are usually salts or water-soluble polymers that, as they become solvated, compete for the highly ordered water molecules from the water cages that automatically form around the hydrophobic portions of a protein in aqueous solution. As a consequence of this salting-out effect, hydrophobic surface regions of the proteins become exposed to the free water, which will facilitate their interaction with the exposed hydrophobic regions of other proteins in the solution and thus eventually to the formation of intermolecular precipitates.

The most widely used crystallization method that is based on the salting-out principle is vapor diffusion. Two common variations of this method are hanging and sitting-drops (Figure 12). Both are utilizing vapor diffusion in a sealed environment to slowly increase the protein concentration over time. The course of a typical vapor diffusion crystallization experiment can be roughly divided into three stages illustrated by a phase diagram in Figure 13. At the beginning of a crystallization experiment, a drop of the protein solution is mixed with a precipitant containing crystallization solution. The reservoir is spatially separated from the drop and contains a significantly larger volume of the crystallization solution. As a result of the lower overall concentration of solutes in the drop mixture compared to the reservoir solution, water vapor diffuses from the drop into the reservoir and causes a slow increase in protein and precipitant concentration in the drop. Once the solution reaches the moderately supersaturated nucleation zone, crystal nuclei will form spontaneously and start growing. As a consequence of the continuous crystal

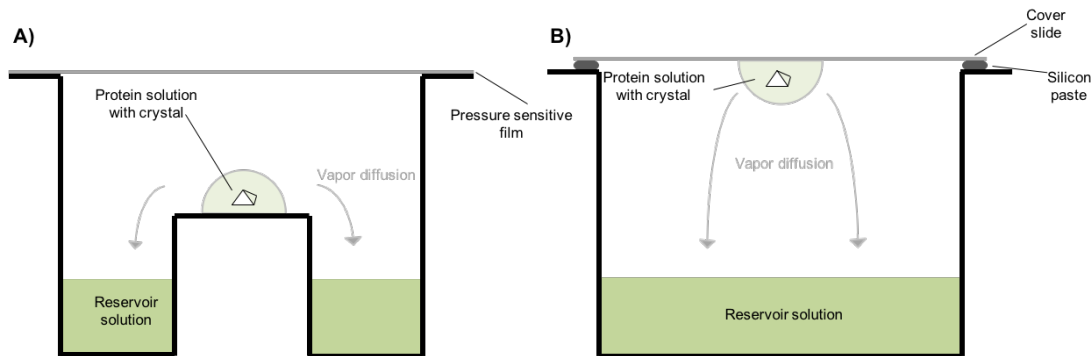


Figure 12: Schematic figures of vapor diffusion based crystallization techniques:A) In the sitting and hanging drop B) method. As a result of the lower overall concentration of solutes in the protein drop mixture compared to the reservoir solution, water vapor diffuses from the drop into the reservoir and causes a slow increase in protein and precipitant concentration in the drop and therefore crystallization of the protein occurs.

formation and growth, the concentration of free protein in the crystal drop will decrease, which will consequently move the drop mixture to the less supersaturated metastable zone. In this zone nucleation ceases and only crystal growth continues until the crystals are in equilibrium with the saturated protein solution. At this point the crystal growth stops. Crystal growth is dependent on many parameters, such as the initial protein quality and precipitant concentrations, the temperature, the pH of the solution and the presence of additives. There is no way to predict the parameters and consequently the composition of a successful crystallization condition for a given protein. This requires the crystallographer to systematically test varying crystallization conditions for each protein.

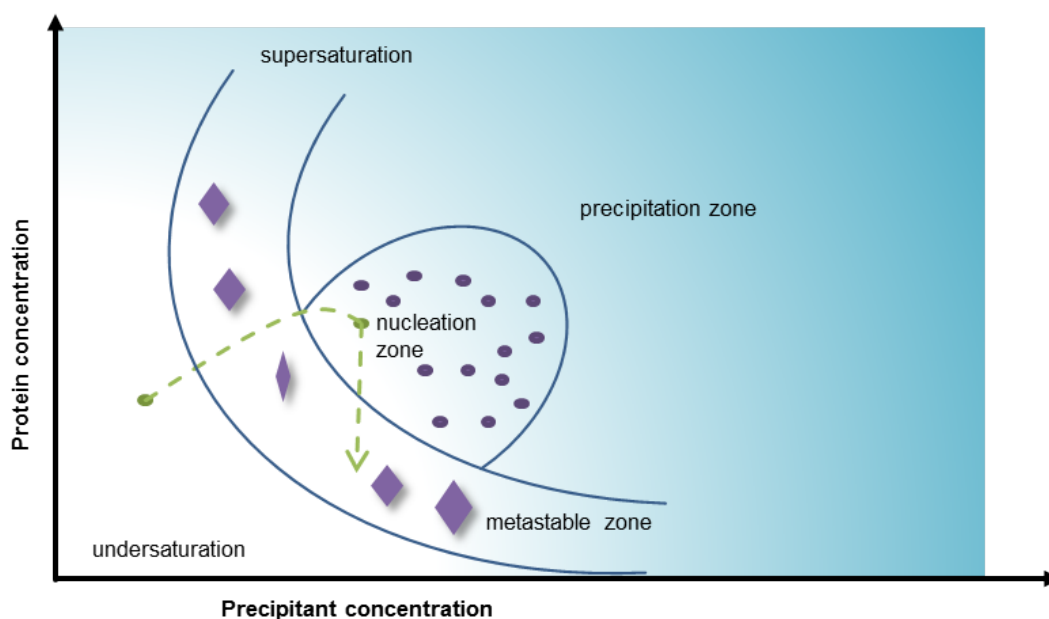


Figure 13: Phase diagram describing the vapor diffusion experiment: The influence of the two crystallization parameters - protein concentration and crystallizing agent concentration on the formation and growth of protein crystals. Due to water diffusion, the concentrations increase along the arrow from undersaturation over the metastable phase to the nucleation zone. Crystal nuclei form spontaneously and start growing. The concentration of free protein in the crystal drop will decrease, which will consequently move the drop mixture to the less supersaturated metastable zone. In this zone only crystal growth continues until the crystals are in equilibrium with the saturated protein solution. At this point the crystal growth stops.

2.4.3 Crystallization and crystal optimization strategy

After purification the protein was stored at $-80\text{ }^{\circ}\text{C}$ in PBS or SEC buffer. For protein crystallization of hGCH1, the buffer was exchanged to 100 mM Citrate pH 5.75, 50 mM NaCl by concentrating using the Amicon Ultra Centrifugal Filters with a 100 kDa cutoff. The protein sample was initially diluted 1:20 in buffer (100 mM Citrate pH 5.75, 50 mM NaCl) and concentrated up to approximately 1 ml. In order to achieve a proper buffer exchange this step was repeated 2-3 times. Afterwards, the protein was concentrated to 6 mg/ml and filtered. For the crystallization of GFRP, the buffer was not exchanged, and the protein was concentrated to 10 mg/ml in the SEC buffer using Amicon Ultra Centrifugal Filters with a 30 kDa cutoff.

In search of conditions in which the hGFRP, hGCH1 or the hGCH1-hGFRP

can form crystals, many parameters that contribute to the crystallization process had to be tested simultaneously. Therefore, commercially available screens covering a broad range of different aqueous solutions containing buffers and salts as well as additional precipitating ingredients were mixed in a 1:1 1:2 and 2:1 ratio with protein solution. As recommended by Ng et al. primarily eight following screens (JCSG, Basic, Index, Pact, Proplex, Morpheus, Classic-I, Classic-II) were tested at 3 different drop ratios (1:1 1:2 and 2:1) and 2 temperatures (4 and 20 °C) [88]. The initial screens were set up in 96-well plates (INTELLI-PLATE 96-3) using the sitting drop vapor diffusion method and incubated at 4 °C, and the crystal development was carefully monitored and systematically recorded. A pipetting robot (mosquito Crystal (TTP Labtech) / Crystal Phoenix (Art Robbins Instruments)) was employed to improve the reproducibility of the experiments. While some setups resulted in protein precipitate or semi-ordered structures, so-called quasi-crystals, also many conditions were found to yield in crystals. Conditions were diffracting crystals were grown, were usually optimized in fine screens. In the most cases fine screens were set up by building a grid around the original crystal condition varying the pH and precipitant condition. For further optimization, e.g. if crystals grew only in two dimensions, seeding and additive screening was implemented. A summary of all crystallization conditions is listed in Table 4.

Table 4: Table of crystallization conditions

crystal name	PDB code	cpd	crystallization condition
GCH	6Z87	-	1.26 M (NH ₄) ₂ SO ₄ ; 0.1 M TRIS pH 8.5; 0.2 M Li ₂ SO ₄
	6Z88	AXSP0056BS	10 % PEG 8K; 0.2 M MgCl ₂ ; 0.1 M Tris pH 7 (JCSG BS)
	6Z89	AXSP0056BS	30% GOL-P4K; 0.1 M MB2 pH 7.5; 0.12 M amino acids (Morpheus H7)
	6Z86	7-deaza-GTP	0.1 M MB3, 30 % EDO-P8K; 0.12 M ethylene glycols (Morpheus E10)
GFRP	7ACC	-	2.4 M di-Sodium malonate; pH 7.0 (JCSG F9)
	4I726	7AL9	Phe 0.1 M NaCit pH 5.0; 20 % w/v PEG 8000 (Proplex E11)
complex	7ALC	Phe	2 M NaCl; 0.1 M NaCit pH 6.0
	7ALB	7-deaza-GTP + Phe	25% MPD 0.2 ; NH ₄ Acet; 0.1 M Bis-Tris pH 5.5
	7ALA	D100613584	30% GOL-P4K; 0.1 M MB3 pH 8.5; 0.12 M Monosaccharides (Morpheus F11)
	7ALQ	7-deaza-GTP + BH4	0.2 M Sodium malonate pH 7.0; 20% w/v PEG3350 (Index H03)

Seeding Microscopic bodies are the starting point of every crystallization process. The spontaneous crystal nucleation appears at high level, a multitude of small and often con-joined crystals or microcrystal showers are formed. If the nucleation zone is not reached no crystal appears at all. Providing crystallization nuclei at low supersaturation, (where growth is possible but no nucleation occurs) can improve or initiate crystallization by achieving a balance between the amount of nuclei and crystal growth. The micro-seeding technique therefore uses tiny fragments from crushed crystals.

Seeding was implemented with the help of the seed beat kit (Hampton Research). Crystallization experiments were adapted and performed using sitting drop method of 150 nL protein solution, 50 nL seed solution and 100 nL mother liquor. Different dilutions of the seeding stock were used (undiluted, 1:10, 1:100 and 1:1000). Seeding shows improvement of the crystal quality in most experiments. Especially during the crystallization of hGFRP in complex with phenylalanine, seeding dramatically improved the shape and diffraction quality of crystals.

Additive screening Additive screening uses a library of small molecules that can affect the solubility and crystallization of proteins. These small molecules can perturb and manipulate sample-sample and sample-solvent interactions. They also are able disturb water structure, which can alter and improve both the solubility and crystallization of a sample.

For additive screening, the Additive Screen kit (Hampton Research) was used. The kit is designed to allow the rapid and convenient evaluation of 96 unique additives and their ability to influence the crystallization of the sample. Additive screening was used to optimize a crystal condition found during fine screening, which already delivered crystals of poor quality. The additive screen solution was previously mixed, with the mother liquor (40 μ L mother liquor and 10 μ L additive solutions). A 0.3 μ L drop of the protein solution was mixed with 0.2 μ L of the reservoir solution of the 96-well plate. The additive condition, which leads to the best crystals, was used later to set up a fine screen.

2.4.4 Soaking

In order to find out, how a ligand binds the protein, soaking of the ligand into preformed crystals of the target protein is usually the method of choice. This method commonly employs crystals of the protein that has been crystallized in the absence of any added inhibitor (apo crystal). Compared to co-crystallization, this method can be easily used whenever the protein amount is limited or large numbers of ligands need to be screened. The main disadvantage of this method is that the protein is rigidified by the crystal lattice. Hence, large movements of the protein upon ligand binding are hindered or will damage the crystal lattice. As the main goal was to study the conformational landscape of hGCH and the conformational

changes induced by active site binders, positive and negative modulators and hGFRP, soaking of preformed crystals was avoided to reduce the change of creating biased structures due to crystal close contacts.

2.4.5 Co-crystallization

Some ligands induce conformational changes of the protein and can therefore destroy the crystal packing during soaking. Ligands, which are very insoluble in the crystallization buffer will not be able to occupy enough binding sites within the protein crystal during soaking to result in good ligand density. These ligands could benefit from co-crystallization. During co-crystallization experiments, protein-ligand complexes were obtained by mixing and incubating the protein and its binding partner before setting up the crystallization. In order to study hGCH1's conformational changes, co-crystallization is the method of choice, as it allows the compound induced conformation to be adopted before the crystal contacts are formed.

GFRP at 10 mg/ml or GCH at 6 mg/ml was mixed with 20 mM Phenylalanine (200 mM stock, in PBS), 1 mM BH4 (100 mM stock in water), 1 mM 7-deaza-GTP (100 mM stock ; TriLink N-1044-10), 0.1 mM 8-oxo-GTP (10 mM stock; Jena Bioscience NU-1116S) or 1 mM AXSP0056BS (200 mM in DMSO) and incubated at 4 °C for 1h. Screening for crystallization conditions was carried out as previously described in section 2.4.3.

2.4.6 Crystal freezing

To minimize radiation damage from the high-energy X-rays to the crystals, diffraction measurements are performed at -180 °C in a gaseous nitrogen stream evaporating from liquid nitrogen. Previously, the crystals need to be frozen. Because protein crystals usually grow from aqueous conditions, the formation of crystalline ice during the freezing process can break protein crystals, leave artifacts in the diffraction pattern, or completely destroy the diffraction patterns. Therefore, crystals are usually treated with cryo-protectants.

For most experiments cryo solutions were freshly prepared using 28 % glycerol, as a cryo-protectant and mother liquor in order to minimize dissolving of the crystal.

Crystals were transferred into the cryo-solution with a loop for 30 s and flash frozen in liquid nitrogen. After freezing, the crystals were either tested immediately or kept in a storage dewar at $-180\text{ }^{\circ}\text{C}$ in liquid nitrogen. For some crystals glycerol was not suitable as a cryo agent. Therefore cryoscreen was used to find a better cryo condition. The cryo screen was already described and established [88]. Apo hGCH1 crystals showed a nice improvement of diffraction and reproducibility after using 25 % 1,6 hexanediol instead of glycerol for crystal freezing.

2.5 X-ray crystallography

2.5.1 Data collection

X-rays are electromagnetic radiation of wavelengths between 0.1 and 10 Å. X-ray beams in the useful range for crystallography (0.5 to 2.0 Å) can be produced by a cathode ray tube. High voltage application (40 kV) produces highly accelerated electrons from a heated cathode that hit the anode (e.g. copper). As most of the electron energy is converted to heat, the anode is rotated and cooled with water. Some electrons, however, knock other electrons out of the copper atom's lowest energy orbital, the K-shell. The hole in the core shell is filled by an electron of higher energy from an upper shell. The energy difference is emitted as X-ray radiation. Home source measurements in this thesis were carried out on a Micromax 007 HF rotating anode generator (1.5418 Å) equipped with a mar345 and a PILATUS3 detector. The home source beam line was only used for testing purpose.

X-ray radiation from synchrotron sources was used for collection of data sets. Synchrotron radiation possesses higher intensity along with a better focus. In synchrotron rings, electrons are forced into a circular orbit by large magnetic fields, and therefore constantly emit electro-magnetic radiation. This radiation is collected and focused by a series of magnets, mirrors, and monochromators. In contrast to the home source, synchrotron radiation consists of a broad electromagnetic spectrum. This offers a choice of wavelength.

1 Å wavelength was routinely used for general data acquisition. Data sets were collected at the beamlines PX I, II, and III of the Swiss Light Source in Villigen (Switzerland). A diffraction image was recorded for each increment of rotation (0.25°) and beam intensity of 20 % using a PILATUS 6M or EIGER hybrid pixel

array detector (DECTRIS Ltd.). X-ray diffraction data were collected at cryogenic temperature (100 K).

2.5.2 Diffraction

When X-rays hit a protein crystal, the X-rays interact with the electrons of the macromolecules, so that the crystal lattice planes act as semipermeable mirrors on which a portion of the X-rays is diffracted. The diffracted X-rays have the same wavelength as the incident beam, but their phase and amplitude depend on the distribution of scattering matter (electrons in the unit cell). The amplitudes and phases are related to the content of the unit cell by a mathematical relationship, the Fourier transform. The lattice that is observed upon diffraction of X-rays is related to the crystal lattice by an inverse relationship, and is therefore called the reciprocal lattice. The positions of lattice points in the reciprocal lattice are described by the Miller indices h , k , and l .

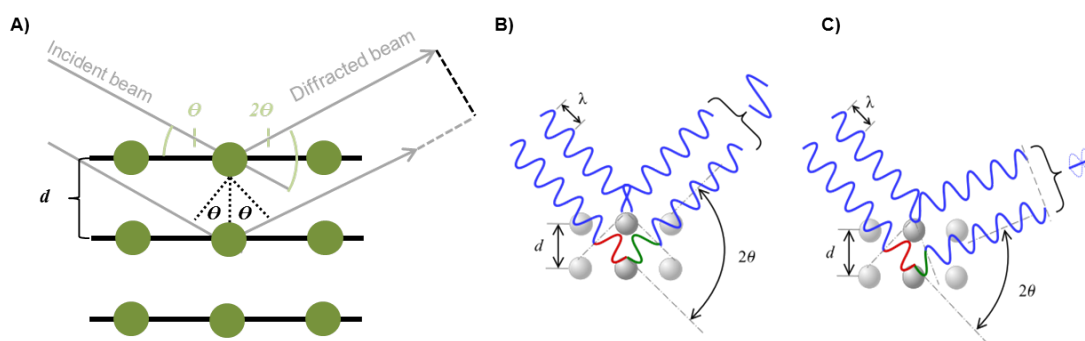


Figure 14: Bragg's law: **A)** Beams with identical wavelength and phase are scattered off two different lattice planes with a distance d and an angle θ . Constructive interference occurs when the path difference is equal to an integer multiple of the wavelength of the radiation. According to the 2θ deviation, the phase shift causes constructive **B)** or destructive **C)** interferences.

In 1912, Sir William Lawrence Bragg described the conditions under which diffraction leads to constructive interference, causing a reflection (h,k,l) that can be observed on a detector. Bragg's law states that a reflection can be observed if the path difference between two beams hitting crystal lattice planes with a distance d under an angle θ is a multiple of the utilized wavelength λ (Figure 14).

Paul Ewald created a three-dimensional graphical representation of Bragg's law using the Fourier reciprocal lattice (later called Ewald sphere (Figure 15)). A sphere is drawn with radius $1/\lambda$ and the crystal in its center. The origin of the reciprocal lattice lies at the edge of the sphere in the transmitted beam. The Bragg condition is fulfilled and diffraction is observed if a reciprocal lattice point lies on the surface of the sphere. The crystal is rotated during the diffraction measurements, therefore other lattice points will intersect the sphere and diffract. Diffraction reflexes are indexed by assigning them the Miller indices (h, k, l) , which are used to label the reciprocal lattice vectors. For non-anomalous data, reflexes $F(h, k, l)$ and $F(-h$

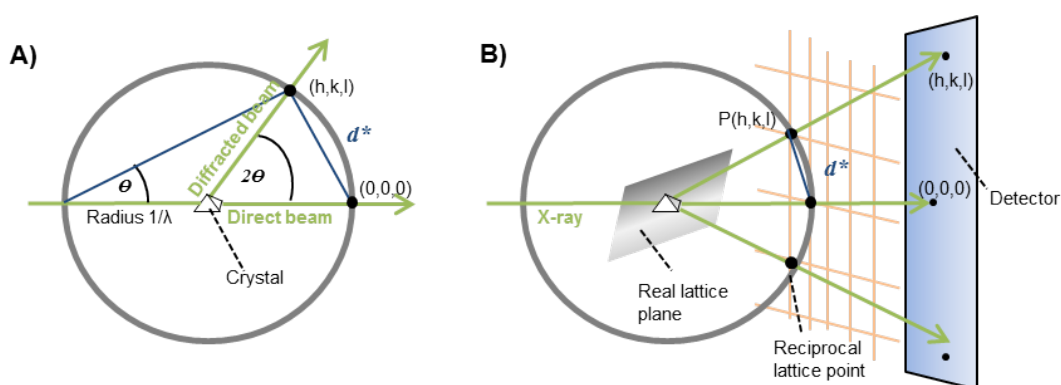


Figure 15: Ewald sphere and reflection condition: A) Two-dimensional representation of a Ewald sphere. The sphere represents the fourier space, while the crystal and diffracted waves are represented in real space. **B)** Ewald sphere with intersecting reciprocal lattice (orange) and detector showing the relation between reciprocal and real space. A reflection is only observed if the diffraction vector corresponding to a point of the reciprocal lattice located on the surface of the sphere.

$-k -l)$ possess the same intensity (Friedel's Law) and are therefore named Friedel pairs. The phase information is lost upon diffraction and only reflection intensities can be obtained, an experimental problem that needs to be overcome for complete diffraction analysis (see section phasing).

2.5.3 Data processing

In practice, data processing and reduction is divided into three main steps: indexing, integrating and scaling. The recorded data were processed using the autoPROC toolbox [122], an offline tool for the fully automatic processing of diffraction images.

The autoPROC implementation uses XDS [45] as the data-processing engine and POINTLESS [26] for space-group determination. MOSFLM [7], SCALA [27] and several other programs from the CCP4 suite are also pipeline components. The typical steps during this process involve (i) image analysis; (ii) spot search; (iii) indexing; (iv) initial analysis of diffraction quality and detector parameters; (v) refinement of initial unit-cell parameters, orientation and mosaicity; (vi) determination of the most likely space group; (vii) integration of all images and (viii) scaling and merging of integrated intensities (Figure 16 [122]).

Indexing is performed by using modules within the XDS package that search the collected data frames for reflections and then assign hkl values to each one of them. Knowing the positions of the individual reflections as well as the X-ray wavelength and the distance of the crystal from the detector allows the indexing program to determine the parameters of the unit cell by measuring the distances and angles between the reflections. At this stage one can already determine the crystal system but not yet the space group of the crystal. Within the refinement step, detector origin, beam direction, rotation axis, unit cell orientation, and cell constants will be refined (CORRECT step of XDS).

The objective of the integration process is to assign a defined raw intensity to each recorded reflection. Particular reflections may be dispersed over multiple frames. Therefore, the first task for the integrating program is to combine these measurements. The second task of the indexing program is to integrate the raw pixel intensity of the diffraction spots and define their three-dimensional profile. In other words, the program defines which area (size and shape) belongs to a reflection and which not (background). After the integration step a list of the observed hkl reflections and their corresponding raw intensities (and the estimated error for each observation) is obtained. At this point we are able to analyze the systematic absences of reflections. Systematic absences are caused by certain internal symmetry elements (screw axes) of the crystal's unit cell. In combination with the determined Bravais lattice type, systematic absences can be used to determine the space group. Additionally pointless checks the chosen space group by scoring all the possible Laue groups consistent with the crystal class, by matching potential symmetry equivalent reflections. It then checks sets of reflections which may be systematically absent to suggest a possible spacegroup. There is also a check for lattice centering,

and for twinning implemented.

Many recorded hkl reflections are symmetry-related to each other and should therefore theoretically have the same intensity. However, in practice this is usually not the case and instead some variation in intensities of the symmetry related reflections is observed. These variations can be caused by the weakening diffraction of a crystal in the course of the experiment due to radiation damage or different X-ray path lengths through the crystal (crystal shape). In order to correct these intensity variations, the scaling program assigns a scale factor to each hkl reflection, which consequently results in a list of hkl reflections with consistent intensities. However, the list still contains the redundant hkl reflections that were already present in the list of reflections after the integration step. Subsequently, as part of the scaling process these redundant hkl observations are merged to a single hkl reflection. The output file of the program consists of a table that contains a list of all unique hkl reflections as well as their intensities. Furthermore, tables are generated whose statistical content report the data quality and the resolution limit of the data.

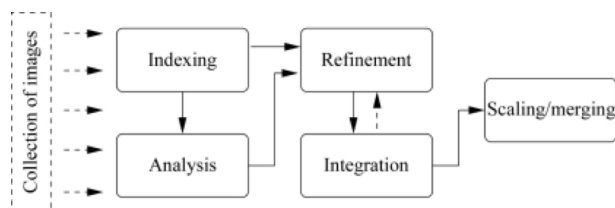


Figure 16: Workflow of offline data-processing steps in autoPROC: The collected spots are indexed and the diffraction quality and detector parameters are analyzed. Afterwards the input parameters are refined to precisely determined the cell parameters. This step is followed by integrating, scaling and merging of the spots.

2.5.4 Calculating the electron density and MR Phasing

X-rays are scattered at the electron sheath of atoms. The electrons position can be described as a three dimensional distribution, the so called electron density distribution ρ . As crystals are periodic assemblies of molecules, the electron density of a crystal resembles a periodic function. Thus, a Fourier Transformation (Fourier-Summation) can be applied to calculate the electron density for each point $(x, y,$

z). The inverse Fourier Transformation of the electron density can be written as

$$\rho(xyz) = \sum_{hkl=-\infty}^{+\infty} |F(hkl)|^2 * e^{-2\pi i(hx+ky+lz)-\phi(hkl)} \quad (3)$$

Calculation of the electron density at every point (xyz) then requires the knowledge of $F(hkl)$. The amplitude $|F(hkl)|$ of a scattered wave is proportional to the square root of the measured intensity $I(h, k, l)$ for each reflection (hkl).

$$I(hkl) = |F(hkl)|^2 \quad (4)$$

Only $|F(hkl)|$ is determined from the directly observed intensity $I(hkl)$ during measurement. The structure factor $F(hkl)$ however is not completely specified by the measured intensities as the phase of the reflection $\phi(hkl)$ is lost during data collection process. Without the phase the electron density can not be calculated. This is the so called phase problem in crystallography. To overcome the phase problem in de novo structure determination, several approaches are applied including isomorphous replacement (MIR/SIR) and anomalous scattering techniques (MAD/SAD), or a combination of both methods (MIRAS/SIRAS), which require the attachment of a heavy atom and/or the presence of anomalous scattering atoms, respectively, to the protein in the crystal. If parts of the structure or the structure of a close homologue are known, phases can be obtained by molecular replacement (MR). In this study, molecular replacement was used to obtain initial phases.

Molecular replacement is possible when parts of a protein structure or the structure of a close structural homologue of a protein are already known (rmsd <2). The phase angles of the unknown structure are thereby obtained from the known structure. For this, the known model has to be rotated and translated into the electron density of the unknown structure. The replacement is a 6-dimensional search problem (or two 3-dimensional searches), which can be solved with the Patterson function. The Patterson function is the Fourier transformation of the measured intensities (its squared reflection amplitudes $|F^2|$), which do not depend on phases as the phase angle is 0°. During translation and rotation search, the Patterson maps of the model structure and of the crystal diffraction data are compared. The derived coordinates of the molecules in the unit cell then allow the

calculation of new structure factor amplitudes and an estimation of the respective phase angles.

2.5.5 Structure refinement and ligand fitting

Refinement Model refinement is an iterative process of cycles of real- and reciprocal space refinement steps. The aim of refinement is to obtain a more and more accurate model of the crystallized macromolecule. The refinement process is implemented to improve the agreement and so minimize the difference between the calculated and observed structure factor amplitudes $|F_{\text{Obs}}|$ and $|F_{\text{Calc}}|$ by optimizing the parameters of the overall model, which consists of the atomic coordinates, the occupancies, and the temperature factors (B factors) of each atom of the macromolecule as well as atoms belonging to other ordered molecules (water, ions, ligands) in the ASU. Note that $|F_{\text{Obs}}|$ is available from the recorded data and that $|F_{\text{Calc}}|$ is obtained by a Fourier transform of the current model. Mathematically, the refinement process is performed by fitting the a model $|F_{\text{Calc}}|$ to the experimental data ($|F_{\text{Obs}}|$). The model parameters are adjusted during the fitting process in order to create a fit that deviates as little as possible from the experimental data.

$$R = \frac{\sum |F_{\text{obs}}| - |F_{\text{calc}}|}{\sum |F_{\text{obs}}|} \quad (5)$$

The progress of refinement is monitored by the so-called R (residual or reliability) factor R_{work} . The upper equation implies that if the quality of the model is increased during a single refinement cycle (that consists of a real- followed by a reciprocal refinement step), the R_{work} value should decrease.

Care must be taken at this point not to overfit the data. Overfitting happens if too many parameters are introduced into a model. To judge at which ratio the overfitting starts another R factor, the R_{free} , was introduced that can be calculated in the same way as R_{work} . For the calculation of R_{free} a portion of 5 - 10 % of the overall reflections is set aside. These free reflections are not included in the crystallographic refinement process of R_{work} . This means that the fitting program can adapt the model parameters to the 90 - 95 % of the reflections, while the same is not possible with the free reflections that are basically hidden from it. Nevertheless

a properly parameterized model after fitting also has to properly predict the free reflections. If after fitting, the free reflections are less well described by the model this indicates overfitting. In the final model the R_{work} and R_{free} values should ideally not deviate more than 5 % from each other. Real space refinement was performed in COOT. phenix.refine and autoBUSTER were applied for restrained structure factor amplitude refinement in Fourier space. Such refinement programs use the maximum likelihood refinement method, which weighs the model parameters based on the likelihoods of both chemical correctness, like agreement with known bond length and dihedral angles and correlation with the experimental diffraction data.

For structure refinement the selection of model parameters is very important. They should give a good description of the experimental data as possible while retaining a realistic data-to-parameter ratio. The number of refinement parameters can be reduced by using collective variables rather than independent atomic variables. The TLS parameterization for describing the translation, libration and screw-rotation displacements of a pseudo-rigid body and non-crystallographic symmetry (NCS) restraints were also used for the refinement process. NCS can be used to provide additional symmetry relationships between atoms that cannot be explained by the crystal symmetry. The correspondence of identical copies of the molecule is assumed to be perfect and the model does not allow any variation between them. Basically the number of parameters in the model decreases by the number of identical copies in the asymmetric unit. Further information about the refinement procedure can be found in crystallographic textbooks [101, 30, 81].

2.6 Single-particle cryo-electron microscopy

Several techniques are available for the determination of three-dimensional structures of biological macromolecules, including X-ray crystallography, nuclear magnetic resonance (NMR) and Single-particle cryo-electron microscopy (cryo-EM). Compared to other structural techniques, cryo-EM has the advantage that the amount of protein required is extremely small and that the protein can be used in aqueous solution. In addition, no formation of crystals is necessary, which is particularly advantageous for large, flexible or membrane proteins. Even though the first electron microscope was developed as early as 1931, this technique has

undergone a real revolution in the last 10 years in terms of maximum achievable resolution. In recent years, structures with sub-atomic resolution have been routinely published and cryo-EM has enabled the structural characterization of large protein complexes and membrane proteins that were previously difficult to access with the other established methods.

2.6.1 The Electron Microscope

The maximum resolution that we as humans can see with our naked eyes is limited. We humans can no longer resolve structural details smaller than a few hundred micrometers. Therefore, the development of the first magnifying lenses and light microscopes was a big step forward, especially in biology, and enabled the visualization of previously invisible microscopic features as the composition of tissues and individual cells. However, the maximum resolution of all microscopes is strongly limited by the wavelength of the light source used. The term resolution thereby describes the minimal distance at which two points (at specimen level) may still be distinguished as such (e.g. in the magnified image). The physical relation which describes this limitation of resolution is described by the Abbe diffraction limit, which describes the resolution limiting correlation between the illuminating wavelength and the optical properties of a microscope.

$$d = \frac{\lambda}{2n \sin(\alpha)} \quad (6)$$

More precisely, the principle states that two separate objects in the projected image can only be resolved as such if the distance (d) between them is greater than or equal to the wavelength (λ) divided by the double numerical aperture of the lens ($\sin(\alpha)$). Even if we assume perfect and faultless instrumentation, the maximum achievable resolution would only be half of the wavelength, which would correspond to only a few hundred nanometers using a light microscope. This resolution limits the light microscope to the visualization of structural features within a cell to the individual organelles.

In structural biology we aim to reveal atomic details of macromolecules, Hence, it becomes obvious that a diffraction-limited system, like the light microscope, is physically not capable of e.g. resolving the distance of two carbon atoms. For

visualizing two organically bonded carbon atoms that are typically situated $0.12 - 0.15$ nm apart, an illuminating wavelength of at least 0.3 nm would be required. Glass lenses, however, cannot effectively manipulate electromagnetic radiation at wavelengths smaller than 200 nm. Hence, in order to visualize the atomic details of macromolecules, as proteins, the utilization of a different light source and the development of a lens that focuses these waves was essential to achieve atomic resolution. The discovery of wave-particle dualism in 1924 and the subsequent development of an electromagnetic lens in 1928 led to the patenting of the first electron microscope in 1931 by Ernst Ruska and Max Knoll. Even though the imaging capability of transmission electron microscopes (TEM) improved tremendously within the last 80 years, the overall architecture of a modern TEM resembles still the first ones (Figure 17).

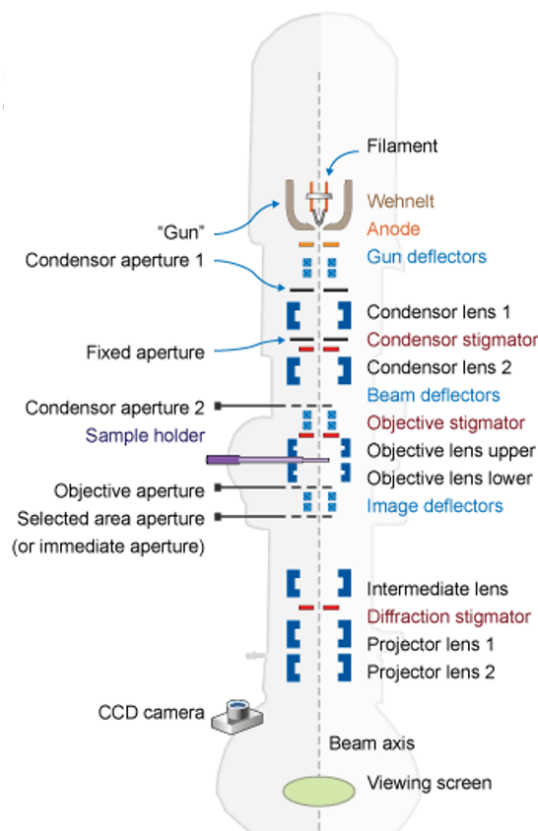


Figure 17: Scheme of a typically used TEM is shown with all essential components: Scheme of a typically used TEM is shown with all essential components. (The figure was adopted from [77])

In fact, the structure of an electron microscope is not very different from that of a light microscope: at the top of the column there is a light source (here electrons), followed by the condenser lens system which ensures the perfect illumination of the sample, the next part is the specimen holder, followed by the objective lens which produces the first image of the sample, which is magnified to the desired size by a set of projector lenses and finally falls onto a detection device which digitizes the image information. However, there are still very important differences in the design of a TEM compared to the conventional light microscope, which I will discuss in the next subsections.

The electron source Beginning with the source of illumination, there are three different kinds of electron sources. The electron emitting part of the assembly is furthermore frequently described as the cathode of a microscope. Historically, heated tungsten filaments or lanthanum hexaboride (LaB6) crystals are used to provide the electrons required for imaging by emission into the liner tube of the microscope column. In order for the energy to be large enough for the electrons to leave the metal, the filament must be heated to about 3000 °C in a high vacuum that prevails throughout the column of the microscope. More recent devices, however, instead feature an ultra-thin tipped, zirconium oxide-coated tungsten crystal that is operated as field- or Schottky emitter in order to extract a temporally and spatially more coherent beam of electrons at desirably high currents [109].

Extracted by a positive potential difference between the tip of the emitter and an anode, emitted electrons are accelerated by an electric field with several hundred kV and focused by a hole in the negatively charged anode surrounded by a negatively charged cup (the Wehnelt cylinder). Since the wavelength of an electron is directly correlated to its momentum (hence, its mass and velocity), acceleration is required to obtain electron radiation of the desired wavelength and high energy. The latter is practically achieved in the microscope by exposing the emitted beam of electrons to an increasingly positive electric field that is created by a potential difference applied perpendicular to the path of flight. Acceleration voltages of around 300 kV are currently utilized in high-end equipment to generate electron radiation of approximately 2 pm in wavelength. Thus theoretically allowing to reach sub-angstrom resolution. The accelerated electrons are then ready to be

used for imaging, in analogy to the photons that are emitted from a light source in an optical microscope.

Most state-of-the-art electron microscopes are equipped with a field emission gun (FEG) that is operated at a temperature of 1700-1800 K and optimised for brightness (XFEG). In order to optimise the source for its energy spread, a so-called 'cold' FEG (CFEG) may be operated at room temperature instead. Compared to XFEG, the CFEG has a much smaller energy spread, which leads to an increased SNRs at high spatial frequencies. Whereas the differences are small for resolutions worse than 2 Å, the use of the CFEG boosts the CTF at resolutions below 2 Å and facilitates structure determination in atomic detail [83].

The condenser lens system The accelerated electrons must be deflected by electromagnetic coils and lenses to obtain a magnified image of a sample. Not only an external electric field (as used in acceleration) can influence the propagation of an electron through space, but also a magnetic field by exerting the Lorentz force. The trajectory of each electron wave is affected when a magnetic field is generated in the immediate proximity of an electron. In fact, electron-optical elements create a specifically shaped magnetic field by sending an electric current through wire coils. Assemblies, which induce a spherical magnetic field, therefore ultimately behave like an electromagnetic lens and have the ability to condense or deflect incident electron radiation. The refractive power of an electromagnetic lens depends directly on the strength of its magnetic field, so both can be adjusted by changing the current sent through the wire coils within the element. Compared to glass lenses, electromagnetic lenses offer the possibility of adjusting the refractive power.

As we now continue our path through the microscope column, the accelerated electron beam is directed into an array of two or three electromagnetic condenser lenses, preparing the beam for optimal illumination of the sample. Precise shaping of the beam to fine-tune the illuminated area is facilitated by the interaction of the condenser lenses, which are operated with adjustable refractive powers and various exchangeable apertures. By combining a fixed diameter aperture with the adjustable power of certain lenses within the condenser lens array, the coherence and brightness of the incident electron illumination can be adjusted by physically blocking fractions of the electrons initially emitted by the electron source.

Objective lenses and specimen holder Once the coherency characteristics, dose and shape have been optimized, the beam enters the upper part of the objective lens, which is physically located directly below the condenser lens system. The objective lens itself then images the sample.

The sample holder (stage), which can be moved in x, y and z direction and, depending on the model, also tiltable, holds the sample, which is usually applied to a thin metal grid of 2-3 mm diameter. This is then inserted between these two parts of the objective lens. The so-called upper and lower pole pieces of the lens then precisely shape the magnetic field to guide the electron beam through the pole piece gap and the sample. Since the emerging wave now contains the spatial information of the imaged sample area, the electron-optical properties of the objective lens must be particularly well adjusted and monitored to avoid aberrations in the final, recorded projection.

Intermediate and projector lenses Now the virtual image of the sample is physically carried along in the scattered electron wave and can then be magnified in a setup comparable to a light microscope. An arrangement of intermediate lenses magnifies the virtual image by manipulating the convergence and aperture angles of the beam. In contrast to a light microscope, the desired degree of magnification can be freely determined without changing the hardware, since the refractive power of electromagnetic lenses can be adjusted. Once brought to the desired magnification the emergent beam passes through a final projector lens that eventually adapts the geometry of the beam in order to properly expose a downstream detector or fluorescent screen.

Electron Detectors The electron wave, which previously interacted with the sample and thus carries its spatial information, now hits a detector, which records and digitizes this information. If wavefronts hitting the surface of the detection device are then recorded at a defined spatial position on the detector and can be digitized after readout. However, together with the recorded signal, each detector inevitably adds additional, signal-independent intensities to the final image, which are commonly classified as noise. A critical quality measure of the readout signal is therefore given by the detector's detective quantum efficiency (DQE). The DQE is

defined by the square of the ratio of output signal to noise (SNR) to that of the input SNR. Consequently, the DQE describes how well a detector is capable of restoring the characteristics of an original input signal in relation to that which is finally read from the device after recording. Therefore, DQE values close to one represent an almost perfect signal recovery, while values close to zero indicate that a signal can hardly be distinguished from noise.

In the past, photographic film was used for the image acquisition in electron microscopy. Electrons darken a film material through specific chemical interactions with its substrate. While photographic film offers good imaging properties and a high DQE in many imaging scenarios, its physical handling and throughput is extremely tedious. The use of photographic film has been replaced by the emergence of other detection devices, which allow faster, more convenient and higher throughput data acquisition. The first digital detectors used were CCD (Charge Coupled Device) chips, which are excited by photons generated by the impact of electrons on a thin scintillation material above the sensitive detection layer. The digital readout of the recorded signal offered a great efficiency advantage. CCDs, however, are not hard enough to endure direct electron irradiation at the doses required in electron microscopy, and so they have been replaced by improved complementary metal oxide semiconductor (CMOS) detectors, which eventually allowed the construction of a direct electron detector [72]. The latter then allowed for a removal of the scintillation material and a much thinner design of the active detection layer (i.e., “back-thinning”) to provided a significantly improved DQE compared to all other detection methods available to this date. In combination with a fast readout rate it thus became feasible to operate the detectors in several recording modes, allowing to further improve the quality of the data. Single electron counting and the possibility of reading out many frames (hundreds to thousands) per second improves the spatial accuracy of the recorded signals, thus significantly contributing towards the widespread adoption and success of electron (cryo-) microscopy techniques today [60].

The Column The entire column of an electron microscope constantly has to be under high vacuum, since electrons interact strongly with all kinds of matter, including gas molecules in the ambient air. Therefore, various vacuum pumps, e.g.

, turbo molecular and ion-getter pumps, are mounted on the microscope column in several stages and work in such a way that they remove as many contaminant molecules as possible in order to create local vacuums of up to 1×10^{-9} mbar.

2.6.2 Optical aberrations

In great contrast to light microscopy, lenses of an electron microscope are only shaped magnetic fields and contain no matter. Due to the nature of magnetic fields, not all imaginable lens shapes can be created by them. This leads to imperfections of the lenses resulting in severe aberrations. The most crucial of those are astigmatism, coma and spherical aberration (Figure 18). If two waves, propagating perpendicular to each other, have different foci, one speaks of astigmatism. If the wave front of the electron beam is not parallel to the optical axis when hitting a lens, comatic aberration will occur. Spherical lenses as they are found in an electron microscope are not able to focus all waves to single focal points. Waves closer to the optical axis will have a different focal point than those away from the optical axis. Here one speaks of spherical aberration. All of these lead to distortions of the images and need to be avoided as much as possible. Using a technique called coma free alignment [136], astigmatism and coma can be reduced to a minimum. This can even be improved by using a spherical aberration corrector [34].

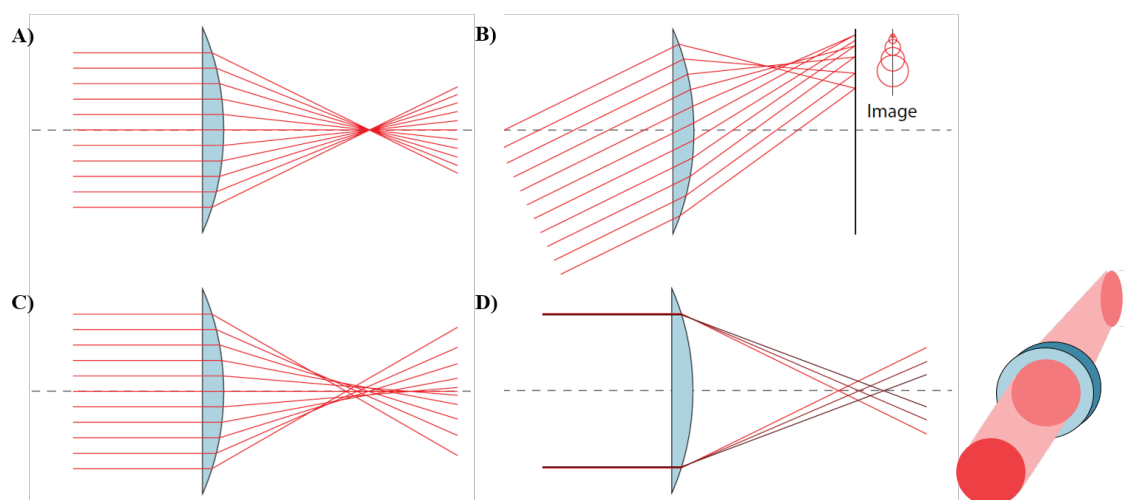


Figure 18: Most Important Aberrations for a TEM: Schematically the optical definition of the three most common aberrations are shown. The electron beam is depicted in yellow, the lens in blue and the optical axis in black. **A)** For a perfect lens, all parts of the beam are focused in a single point. **B)** Lenses with spherical aberration focus beam parts closer to the optical axis in a different point than those farther away from the optical axis. **C)** In case of misalignment, the beam will hit the lens, not in a perpendicular fashion and different parts of the beam will have different focal points. This results in coma. **D)** If waves that are perpendicular to each other have different focal points one speaks of astigmatism. A circular beam will thus be transformed into an elliptical one

2.6.3 Image and contrast formation

The image is formed through the direct interaction of the electrons with matter. An electron penetrating a specimen can either go through it unchanged, be deflected or absorbed and is recorded on the detector.

The formation and transmission of contrast is essential for the imaging and interpretation of any kind of microscopic data. The term contrast describes the magnitude of the difference in intensity of a certain signal compared to the signal coming from the immediate surroundings. A high contrast in imaging therefore increases the probability of distinguishing an actual feature from other features or noise in the immediate surroundings, and is therefore essential for drawing conclusions from the recorded data.

In TEM image formation there are two physically different principals of contrast formation, namely amplitude- and phase contrast that generally contribute towards

the overall image contrast that is finally recorded on the detector.

First, inelastic scattering describes the physical principle, when electrons collide or nearly collide with a nucleus, they transfer energy to the specimen this. This energy transfer can result in knock-on of nuclei, specimen ionization, X-ray emission, formation of free radicals or secondary electron scattering. All of them will damage the specimen and contribute to the noise in the image. Due to those effects, the specimen cannot withstand high dosage of electrons and thus the resulting SNR is low. While illuminating a sample, some of the illuminating radiation is either absorbed in various ways or deflected at high scattering angles far away from the optical axis by certain, mostly dense features within the specimen. Since some of the illuminating radiation has now been removed from the imaging process, the corresponding positions in the final image appear to be depicted darker in general (of lower intensity), with respect to their more intensely illuminated surroundings [55]. Hence, inelastically scattered electrons contribute to the so-called amplitude contrast. As inelastically scattered electrons are scattered to high angles and they can partly be removed by an objective aperture or energy filters.

Second, electrons can also be deflected by the specimen without losing energy, this principle is called elastic scattering. Those electrons will contribute to the contrast in the image and do not harm the molecules and are thus favored interactions. However, inelastic scattering can by no means be avoided and is even three times more frequent than elastic scattering. Moreover, the deflection angles of elastically scattered electrons are relatively small. The distance travelled (i.e., path length) of these refracted parts of the wave, however, changes, therefore introducing a phase shift between the scattered and unscattered parts of the formerly plane, incident wave [97]. Since the density of the biomolecular specimen (1.33 g cm^3 for protein) is slightly larger than the one of the surrounding ice (0.92 g cm^3), the phase shift is stronger in the specimen than in the ice and thus location dependent.

Image formation in cryo-EM is primarily by phase contrast, although between 7 and 10% of image contrast is from amplitude contrast. The sample in a TEM is modified by a point spread function, often referred to as contrast transfer function, which actually equals the point spread function in Fourier space. For micrographs recorded in-focus, the CTF attenuates low resolution features that are necessary to distinguish the proteins from the background, due to the very low contrast (Figure

19). A commonly used method for enhancing the phase contrast over certain spectral ranges is increasing of the defocus. Typically defocus values between -0.7 and $-2.5 \mu\text{M}$ are used. Yet, under defocused conditions, the CTF modulates the image information, which has the consequence that the contrast at higher spatial frequencies is eliminated, attenuated or reversed and the image information is delocalized, since each point in the ideal image is convoluted with the oscillation point spread function.

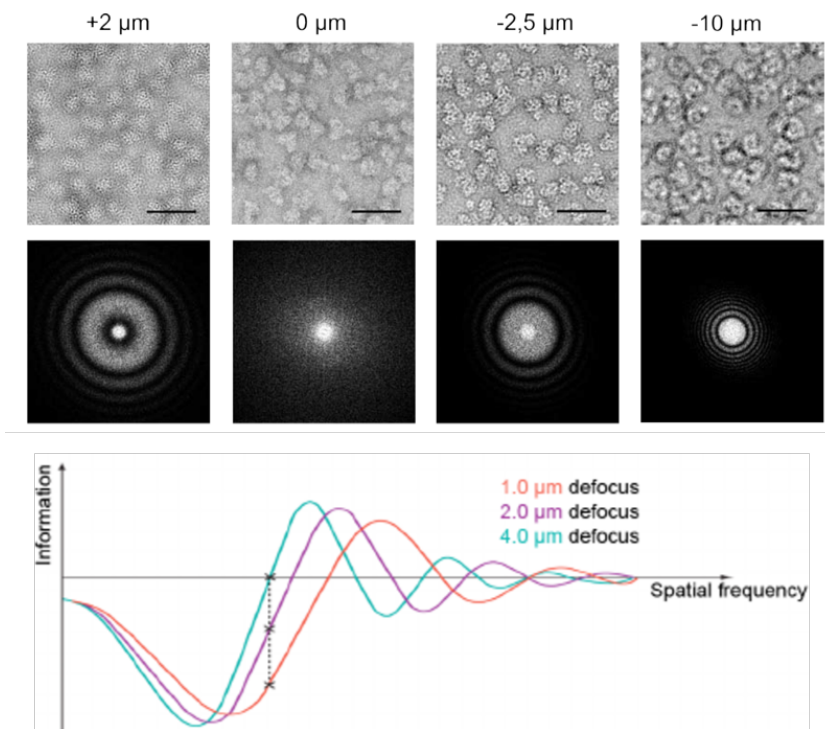


Figure 19: The effect of defocus: **A)** The negative stain images of a protein complex at different focus values. Upper row shows a micrograph at the given focus value. Positive values represent overfocus, negative values underfocus. In the lower row, the power spectrum of the respective micrograph is shown. The higher the focus, the closer are the Thon rings. **B)** A CTF has an oscillating form with increasing frequency and decreasing amplitude – i.e. there are contrast reversals, spatial frequencies where no information is transferred (zeroes) and attenuation of high- resolution information. Only by combining data at different degrees of defocus can full restoration of information at all resolutions be achieved.

While higher defocusing improves contrast, it comes with the tradeoff of increased fluctuations in the CTF, which makes accurate estimation and correction more difficult and thus limits resolution. Further it also causes increased image

delocalization, so that particle images in larger windows must be extracted to capture this information. However, it is possible to compensate for the effects of the CTF in computational image processing if some parameters of the TEM are known and the defocusing can be estimated accurately. During computational image reconstruction, it is possible to correct for the effects of the CTF provided that some parameters of the TEM are known and that the defocus can be accurately estimated.

In summary, the defocusing of the beam leads to an additional phase shift which allows the recording of phase contrasted image with visible amplitudes. To enable the calculation of a high-resolution 3D reconstruction, a data set covering a range of defocusing values must be collected to compensate for the loss of information caused by the CTF.

2.6.4 Sample preparation under cryo conditions

As described above, rapid freezing of the biological sample is needed to keep the biological sample in its hydrated state [25]. In more detail, the purified sample is pipetted as a small volume onto a grid designed for cryo-EM. These grids are often made of copper, and are covered by a carbon film with a regular or a random distribution of holes. The grid can influence the orientation of the macromolecule and can even affect the amount of sample that is embedded in ice. For a successful high-resolution structure determination, an equal distribution of orientations and a high amount of particles that are not aggregated in ice is preferred. Before sample application the hydrophobic carbon-coated grids are made temporarily hydrophilic with ionized gas molecules in a plasma cleaner. After applying the sample onto the carbon-coated grid, the grid is plunge frozen into a cryogen, such as liquid ethane, which is cooled to $-180\text{ }^{\circ}\text{C}$ through liquid nitrogen. The water molecules are transformed into a vitreous ice state before forming crystalline ice because of the high cooling rate of $100,000\text{ Cs}^{-1}$. Vitreous ice does not affect the density of the macromolecule or the interactions between the biological sample. Importantly, vitreous ice keeps the sample very translucent making it the perfect sample for cryo-EM data acquisition [25]. The plunge frozen sample needs to remain at $-180\text{ }^{\circ}\text{C}$ during the entire cryo-EM data acquisition to stay fixed onto the grid.

2.6.5 Single particle data processing

Any micrograph provides the two-dimensional (2D) projections of a three-dimensional (3D) object of interest. In the process, the entire density distribution of the 3D object is projected along one specific projection axis into a single 2D image [92].

In most applications (non-tilted acquisition) the angle at which a 3D particle's appearance is projected onto a detector is solely dependent on the orientation of the particle on the grid. In order to reconstruct a 3D model of the initially imaged particle, its projections need to be recorded at various projection angles [92]. On a cryo-EM-grid, the particle surfaces interact with the grid substrate, ideally in a non-specific way. In the ideal case, this results in a random distribution of the particle orientations and thus projections of individual particles are recorded at ideally random angles on each micrograph and can therefore be used for 3D reconstruction. Since many images of single protein particles are recorded and utilized, the procedure is commonly described as single particle analysis (SPA). Extensive image processing is required to reconstruct and analyze the 3D density map of a macromolecular complex from the 2D projections recorded in the electron microscope. In the following sections, therefore, the most important procedures are briefly introduced.

Micrograph quality control and pre-processing With today's direct detectors, not only one image is taken during exposure, but several images can be captured in succession (movies) at very short exposure times. This allows dose fractionation and correction of beam-induced motion by aligning each image of the same frameset with respect to the others. The latter is usually achieved by a choice of software packages and effectively reduces the effects of beam-induced motion blur or charging that would otherwise degrade image quality [71]. The resulting stacks of the aligned images are then averaged and dose-weighted to improve the signal-to-noise ratio of the final micrograph and at the same time optimize the representation of high-frequency spatial information in the data [139]. This first step of image preprocessing is generally called motion correction and dose weighting.

The pre-processed, averaged and doseweighted newly synthesized micrographs are further processed using CTF-correction. As already mentioned, certain aberrations

tions are transferred into the image which have to be corrected later. In addition, the signal recorded on each micrograph is usually derived from the phase contrast and therefore always modulated by a CTF. For high resolution 3D reconstruction purposes, however, an eventually homogeneous signal distribution over all spatial frequencies is extremely important [141]. The so-called power spectrum of a micrograph is calculated by transforming the real space image information mathematically to reciprocal, or Fourier space. The power spectra is used to fit an approximation of the respective CTF for every micrograph. As the CTF is directly dependent on the focal height of the recording, fitting the function to the real data also reveals its respective defocus parameter, the amount of astigmatism and the CTF zero crossings can be precisely mapped [125]. This analysis, usually automatically performed by software, thus allows the application of basic image processing procedures such as phase flipping or astigmatism correction [138]. Specifically the flipping of phases that would otherwise have resulted in a negative image contrast composes new images of the particle projections that consequently feature an all-positive image contrast. The described procedures are thus absolutely essential to eventually retrieve the high spatial frequency information from any phase contrast transfer function modulated image [16].

Particle picking and extraction Once the micrographs are Motion- and CTF-corrected, the position of all single particle projections on the micrograph must be determined; a process commonly referred to as particle picking. Due to the low SNR, and varying ice thickness, particles are barely visible and often artefacts on the grid like ethane or ice crystals can be easily confused as particles. Only a few years ago, picking was done exclusively manually. Nowadays, a large number of software packages are available. Those use either template-free approaches [137] [102], template matching algorithms [14] image statistics [123], machine learning [8] [52] or combinations of several methods to identify the particles. None of those performs perfectly on every data set, but all have their advantages. Thus, additional steps to remove artefacts or false positives from the data set are required. As soon as the particle coordinates are obtained, every projection is cropped from its original micrograph at a box size that is approximately 1.5 - 2x the diameter of the particle. All further basic image-processing procedures are then performed on these stacks

of particle images only.

Particle classification and averaging As previously explained, the low dose imaging that is commonly applied during single particle image acquisition inevitably results in a noisy representation of the recorded image. One of the most critical challenges in single particle cryo-EM image processing is therefore to improve the generally low signal-to-noise ratio (SNR) in the recorded image, which is inevitable when using low dose exposure techniques. Averaging of multiple low dose images however is known to generate micrographs of satisfactory signal-to-noise ratio [38] [40]. In single-particle cryo-EM the projections of particles are usually recorded at random projection angles, however, a careful alignment and classification of all images is obligatory before averaging by summation. After alignment and classification, the same kind of projections thus show the same features at the same position while the noise in the image is generally distributed randomly. Hence, after averaging, the signal of particle features increases proportionally with the number of images used, while the signal resulting from random noise is cancelled out in a similarly proportional manner. The resulting stable class averages should now represent all the different projection directions of the molecule present in the data set. They should be mass centered, and thus, the translational degrees of freedom are determined.

Many algorithmic approaches have been developed in order to align and classify sets of noise contaminated single particle projections. Methods that are based on maximum likelihood estimations and Bayesian statistics are gaining importance in the field and are nowadays used on a routine basis [102]. Finally, 2D class averages of sufficiently improved SNR and best possible structural homogeneity are required to proceed to angular reconstitution and 3D reconstruction steps.

Angular reconstitution and 3D reconstruction In order to reconstruct a 3D volume from its 2D projections, the latter need to be back projected while spatially arranged at their corresponding, original projection angles (Figure 20). In effect, a virtual 3D model of the originally imaged object is created at the centre of an imaginary projection sphere, which can then be analysed at various threshold levels that again represent the density distribution of the original object.

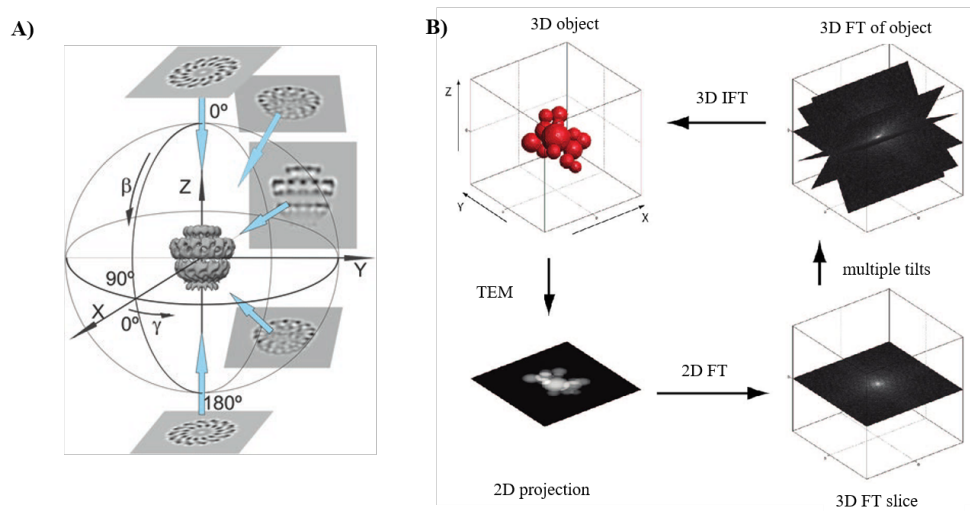


Figure 20: 3D reconstruction in real- and fourier space: A) Projection sphere illustrating the relationship between 2D projections and their 3D origin. Various 2D projections of the same 3D particle that is oriented in the centre of the sphere are illustrated. The 2D projections are thereby arranged on the arbitrarily sized projection sphere according to their correctly determined projection angle (Euler angle) [18]. **B)** Most computational 3D reconstructions are calculated in fourier space and follow the Projection-Slice theorem depicted in this scheme. FT denotes the Fourier transform, and IFT denotes the inverse Fourier transform. By combining projections recorded at multiple tilts the 3D FT of the object is probed. An inverse Fourier transform then reconstructs the 3D object [28].

Although the method described above is well characterized in theory and can be efficiently calculated in reciprocal space, its application to real electron microscopic data is not trivial. The most difficult task in this respect is the (re)assignment of projection angles to 2D images, which were randomly oriented on the EM grid. Although the entire 3D density distribution within a 2D projection of a 3D particle is preserved, the relative angular relationship of this projection to the original particle is lost. However, knowledge of the exact projection angles is crucial for the success of any back projection attempt in 3D reconstruction [92].

Mostly, no initial model is available and thus the projection angles have to be derived directly from the data itself. A purely mathematical approach, needing no extra information besides the data set itself is called angular reconstitution. It is based on the Fourier slice theorem, which says: “The Fourier transform of a parallel 2D projection of a 3D object equals a central section through the Fourier transformation of the 3D object. It follows: If two projections are derived from

the same 3D object, their 2D Fourier Transformations will share at least one central section through the center of the transformed image". Already a set of three projections gives rise to three common lines, which is sufficient to determine the angular orientations. While equal line sections are hard to determine in Fourier space, a real space analogous theorem, the common lines theorem, was developed [119]. If one transforms the common line from Fourier space back into Real space, they represent 1D projections of the original 2D projections. Since they are equal in Fourier space, they also have to be equal in real space. One can thus derive that two 2D projections from the same 3D object will share at least one 1D projection. With this, one only needs to find this common line. To do so, Radon transformations, also called sinograms, are calculated. These are the set of all possible 1D projections of a given 2D image. In a second step, all combinations of 1D projections are compared for similarity and thus the Euler angles are determined. Angular Reconstitution in general works to a satisfactory extent if the input 2D projections all belong to the same 3D object and are of sufficient SNR. Once 3D information concerning the particle of interest is available, e.g. through initial attempts of angular reconstitution, a crystal structure or any other model that is compositionally related, computed projections of this existing model can then be utilized as an alignment reference for the recorded data. Since the reference projections are computed, not empirically recorded, their angular relationship is known. All particles that are aligned to a projection of this kind may therefore be used at once in a 3D reconstruction with an angular relationship that originates from and is equal to that of the original reference projection [94]. The method is therefore named projection matching and reviewed in more detail here [23]. As an existing model is used as a reference, the procedure may likewise be utilized to iteratively refine a 3D structure against the data through consecutive rounds of alignment, 3D reconstruction and re-projection of the reconstructed volume. This procedure thus allows an iterative improvement of the back-projected 3D volume, hence, its re-projections, and consequently results in a more precise alignment of the recorded data to the computed reprojections of higher resolution during the next iteration. Maximum-likelihood based methods of classification in combination with projection matching procedures therefore allow the refinement of cryo-EM data to highest resolutions [102].

Resolution after 3D reconstruction Objective measures for the assessment of resolution are of great importance in evaluating the informative value of any reconstructed 3D volume. The optical resolution of the microscope does not necessarily equal the resolution of the 3D volume after 3D reconstruction. Instead, the point-to-point resolution theoretically obtainable in an ideal exposure of a 2D micrograph is further degraded by the low SNR in a typical cryo-EM recording, alignment- and aberration correction errors, and additional optical aberrations introduced by recording procedures that are optimised for speed (e.g. beam tilt induced coma) [93]. The resolution assessment of cryo-EM data after image processing therefore rather concentrates on the consistency of the result, which is generally an averaged image in the 2D classification scenario and a density map after 3D reconstruction. While a wealth of procedures have been developed over the years, the Fourier Shell Correlation (FSC) in 3D [37] are most commonly utilized in the field today. The FSC thereby represents a 1D function of the modulus of spatial frequency, where its values are computed correlation coefficients between two similar but independently reconstructed 3D volumes. Consequently, values of the FSC curve close to one represent a strong similarity between the two 3D volumes at a given spatial frequency while values approaching zero suggest a random, thus no correlation. A specific, somewhat arbitrary cut-off value (e.g. 0.5 or 0.143) is then used to determine the resolution [100]. Defined dataset refinement procedures and FSC cut-off values eventually represent the “gold-standard” of resolution determination [39]. The obtained numerical value thereby commonly represents spatial frequency (e.g. $1/\text{\AA}$ in units), while an inverse of this number is used to describe the apparent resolution in units of real space distance, e.g. \AA . Resolution estimations of this kind are additionally utilized during refinement procedures in order to prevent overfitting and to guide the process in general [102]. 3D maps may therefore be filtered and post-processed at their respective maximum resolutions without the risk of an over- or underestimation of the information content that is actually present in the data. Once the resolution of a reconstructed 3D model is evaluated, its numerical value is expected to represent a consistent and reproducible indication for the information content of the map. In general, it is accepted that resolutions worse than 30\AA solely describe the overall shape of a macromolecular complex in rough detail. In the range of $30 - 10 \text{\AA}$ it then becomes feasible to fit

and identify rigidly folded whole protein structures or their domains. A map with a 10 – 4 Å resolution range is expected to clearly reveal the shape of alpha-helices and beta-sheets, eventually separating the later and allowing an identification of the alpha-helix pitch at resolutions close to 4 Å [102]. Maps better than 4 Å in resolution are finally expected to reliably reveal densities for individual side-chain moieties, where resolutions of 3,2 Å or even lower values continuously increase the certainty of their fit, up to exposing true atomic detail at around 1 Å [83].

2.6.6 EM sample preparation for GCH1-GFRP complex

For complex formation hGCH1 and hGFRP was mixed using a 1.3 x hGFRP excess. The mixed proteins were diluted by 1:10 in complex buffer and incubated for 30 min at 4°C. The identification of suitable buffer conditions was key to the preparation of high-quality grids. The final puffer composition was identified using the ProteoPlex technology [39]. 100 mM sodium phosphate pH 5.5, 80 mM NaCl and 20 mM phenylalanine was used to form the stimulatory complex and 100 mM sodium citrate pH 5.75 and 0.1 mM BH4 (Sigma Aldrich; T4425) was used for the formation of the inhibitory complex. The two distinct protein complexes were purified using a Superose 6 Increase 10/300 GL column and the respective complex buffers. The respective complex fractions were pooled and concentrated up to 1-1.6 mg/ml. The purified samples were never kept at 4°C longer than 48 h prior to grid preparation. Shortly before grid preparation, the stimulatory complex was diluted with Phe containing buffers to 0.6 mg/ml so that the final buffer composition consisted of 50 mM sodium phosphate pH 5.5, 20 mM NaCl and 20 mM Phe. Furthermore, 0.1 mM 8-oxo-GTP (Jena Bioscience; NU-1116) was added. The inhibitory complex was diluted to 0.25 mg/ml and 40 mM sodium citrate pH 5.75 and 0.1 mM BH4. 3µL of protein solution was applied to freshly glow-discharged C-flat CF-1.2/1.3-4C Grids and plunge frozen in liquid ethane using a Vitrobot (Thermo Fisher).

2.6.7 Data acquisition and processing of GCH1-GFRP EM datasets

Micrographs were automatically recorded using EPU on a Titan Krios microscope (Thermo Fisher) operated at 300 kV equipped with a K2 direct electron detector

in electron counting mode at a nominal magnification of 130,000x, corresponding to a calibrated pixel size of 1.077 Å. Dose fractionated 8 s movies of 40 frames were recorded with a total electron dose of 55 e/Å² using defocus values of 1.0 - 2.4 µm. A total of 2698 micrographs was collected for the inhibitory dataset and 3121 images for the stimulatory complex. Whole-image drift correction of each movie was performed using MotionCorr [59]. The CTF was determined using CTFFIND4 [99] in the RELION 3.0 workflow [140]. Initially approximately 40,000 particles were manually picked with EMAN boxer [63] and subjected to 2D reference-free classification in RELION [140] to check the quality of the particle images and generate 2D class averages for autopicking in RELION. Approximately 350,000 - 750,000 particles with a box size of 250x250 pixels were extracted. Afterwards the dataset was cleaned by 2D- and 3D-classification. A low-passed filtered volume of the rat GCH1-GRFP crystal structures (1is7; 1wpl) was used as a starting reference for 3D classification. The stimulatory and inhibitory complexes were reconstituted from 122,275 or 254,907 particles, respectively, using RELION 3Dauto-refine. The refined particles were subjected to per-particle CTF refinement and Bayesian polishing in RELION 3.0 [140], yielding maps of 2.9 and 3.0 Å resolution determined by the gold-standard 0.143 Fourier shell correlation (FSC) criterion using the post-processing procedure in RELION 3.0. For both complexes the same mask was applied. Local resolution was estimated using MonoRes [121]. Structures of hGCH (1fb1), hGFRP (7acc) and rGCH-GFRP (1wpl, 1is7) were docked into our final cryo-EM maps using Chimera [39]. Docking of the individual subunits was improved by rigid body fitting in Coot. Model adjustment and refinement were performed iteratively in Coot [24] and Phenix [2], and the statistics were examined using Molprobit [129] until no further improvements were observed. The final model was also evaluated using FSC analysis against the map and using EMRinger [6] to compare the fit of the model backbone into the cryo-EM map. The model statistics showed good geometry and matched the cryo-EM reconstruction (Figure 7). The structure of the hGCH.hGFRP inhibitory and stimulatory complexes have been deposited in the Protein Data Bank (PDB; accession codes 6Z80 and 6Z85). The respective cryo-EM density maps have been deposited in the Electron Microscopy Data Bank (accession codes EMD-11113, 11114)

3 Results

3.1 Expression, lysis and purification of hGCH and hGFRP proteins

Plasmids encoding for either hGCH1- Δ 42-NHis, hGCH1-FL-NMBP or hGFRP-FL-NHis were transformed into E.coli BL21 (DE3) chemical competent cells. Large quantities of protein are necessary to carry out structural research and biophysical experiments. The hGCH1-FL-NMBP is a thrombin cleavable MBP-tagged construct and was therefore purified using amylose resin, while the other protein constructs have a thrombin cleavable hexahistidine tag and are purified over NiNTA.

3.1.1 hGFRP

Purification of hGFRP was performed as described in detail in the method section the used buffer compositions are listed in Table 3.

hGFRP-FL-NHis was expressed in E.coli BL21 (DE3) cells. Cells were cultured in LB medium at 37°C and protein expression was induced using 1 mM IPTG upon reaching an OD600 of 0.6. Figure 21 A shows strong overexpression of a band at approximately 10 kDa after induction with IPTG (Figure 21 A). This is hGFRP, which was identified by mass spectrometry analysis and is 11.86 kDa Da in size (tagged construct). Cells were cultured over night at 20°C before being harvested at 4 000 x g. For storage, pellets were flash frozen in liquid nitrogen. Afterwards, frozen pellets were thawed on ice and resuspended in lysis buffer. Subsequently, the cells were lysed by sonication and cell debris were removed by centrifugation. hGFRP seems to be soluble in the lysate supernatant as well as insoluble in the pellet (Figure 21 A). This could result from incomplete lysis due to lysing too many cells in too little buffer or due to expression of target protein in inclusion bodies. Nevertheless, the pellet was discarded and only the supernatant was used for further purification.

The supernatant was loaded on a spin column filled with 4 mL (for a 4 L cell pellet) previously equilibrated (Ni-NTA-loading buffer, Table 3) Ni-NTA slurry. Binding of the protein to the column material was performed for 10 min on a rotator. Extensive washing (Ni-NTA-elution buffer, Table 3) of the resin removes

the unbound bacterial protein. Afterwards elution with a imidazole containing buffer (Ni-NTA-elution buffer, Table 3) was performed. Multiple elution steps were necessary, until no more protein eluted from the column. The eluted protein already looks quite pure on the SDS PAGE (Figure 21 A) and the gel shows no target protein in the wash and flow-through, indicating that the column was not overloaded.

The His-tag of hGFRP was cleaved by thrombin digestion during dialysis while monitoring the cleavage efficiency as shown in Figure 21 B. After 42 h of incubation with 1.5 U thrombin, His-tag was cleaved almost completely and GFRP solution was purified by anion exchange chromatography (Figure 21 C/D). Fractions of the anion exchange chromatography show small contaminations of uncleaved his-tagged GFRP with a size of 11.8 kDa that are nearly completely vanished after size exclusion chromatography (Figure 21 D/F). Therefore, the protein volume was reduced up to 5 mL using a Amicon Ultra Centrifugal Filters with a 30 kDa cutoff and loaded afterwards on a SD200 (26/600) column. One single peak eluted at 239 mL which corresponds to a size of 60 kDa (Figure 21 E). hGFRP is known to form a 50 kDa pentamer in solution. As the SEC profile was mono-disperse and no difference on the SDS-Page fractions were visible all target protein containing fractions were pooled and concentrated to 10 mg/ml. The purification yielded approximately 6 mg protein per liter culture medium at an estimated purity of 98 % (based on SDS-PAGE).

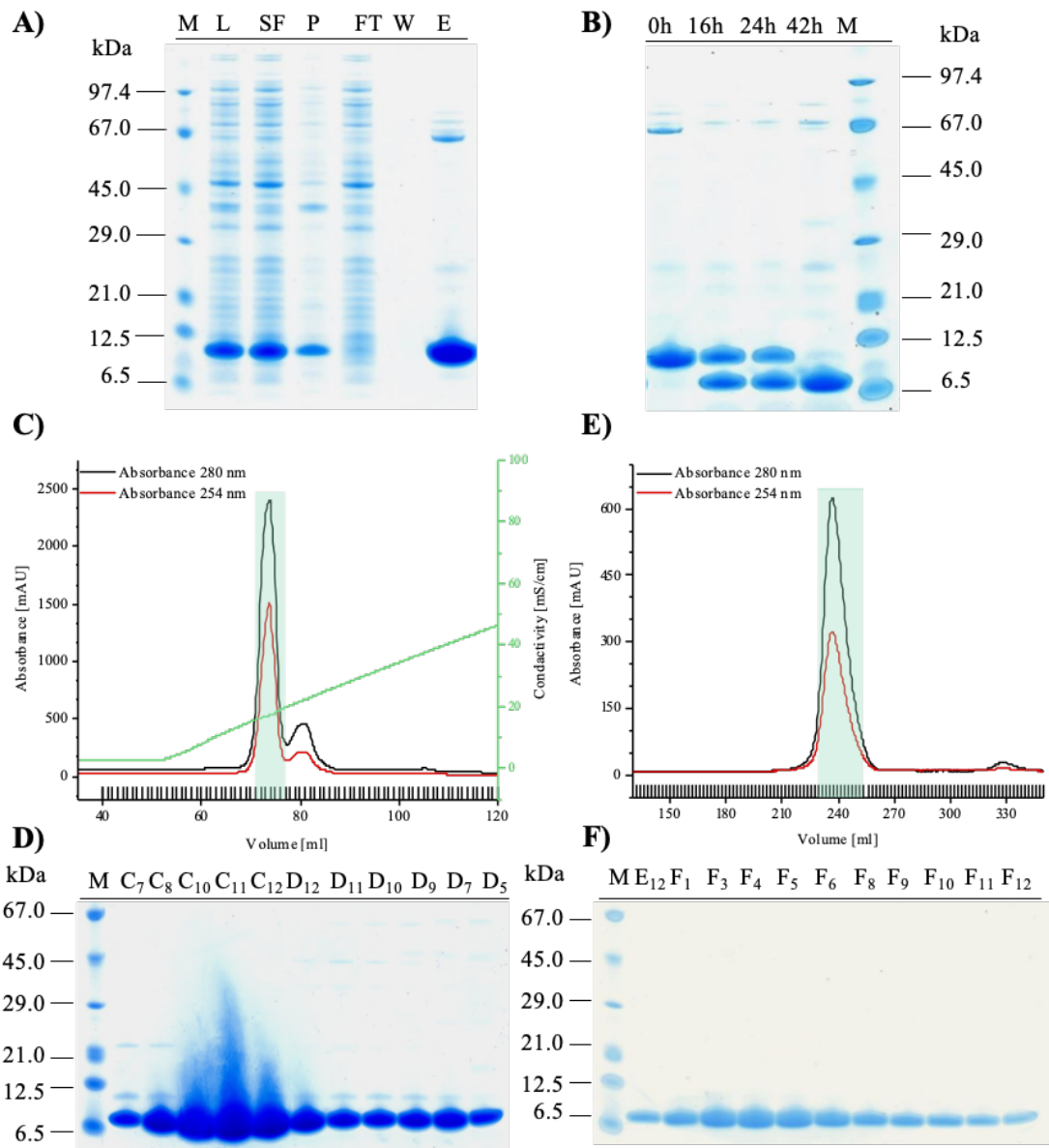


Figure 21: hGFRP-FL-NHis overexpression, lysis and purification: **A)** SDS-PAGE samples show over-expression and lysis of recombinant GFRP (11.8 kDa) and different steps of NiNTA purification. M = Ladder; L = Lysat; SF = Soluble fraction; P = Bacterial pellet; FT = Flow Through; W = Wash; E= Elution. **B)** GFRP His-tag cleavage using 1.5 U thrombin over different periods at RT. h = hours. His-GFRP = 11.86 kDa; GFRP = 9.98 kDa. **C)** Anion exchange chromatography profile of GFRP. Green highlighted fractions (F1-F12) were selected by **D)** SDS-PAGE for pooling and subsequent size exclusion chromatography. **E)** SEC elution profile shows monodisperse elution of hGFRP. Green highlighted fractions (C8-C12; D12) were pooled. **F)** SDS-PAGE of selected and pooled fractions from SEC.

3.1.2 $\Delta 42$ -hGCH1

The following section describes exemplarily the protein purification results by the example of the wild type $\Delta 42$ -hGCH1 construct. The purification of mutated constructs, like hGCH1- $\Delta 42$ -NHis-F122A, were conducted using the same expression and purification procedure and results looked comparable. hGCH1- $\Delta 42$ -NHis was also expressed in *E. coli* BL21 (DE3) cells. Cells were cultured in LB medium at 37°C and expression was induced with 1 mM IPTG upon reaching an OD600 of 0.7. Cells were cultured over night at 20°C before being harvested at 4 000 x g. Pellets were stored at -20°C. Afterwards, frozen pellets were thawed on ice and resuspended in lysis buffer. Subsequently, the cells were lysed by sonication and cell debris were removed by centrifugation. As previously seen with hGFRP (Figure 21 A), hGCH (Figure 22 A) seem to be soluble in the lysate supernatant as well as insoluble in the pellet. The pellet was discarded and only the supernatant was used for further purification. As $\Delta 42$ -hGCH1 constructs have a N-terminal hexahistidine tag, they were purified using pre-equilibrated 5ml HiTrap columns (GE Healthcare, GE17-5248-01) on an Akta system. The lysate was passed over the column material at a flow rate of 0.7 ml/min and then thoroughly washed. Afterwards the protein was eluted using elution buffer until the last wash fractions contain no detectable amount of any protein, confirming a sufficient purity of specifically bound proteins on columns or beads, whereas the elution fractions indicate a high enrichment and effective elution of the target proteins (Figure 22 B). $\Delta 42$ -hGCH1 purification was continued with a SEC to reach a high protein purity without significant contaminations. As expected, $\Delta 42$ -hGCH1 eluted in a monodisperse peak as a decamer of approximately 250 kDa. All target protein containing fractions were pooled and concentrated to 6 mg/ml and snap frozen in liquid nitrogen. The purification yielded approximately 4 mg protein per liter culture medium at an estimated purity of 95 % (based on SDS-PAGE).

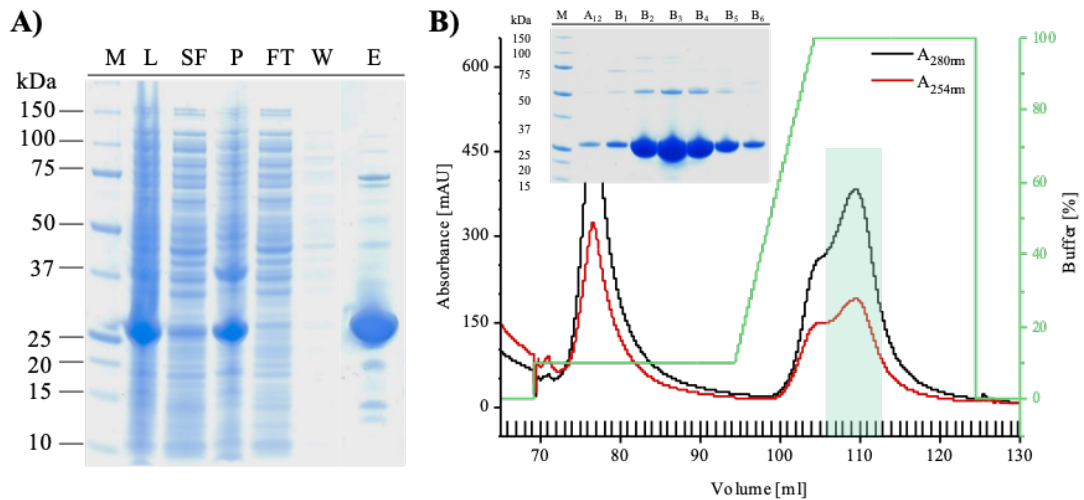


Figure 22: Overexpression, lysis and purification of hGCH1- Δ 42-NHis construct: **A)** SDS-PAGE monitoring the cell lysis and NiNTA purification of Δ 42-hGCH. SF = Soluble fraction; P = Bacterial pellet; FT = Flow Through; W = Wash; E = Elution; M = Ladder. **B)** Ni-NTA chromatogram. The green highlighted fractions (B₂-B₅) were selected by SDS-PAGE for pooling and storage at -80 °C.

3.1.3 Full-length GCH1

hGCH1-FL-NMBP was recombinantly expressed in *E. coli* by IPTG induction. The obtained bacterial pellets were lysed by sonication and centrifuged to separate cell lysate and bacterial cell debris. hGCH1-FL-NMBP was purified using pre-equilibrated 5ml MBPTrap columns (GE Healthcare, GE28-9187-80) on an Akta system. The lysate was passed over the column material at a flow rate of 0.7 ml/min and then thoroughly washed. Afterwards the protein was eluted using elution buffer until the last wash fractions contain no detectable amount of any protein, confirming a sufficient purity of specifically bound proteins on columns or beads, whereas the elution fractions indicate a high enrichment and effective elution of the target proteins (Figure 23 AB). Afterwards, the hGCH1 full length protein was cleaved from their MBP-tag by TEV-cleavage (Figure 23 A). The MBP-tag was cleaved nearly completely, leading to a shift of the protein band from 70 kDa to two bands at 42 kDa for the MBP-tag and 28 kDa for hGCH1 as seen in Figure 23 A. hGCH1 and MSP were separated from each other either by reverse affinity purification or SEC and GCH1 shows no visible contaminations on the SDS-PAGE

(Figure 23 C). The SEC profile had a monodisperse shape and eluted, similar as the $\Delta 42$ -hGCH1 protein, at a volume which is corresponding to the size of a decamer. All fractions, which contained the target protein, were pooled and concentrated to approximately to 6 mg/ml. The purification yielded approximately 3 mg protein per liter culture medium at an estimated purity of 98 % (based on SDS-PAGE).

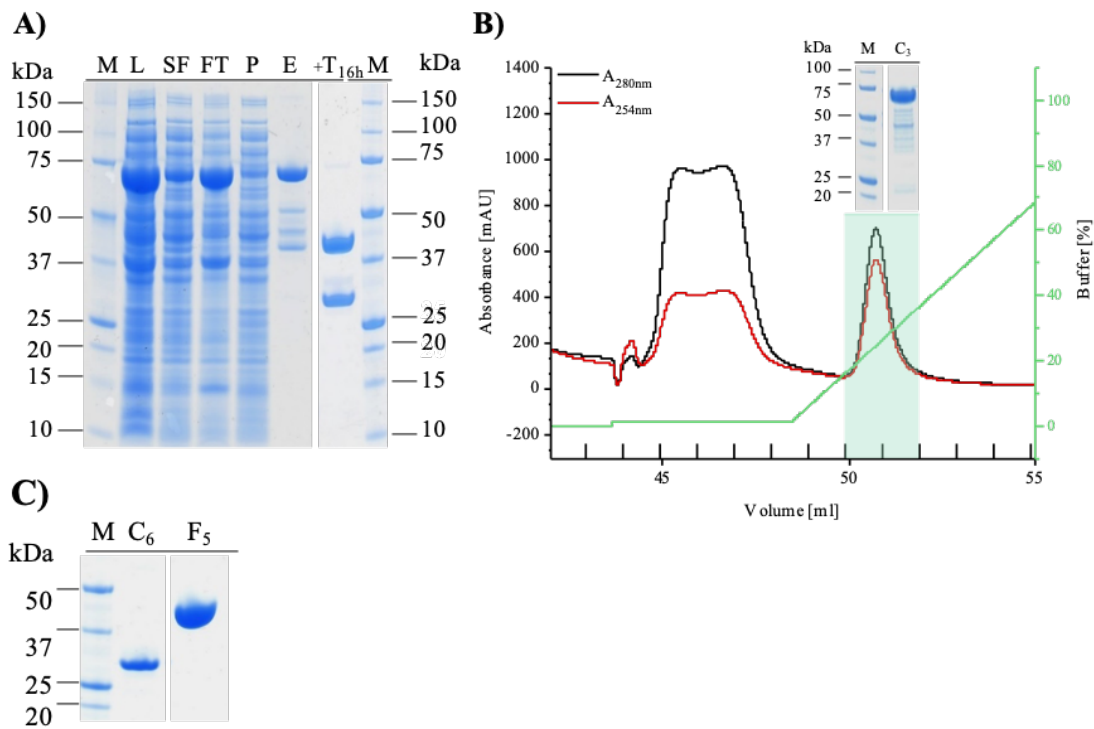


Figure 23: Overexpression, lysis and purification of hGCH1-FL-NMBP construct: **A)** SDS-PAGE monitoring the cell lysis and MBP-affinity purification elution before and after TEV-cleavage after 16 h incubation (+T16h). SF= Soluble fraction; P= Bacterial pellet; FT= Flow Through; W= Wash; E= Elution; M= Ladder. **B)** hGCH1-FL MBP-affinity chromatogram. Green highlighted fractions were selected by SDS-PAGE and pooled for the subsequent TEV-cleavage. MBP-tag= 41.7 kDa; hGCH1= 27.8 kDa. **C)** hGCH1 and MSP were separated from each other either by reverse affinity purification or SEC. C₆= hGCH1; F₅= MSP.

3.2 hGCH1-hGFRP complex formation

3.2.1 Optimization of the hGCH1-hGFRP complex

In order to improve the stability and monodispersity and thus improves specimen quality and ability to form well ordered crystals, a DSF based buffer screen using the ProteoPlex technology was used [13]. ProteoPlex is an advanced adaptation of the DSF technique, systematically explores stabilizing buffer conditions by using a sparse-matrix approach. An important advantage of ProteoPlex in comparison to classical DSF is that it allows to analyze multiple unfolding states in melting curves and the aim is to find a condition in which the target protein possesses a two-state unfolding behavior. This is especially useful for protein complexes, as their different components often offer distinct stability in standard buffer system. The ProteoPlex technology aims to stabilize the protein complexes in a way, that the complex melts together with the individual components.

For the analysis of the melting behavior the complex was not purified via SEC, but mixed in equimolar ratios and incubated for 30 min. The melting curve of the hGCH-hGFRP complex, when formed in a standard Tris buffer (150 mM NaCl; 25 mM Tris pH 7.4; 0.1 mM BH₄) showed multiple unfolding states and separate melting points for the two components of the complex (Figure 24 AB). Although the hGCH-hGFRP complex with its picomolar affinity is already very stable, we were able to identify buffer conditions in which the protein not only shows a melting point increase of 7-10°C, but also shows simultaneous melting of all components fitting the model of a two-state melting transition. 100 mM sodium phosphate pH 5.5, 80 mM NaCl and 20 mM phenylalanine was used to form the stimulatory complex and 100 mM sodium citrate pH 5.75 and 0.1 mM BH₄ (Sigma Aldrich; T4425) was used for the formation of the inhibitory complex.

The identification of suitable buffer conditions was key to the preparation of high quality grids and improved crystal growth. Figure 24 C-F shows the distribution of the inhibitory complex particles on a cryo-EM grid before and after buffer optimization. [13]. Using a standard buffer (150 mM NaCl; 25 mM Tris pH 7.4; 0.1 mM BH₄) the protein had a high tendency to form large aggregates on the grid, even though the protein complex eluted as a sharp monodisperse peak from SEC (Figure 24 D). The aggregates were even visible as large clouds at low magnification

(Figure 24 C). While the hGCH1-hGFRP particles, prepared in the optimized buffers, produced very clean grids with a good distribution of complex particles. Side and top views of the hGCH-hGFRP inhibitory complex are visible on the grid and all particles are clearly separated from each other.

Proteoplex based DSF screening, therefore did not only improve the melting behavior and melting temperature but also the monodispersity and distribution of the protein complex on EM grids. Further, about 50 % more crystals appeared in crystallization trials set-up with protein in low pH phosphate- or citrate buffers.

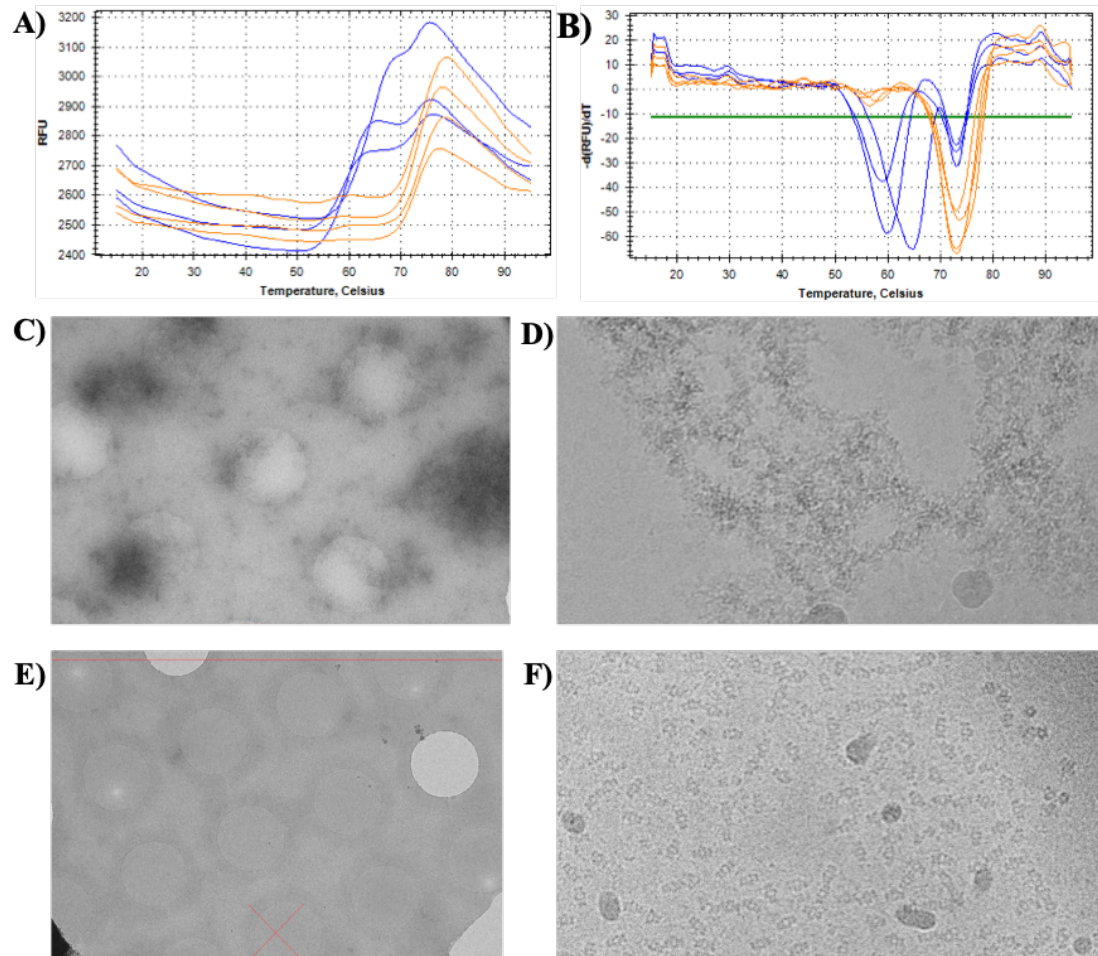


Figure 24: Buffer optimization of the hGCH-hGFRP complex buffer: **A)** DSF raw trace showing the melting trace of hGCH-hGFRP complex in standard buffer (blue) and in buffer optimized via the Proteoplex technology (orange). The non-optimized complex (blue) shows multiple-state melting behavior while the optimized (orange) curve resembles a two-state unfolding model. **B)** DSF first derivative traces showing the melting points of hGCH-hGFRP complex in standard buffer (blue) and in buffer optimized via the Proteoplex technology (orange). The non-optimized complex (blue) shows multiple melting points while the optimized (orange) curve only offers one local minima. **C)** Low magnification microscopic image of the foil holes of a C-flat CF-1.2/1.3-4C grid holding hGCH-hGFRP sample in standard Tris buffer. Cloudy aggregates are visible on an EM-grid. **D)** High magnification micrograph shows in large aggregates of hGCH-hGFRP forming in non optimized puffer. **E)** Low magnification microscopic image of the foil holes of a C-flat CF-1.2/1.3-4C grid holding hGCH-hGFRP sample in Proteoplex optimized buffer. Cloudy aggregates are visible on an EM-grid. **F)** High magnification micrograph shows single particles of hGCH-hGFRP complex with good distribution on EM-grids using the Proteoplex optimized buffer.

3.2.2 Formation and purification of the hGCH1-hGFRP complex

For complex formation hGCH1 (6 mg/ml) and hGFRP (10 mg/ml stock) was mixed using a 1.3 x hGFRP molar excess. The mixed proteins were diluted by 1:10 in complex buffer (100 mM sodium phosphate pH 5.5, 80 mM NaCl, 20 mM phenylalanine or 100 mM sodium citrate pH 5.75, 0.1 mM BH₄) and incubated for 30 min at 4°C. The buffers were optimized using a Proteoplex based DSF screen (section above) [13]. The two distinct protein complexes were purified using a Superose 6 Increase 10/300 GL column and the respective complex buffers. The elution profile shows the complex peak eluting at a volume corresponding to the size the hGCH-hGFRP while the uncomplexed hGFRP elutes as a smaller peak. The successful formation of the inhibitory or stimulatory hGCH-hGFRP complex can be monitored by the shifting of the hGCH peak towards higher molecular weight and simultaneous reduction of the hGFRP signal (Figure 25 AB). Strikingly, the hGFRP peak also shifts in presence of peak, which was unexpected (Figure 25 B). A possible reason for that could be the high concentration of phenylalanine which is changing the running behavior of hGFRP on the SEC column in contrast protein in absence of effector molecules. Only the three main-peak fractions of the complex peak were pooled in order to avoid the shoulder region. After SEC, the protein was concentrated to the desired concentration.

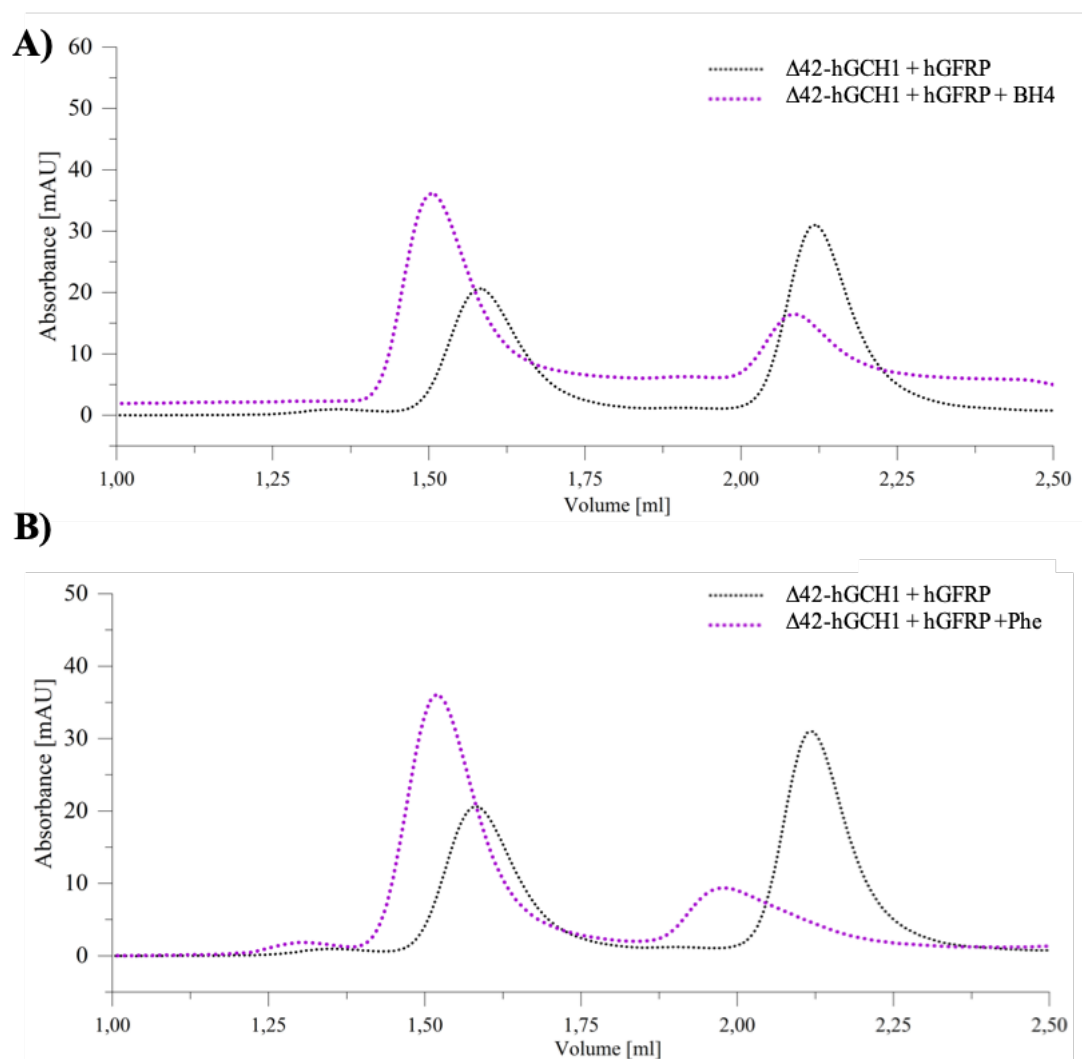


Figure 25: Formation and purification of the hGCH-hGFRP complex using SEC: A) SEC profile of hGCH and hGFRP (1:1.3 molar ratio) in buffer containing 0.1 mM BH4 (purple) and buffer containing no effector molecules (black). hGCH-hGFRP complex formation only occurs in presence of BH4. **B)** SEC profile of hGCH and hGFRP (1:1.3 molar ratio) in buffer containing 20 mM phenylalanine (purple) and buffer containing no effector molecules (black). hGCH-hGFRP complex formation only occurs in presence of phenylalanine.

3.3 Structural studies

In the following analysis of the protein structures, we will focus on the regions A-C, which are shown in Figure 26 and Table 5. These regions show the most pronounced conformational changes. As expected for allosteric enzymes as GCH1,

these regions are predominantly located at the periphery of GCH1 monomers, forming the interface between the individual protomers.

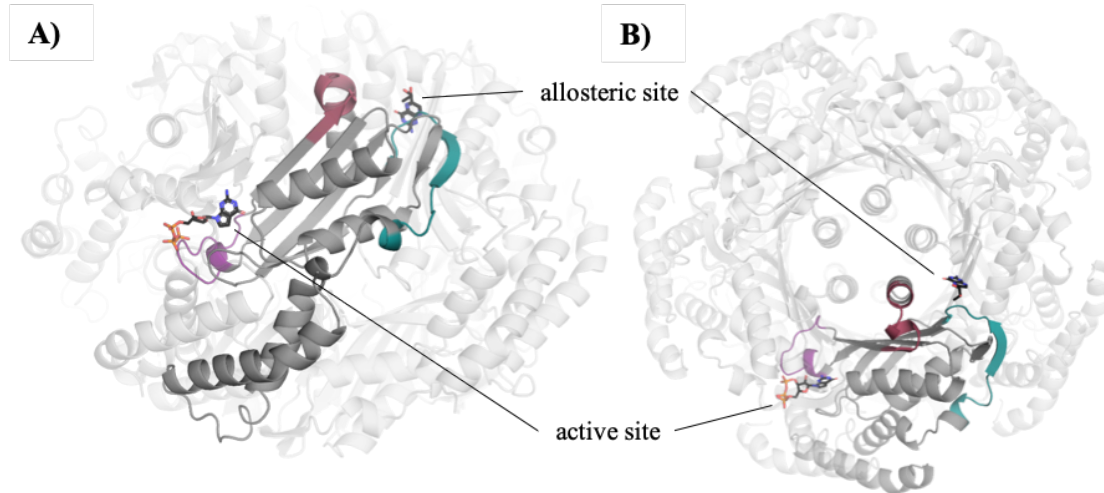


Figure 26: Relevant structural features on GCH1: The homo-decamer of GCH1 is colored in light grey. One GCH1 monomer is highlighted in darker grey. For further analysis relevant regions on GCH1 are colored according to the description in Table 2. The location of the active and the allosteric sites are indicated by the ligands GTP and BH₄, respectively, in stick representation (black). **A)** Side view of GCH1. **B)** Top view of GCH1 depicting the location of the 5-helix bundle and β -barrel in the center of the protein, which are formed from α -helices or β -strands from five protomers.

Table 5: Relevant structural features on GCH1. The colors indicated correspond to the colors in Figure 26.

region	description	residue range
A	Loop connecting the allosteric and active site	115-130
B	Coordination of tri-phosphate	213-222
C	Tip of 5-helix bundle and last strand of β -barrel	230-242

3.3.1 Determination of hGCH-hGFRP complexes by cryo-EM

We suspected from analysis of the published crystal structures of the rGCH1-rGFRP complexes that important functional regions on the protein surface undergo order-disorder transitions on the trajectory from active to inactive or substrate-bound states and could be impacted by crystal packing. Therefore, we decided to use cryo-EM as a complementary approach to resolve the structures of hGCH1-hGFRP

complexes in an aqueous environment, unbiased by crystal contacts.

Table 6: Summary of obtained hGCH1-hGFRP EM structures. The colors indicated correspond to the colors in all following figures.

	name	method	PDB code	cpd	resolution
GCH	EM-hGCH1+hGFRP+Phe+active	 EM	6Z80	Phe + 8-oxo-GTP	3.0 Å
	EM-hGCH1+hGFRP+allosteric	 EM	6Z85	BH4	2.9 Å

Due to their size and symmetry, hGCH1-hGFRP complexes are well suitable for high resolution studies using cryo-EM. Structures of the inhibitory (EM-hGCH1-hGFRP+BH4) and the stimulatory (EM-hGCH1-hGFRP+Phe+active) hGCH1-hGFRP complexes were generated using single particle cryo-EM. Table 6 shows the ensemble of generated EM structures and the names with which we will refer to them in the following.

Grid preparation and data collection For complex formation hGCH1 and hGFRP was mixed with excess of hGFRP and the complex were formed using the optimized buffers described in the previous section. The identification of suitable buffer conditions was key to the preparation of high-quality grids. 100 mM sodium phosphate pH 5.5, 80 mM NaCl and 20 mM phenylalanine was used to form the stimulatory complex and 100 mM sodium citrate pH 5.75 and 0.1 mM BH4 (Sigma Aldrich; T4425) was used for the formation of the inhibitory complex. The two distinct protein complexes were purified using a Superose 6 Increase 10/300 GL column and the respective complex buffers. The respective complex main fractions were pooled and concentrated up to 1-1.6 mg/ml. For grid preparation, the purified samples were not frozen and never kept at 4°C longer than 24 h prior to grid preparation.

Shortly before grid preparation, the complexes were further diluted to reduce the salt and buffer concentration in order to reduce the background and improve the contrast of the cryo-EM samples. The stimulatory complex was diluted with phenylalanine containing buffers to 0.6 mg/ml so that the final buffer composition consisted of 50 mM sodium phosphate pH 5.5, 20 mM NaCl and 20 mM phenylalanine. Furthermore, 0.1 mM 8-oxo-GTP (Jena Bioscience; NU-1116) was added. The Inhibitory complex was diluted to 0.25 mg/ml and 40 mM sodium citrate pH 5.75 and 0.1 mM BH4. 3 μ L of protein solution was applied to freshly glow-discharged

C-flat CF-1.2/1.3-4C Grids and plunge frozen in liquid ethane using a Vitrobot (Thermo Fisher).

Micrographs were automatically recorded using EPU on a Titan Krios microscope (Thermo Fisher) operated at 300 kV equipped with a K2 direct electron detector in electron counting mode at a nominal magnification of 130,000x, corresponding to a calibrated pixel size of 1.077 Å. Dose fractionated 8 s movies of 40 frames were recorded with a total electron dose of 55 e/ Å² using defocus values of 1.0 - 2.4 μm. A total of 2698 micrographs was collected for the inhibitory dataset and 3121 images for the stimulatory complex. Figure 27 A shows an exemplary micrograph of the inhibitory complex. The particles are evenly distributed and the overall background is low. Top and side views of the hGCH-hGFRP complex are clearly visible.

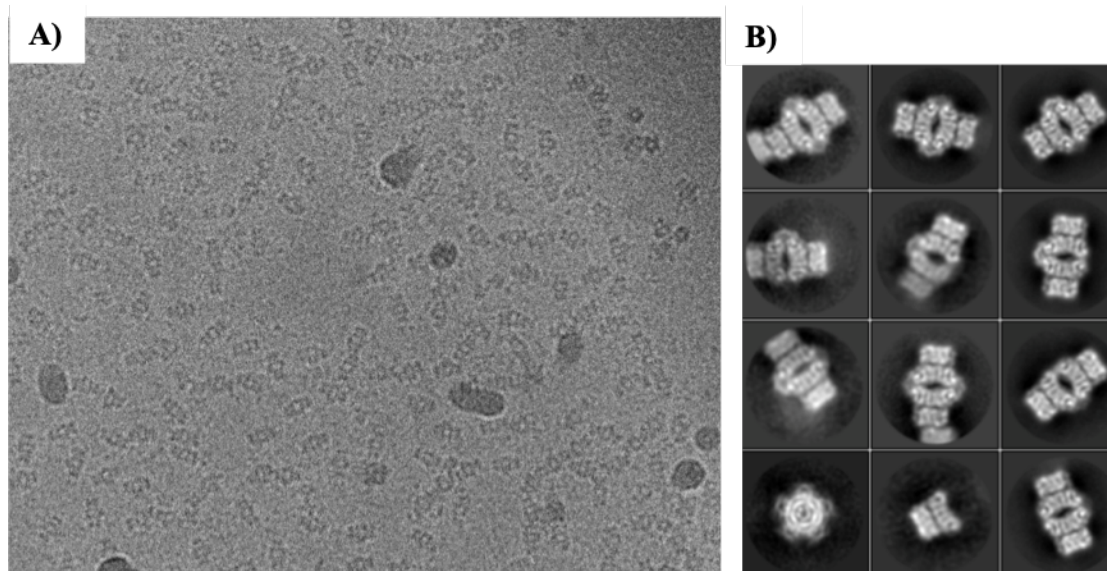


Figure 27: Exemplary micrograph and 2D classes of the inhibitory complex:
A) High magnification micrograph shows single particles of the inhibitory hGCH-hGFRP complex with good distribution. Top and side views of the protein complex are visible.
B) 2D classification of the inhibitory complex shows side and top views but also broken hGCH-hGFRP particles.

Data processing and model building About 3000 micrographs were collected for both, the stimulatory and the inhibitory complex. Approximately 350.000 -

750,000 particles with a box size of 250x250 pixels were extracted. Afterwards the dataset was cleaned by 2D- and 3D-classification. A low-passed filtered volume of the rat GCH1-GRFP crystal structures (1is7; 1wpl) was used as a starting reference for 3D classification. The stimulatory and inhibitory complexes were reconstituted from 122,275 or 254,907 particles, respectively, using RELION 3Dauto-refine and applying D5 symmetry. The refined particles were subjected to per-particle CTF refinement and Bayesian polishing yielding maps of 2.9 and 3.0 Å resolution (Figure 28 BC) determined by the gold-standard 0.143 Fourier shell correlation (FSC) criterion using the post-processing procedure in RELION 3.0. For both complexes the same mask was applied. Local resolution was estimated using MonoRes [120] (Figure 28 A) . Structures of hGCH (1fb1), hGFRP (unpublished) and rGCH-GFRP (1wpl, 1is7) were docked into the final cryo-EM maps and the model was adjusted and refined iteratively. Refinement and Molprobidity statistics were examined and are depicted in Table 7 together with the data collection statistics. The model statistics showed good geometry and matched the cryo-EM reconstruction (Table 7 and Figure 28 DE). The structure of the hGCH-hGFRP inhibitory and stimulatory complexes

Table 7: Data collection and refinement statistics for the inhibitory and stimulatory hGCH1-hGFRP complexes determined by cryo-EM.

Experimental data		
PDB/EMD code	6Z85/11114	6Z80/11113
ID	Inhibitory complex	Stimulatory complex
Protein	hGCH1-hGFRP	hGCH1-hGFRP
Ligands	BH4	Phenylalanine 8-oxo-GTP
Data Collection and Processing		
Microscope	FEI Titan Krios	FEI Titan Krios
Voltage (kV)	300	300
Camera	Gatan K2 Summit	Gatan K2 Summit
Exposure time (s)	8	8
Total Dose ($e^-/\text{\AA}^2$)	55	55
Dose per frame ($e^-/\text{\AA}^2$)	1.38	1.38
Defocus range (μm)	1.0-2.5	1.0-2.5
Pixel size (\AA) (calibrated)	1.077	1.077
Magnification (nominal)	130000x	130000x
Symmetry imposed	D5	D5
Number of micrographs	2688	3121
Initial particle number	1871460	1272592
Final particle number	560802	122310
Map resolution (\AA)	2.9	3.0
FSC threshold	0.143	0.143
Refinement		
Map-sharpening B factor (\AA^2)	-128	-104
Model composition		
Protein (residues)	2360	2660
Ligands	10xBH4	10xPhe; 10x8-oxoGTP
RMSD bond length (\AA)	0.013	0.010
RMSD bond angles ($^\circ$)	1.665	1.587
Sidechain outliers (%)	1	0.4
ADP (B-factor) (min/max/mean)	0.008	0.008
Protein	3.07/25.22/9.14	5.22/30.24/12.07
Ligand	4.54/26.07/5.74	7.16/49.68/9.83
Ramachandran plot		
Favored (%)	96.93	96.05
Allowed (%)	3.07	3.56
Outliers (%)	0.00	0.38
All-atom clashscore	7	3
MolProbity score	2.47	2.53

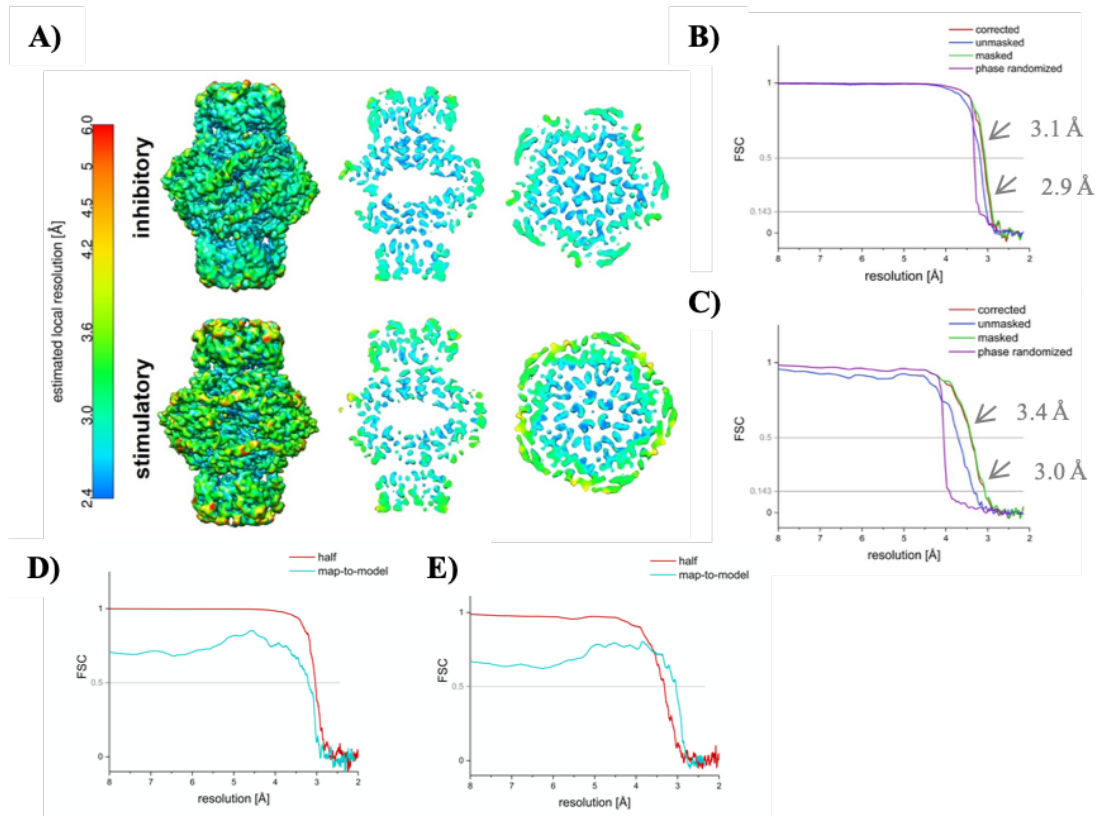


Figure 28: Local resolution estimation and FSC fourier shell correlation of hGCH1-hGFRP complex structures: **A)** Local resolution estimation and FSC functions surface and central slices of the inhibitory (top) and stimulatory (bottom) hGCH1-GFRP complexes colored according to local resolution estimation using MonoRes. FSC of the inhibitory **B)** and the stimulatory **C)** complexes between two half-maps as a function of spatial frequency were calculated. FSC is shown for the original, unmasked half-maps (blue), masked half-maps that had most of the membrane and genome density removed (green), and phase-randomized half-maps (purple) in which phases were randomized at frequencies higher than $1/3.5 \text{ \AA}$ or $1/4 \text{ \AA}$. The phase-randomized FSC drops sharply at the cutoff frequency below the noise threshold (0.143), as expected. The phase-randomization test was used to take the effect of masking on the half-maps into account before calculating the final, corrected FSC curve (red). Good agreement between the masked and corrected curves indicated that masking did not cause overestimation of resolution. The corrected curve drops below the noise threshold at $1/2.9 \text{ \AA}$ and $1/3.0 \text{ \AA}$ indicating a resolution of 2.9 \AA in the reconstruction of the inhibitory complex and 2.9 \AA for the stimulatory complex. FSC between the final cryo-EM map and a map calculated from the fitted model (turquoise) and FSC between maps from independent halves of the data (red) for the inhibitory **D)** and the stimulatory **E)** complex.

Molecular structure of hGCH1-hGFRP determined by cryo-EM The inhibitory and stimulatory protein complexes were reconstructed yielding in maps with resolution of 2.9 and 3.0 Å, respectively, which allowed building of atomic models. The quality and resolution of the EM maps allowed for unambiguous identification of bound ligands (Figure 29B-D). Comparison of the cryo-EM derived inhibitory and stimulatory GCH1-GFRP complexes reveals a significant increase of protein density at the core of the GCH1 decamer involving the central 5-helix bundle and the 20-stranded β -barrel (region C) as a result of allosteric ligands and GFRP binding (Figure 29FG). Looking at region C (Figure 26 & Table 5), this observation fits well with existing models of allosteric enzymes, which control their regulation via an active, mobile state (relaxed state) and an inactive, rigid state (tensed state). Helices approach each other by more than 1Å and the β -barrel diameter is reduced by 2Å. Figure 30AB show top views of both structures and the respective distance measurements. Exactly the same conformational rearrangement is present in the rat complex structures [65], but this finding had been overlooked in the analysis of rat complexes and was not discussed by the authors.

Secondly, the EM structures reveal a drastic difference between the inhibitory and stimulatory hGCH1-hGFRP complex in the structure and flexibility of the surface-lining loop 115-130 (region A) (Figure 26 & Table 5). This loop is the closest and direct connection between the active and the allosteric site. F122 and its close periphery appears well ordered and in a distinct closed conformation in the active site ligand bound state of the stimulatory complex, while it is not visible in the densities after reconstruction of the inhibitory complex (Figure 30CD). For a valid comparison of both EM maps their contour levels were adjusted at regions which are similarly well defined in both structures. In the inhibitory complex, a high degree of flexibility is responsible for the apparent disorder. The loop does not seem to be held in place by any relevant interaction with the surrounding protein structure. In the stimulatory complex, however, the loop is ordered and visible in the maps. F122 seems to act as a clasp, holding the loop in position by π -stacking against H143, localized at the opposite side of the active site cleft (Figure 30C).

The finding of a disorder-order transition in GCH1 is in contrast to the current model discussed in the literature. Based on findings in the rGCH1 complex X-ray structures the authors discuss a major conformational change involving F122

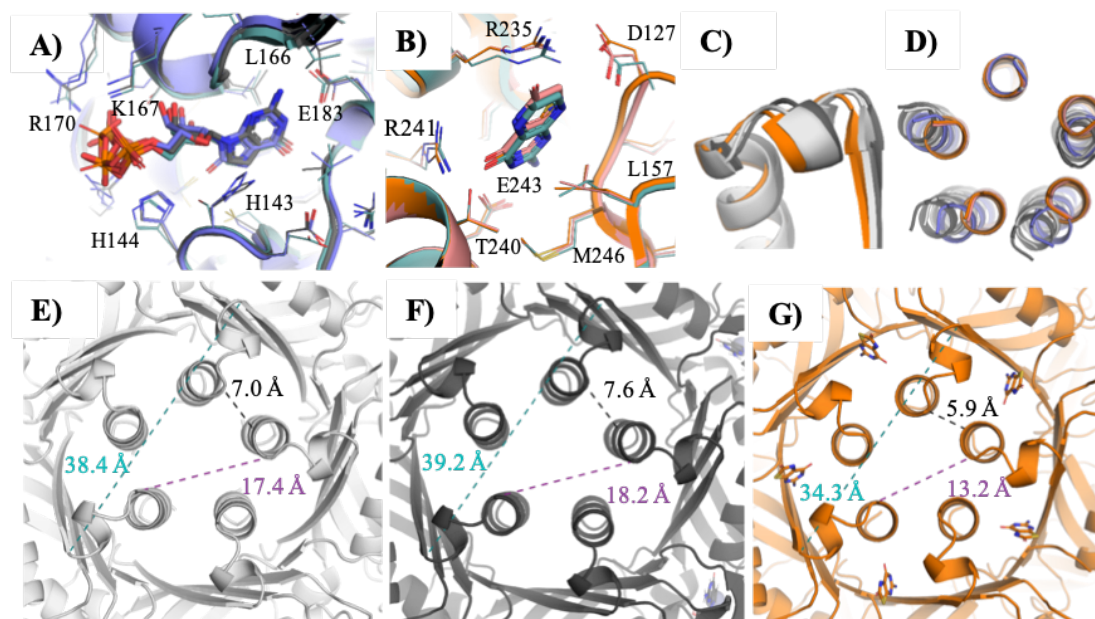


Figure 29: Overview of the architecture of the GCH1-GFRP complex and details of the EM maps of the stimulatory and inhibitory complexes: A) hGCH-hGFRP complex (grey) depicting the binding site for the substrate (purple), the allosteric effector molecules phenylalanine (blue) and BH4 (red) as well as the position of region A (green), which is the loop connecting the active and allosteric site. Observed EM density (black mesh) of the ligands **B)** phenylalanine, **C)** BH4 and **D)** 8-oxo-GTP. **E)** Quality of cryo-EM density map. Selected region showing the fit of the derived atomic model to the cryo-EM density map (black mesh). For panels **F)** and **G)** both EM structures were aligned before images of the cross-sections along the y-axis were taken. The lines in panel A) corresponds to the height of the slices. Panel F) shows a section through GCH1 of the stimulatory complex, while Panel G) shows the equivalent section for the inhibitory complex.

(F113 in the rat GCH1 sequence) and L165 (L156 in rGCH1) [65]. F122 is in an outward orientation in the inhibitory complex leading to a solvent exposed active site, whereas it is inward oriented in the stimulatory complex leading to a closed, solvent shielded active site. In addition, they discuss a displacement of L165 in the inhibitory complex that decreases the depth of the GTP pocket by shifting towards the active site and thereby permitting substrate binding. Close inspection of their experimental data shows, that region A is involved in direct crystal contacts in some protomers of both rat structures. It is obvious that direct crystal packing can influence conformations of surface lining regions. However, crystal packing

artefacts not only have an influence on the conformation of the affected protomer region, but can also change the energy landscape and conformations of neighboring subunits, especially in highly symmetric, cooperative and multimeric proteins with large subunit interfaces. As the EM data was recorded in solute environment, we presume that in the crystal structure region A was artificially locked in a more rigid state and that the loop is in fact disordered in solution. Additionally in our superpositions (Figure 30 C), L165 is not displaced and the active site machinery is in fact fully structurally conserved in both complexes and should allow for substrate binding.

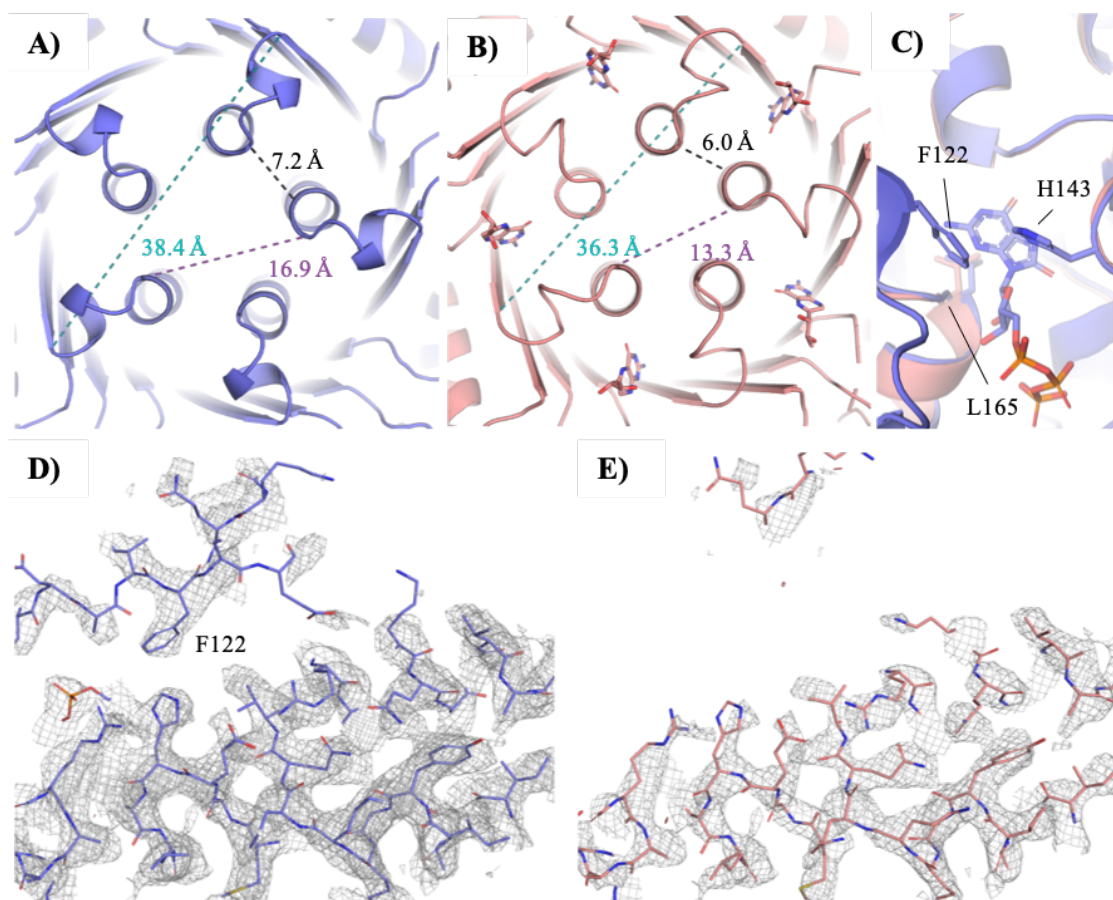


Figure 30: Details of the stimulatory (blue) and inhibitory (red) EM structures: **A)** Distance measurements show the changes of the radius of the β -barrel and the 5-helix bundle between for the stimulatory (blue) complex. Panel **B)** depicts the changes in the dimensions of the radius of the β -barrel and the 5-helix bundle for the inhibitory complex (red). **C)** π -stacking of F122 against His143 of the opposite site of the active site cleft fixes region A in closed conformation in the stimulatory complex (blue). No shifting of L165 backbone and respective helix structure is observed between the inhibitory (red) and stimulatory (blue) complex. EM density of the stimulatory **D)** and inhibitory **E)** complexes show no density for loop F122, while it is defined in the stimulatory complex, indicating a higher degree of flexibility in region A in the inhibitory complex.

3.3.2 hGCH1 crystal structures

In parallel to the cryo-EM studies, we wanted to generate additional information on as of yet unknown conformational states of GCH1 alone, in the absence of GFRP. We chose to utilize a set of active site and allosteric site inhibitors to lock GCH1 in active and inhibited conformations. In order to allow the protein to arrange in

its preferred conformation, all crystals were generated by co-crystallization. We obtained crystal structures of different conformational states and varying levels of occupancy of ligand binding. These structural snapshots helped to delineate the consequences of ligand binding to the GCH1 allosteric site and their influence on the protein conformation (Figure 8).

Table 8: Summary of obtained crystal hGCH1 crystal structures. The colors indicated correspond to the colors in all following figures.

crystal name	method	crystal #	PDB code	cpd	resolution
xtal-GCH1	X-Ray	42815	6Z87	-	2.9 Å
xtal-GCH1+allosteric	X-Ray	41761	6Z88	AXSP0056BS	2.6 Å
xtal-GCH1+allosteric2	X-Ray	41767	6Z89	AXSP0056BS	2.4 Å
xtal-GCH1+active	X-Ray	42508	6Z86	7-deaza-GTP	2.2 Å

A variety of ligands were used to generate the structural information. BH4 and one 2,4-diamino-6-hydroxypyrimidine (=DAHP) analogue were selected as GCH1 allosteric site binders. In the literature, these are described as non-competitive inhibitors [135]. AXSP0056BS (Cpd 1) was identified as a allosteric GCH1 inhibitor in an enzymatic assay with IC₅₀ values of 4 μM. 8-oxo-GTP, a tightly binding, substrate analog GCH1 inhibitor, and 7-deaza-GTP, a non-hydrolysable, more weakly inhibiting analog were used as binders to the active site of GCH1.

Crystallization and structure determination of hGCH1 In order to set up crystallization trials, the proteins were previously buffer exchanged to crystallization buffer (100 mM Citrate pH 5.75, 50 mM NaCl) and concentrated up to 6 mg/mL. For the generation of compound bound structures, GCH at 6 mg/ml was mixed with 1 mM 7-deaza-GTP (100 mM stock ; TriLink N-1044-10) or 1 mM AXSP0056BS (200 mM in DMSO) and incubated at 4 °C for 1h. Screening for crystallization conditions was carried out as previously described in the Method section. Crystal conditions for all GCH1 structures are listed in Table 4.

We determined structures of the human GCH1 in absence (xtal-GCH1) and presence (xtal-GCH1+active) of the substrate analogue 7-deaza-GTP and in presence of the allosteric inhibitor cpd 1 (xtal-GCH1+allosteric and xtal-GCH1+allosteric2). Both co-structures of cpd1 were obtained from the same crystallization trials using the same compound concentration just the crystal condition in which both

crystals were obtained is different (Table 4). xtal-GCH1 is a re-determination of the previously determined apo-hGCH1 structure [4]. Table 8 shows the ensemble of generated hGCH1 structures and the names with which we will refer to them in the following. The data collection and refinement statistics of all crystals are summarized in Table 9.

All dataset were collected on the X06SA (PX I), X06DA (PXIII) or the X10SA X06SA (PX II) beamline (SLS, Villigen, Switzerland). For each structure diffraction data was collected from a single crystal. The diffraction patterns showed sharp well separated spots (diffraction pattern not shown). The diffraction data were processed using the autoPROC toolbox [122]. The data was cut elliptically using STARANISO and the criteria used for the determination of diffraction limits was local $(I/\sigma I) \geq 1.20$. The space groups and unit cell parameters of the four datasets are indicated in Table 9. Molecular replacement using the published hGCH structure (1FB1) was performed using BALBES [62] or Phaser [11]. Crystallographic data statistic and refinement evaluation is given in Table 9. Data statistics show a high completeness and precision of collected reflections. The signal of the spots can be well differentiated from the background even in the highest resolution shell. The models were iteratively fitted into the electron density in Coot [24] and refined using BUSTER [107].

The triclinic 7-deaza-GTP co-crystal contained twenty copies of hGCH1 within the asymmetric unit. Ten protomers accumulate, forming two functional decamers of hGCH1 in the asymmetric unit. In each unit cell, of the orthorhombic cpd1 co-crystal there are ten hGCH1 monomers forming one single functional GCH1 deacmer. The apo and the partially occupied cpd1 co-structure crystallize in the same hexagonal space group but distinct cell parameters. Both unit cells contain five hGCH1 monomers forming a pentamer, wich is translated along the two-fold axis to form the functional decamer.

Table 9: Data collection and refinement statistics for different hGCH1 co- and apo crystals. Values in parentheses represent outer resolution shell.

Experimental data							
PDB code	6Z86	6Z88	6Z89	6Z87			
Crystal ID	42508	41761	41767	42815			
Protein species	hGCH1	hGCH1	hGCH1	hGCH1			
Experiment setup	co-crystal	co-crystal	co-crystal	apo			
Ligand	7-deaza-GTP	cpd1 (AXSP0056BS)	cpd1 (AXSP0056BS) (partial occupied)				
Data collection							
Wavelength (Å)	0.99988	0.99986	0.99987	0.99986			
Space group	P1	C222 ₁	P6 ₅ 22	P6 ₅ 22			
Unit cell parameters							
a, b, c (Å)	87.9 88.6 163.6	112.4 161.5 271.7	121.8 121.8 357.2	109.9 109.9 387.2			
α, β, γ (°)	85.2 88.9 83.5	90.0 90.0 90.0	90.0 90.0 120.0	90.0 90.0 120.0			
Resolution (Å)	87.739–2.206 (2.457–2.206)	135.821–2.687 (2.971–2.687)	105.470–2.366 (2.634–2.366)	95.156–2.561 (2.895–2.561)			
Observed reflections	257298 (13019)	483392 (20327)	1197104 (56604)	511112 (21770)			
Unique reflections	142765 (7139)	47926 (2396)	44678 (2235)	27478 (1375)			
Completeness (spherical) (%)	58.1 (10.5)	69.4 (13.5)	68.9 (12.8)	60.1 (10.0)			
Completeness (ellipsoidal) (%)	89.7 (62.4)	93.9 (58.2)	96.1 (78.8)	93.7 (77.8)			
Redundancy	1.8 (1.8)	10.1 (8.5)	26.8 (25.3)	13.4 (1.8)			
R_{merge} (I)	0.045 (0.337)	0.201 (1.506)	0.109 (2.593)	0.313 (2.985)			
R_{pim} (I)	0.045 (0.337)	0.066 (0.541)	0.021 (0.519)	0.074 (0.758)			
$I/\sigma(I)$	6.2 (1.5)	8.9 (1.5)	24.8 (1.6)	5.2 (1.62)			
$CC_{1/2}$	0.998 (0.772)	0.998 (0.530)	1.000 (0.686)	0.997 (0.670)			
Refinement							
Resolution (Å)	87.7-2.2	135.8-2.6	46.3-2.4	95.2-2.6			
R_{work} (%)	18.1	21.3	22.8	22.8			
R_{free} (%)	20.8	24.9	23.4	25.5			
rmsd bond lengths (Å)	0.009	0.008	0.009	0.007			
rmsd bond angles (°)	1.17	1.08	1.15	0.93			
mean/Wilson B (Å ²)	51/49	74/69	80/75	76/75			
Ramachandran plot							
Favored (%)	98.38	97.77	96.75	97.70			
Outliers (%)	0.00	0.12	0.38	0.22			
Side chain Outliers (%)	3.0	3.9	5.3	1.8			

Molecular details of hGCH1 crystal structures Figure 31 A shows the overlay of bound substrate analogues and Figure 31 B the binding mode of inhibitors binding to the allosteric site. Small molecules recognition does not differ from the observed binding mode in published *E. coli* (1a8r; eGCH1[H112S]+GTP) and rat (1wpl; rGCH1-rGFRP+BH4) crystal structures. Using suitable superpositions of GCH1 monomers and pentameric and decameric ensembles, we analyzed local and global structural changes along the path from unliganded, basally active enzyme to a substrate analog bound, catalytically competent transition state form as well as to partially and fully allosterically inhibited structures [65, 96].

Protein flexibility The observation of region A flexibility described for the cryo-EM data is fully supported by the crystallographic data. The same degree of disorder seen for the inhibitory cryo-EM structure was observed for the xtal-GCH1-allosteric structure, while region A is ordered and F122 is in a defined closed state in xtal-GCH1-active. For the unliganded form xtal-GCH1 weak electron density is visible for region A that allows for tracing the main chain, suggesting that a partially flexible region A is a signature of the basally active state of GCH1. This degree of flexibility in the active site lid could be essential to allow substrate association.

Region B consisting of residues 213-222 is only weakly defined in the electron densities in all structures without an active site ligand bound (xtal-GCH1, EM-GCH1+hGFRP+allosteric and xtal-GCH1+allosteric). It is well defined in the other structures (xtal-GCH1+active and EM-GCH1+hGFRP+Phe+active). R216 is part of this region and in substrate-analog complexed states coordinates the β - and γ -phosphate of GTP variants and contributes to the charge compensation of the triphosphate moiety. Locking the R216 side chain in the presence of triphosphate ligands thus leads to a stabilization of a preferred conformation of this loop.

Effect of substrate binding - stimulatory trajectory Upon formation of the stimulatory complex, which implies association of phenylalanine-bound GFRP to GCH1, only minor conformational rearrangements occur. Attachment of GFRP leads to a slight twisting of the last β -strand of GCH1's β -barrel and the central α -helix in anticlockwise direction.

The most obvious conformational change upon substrate binding occurs in region A. The partial disorder of the residue range 115-130 is resolved into a well defined loop structure closing the upper ceiling of the active site pocket. This disorder-order transition is clearly seen both in the cryo-EM maps and in the X-ray structures. Further, region B involving the triphosphate binding pharmacophore becomes ordered as discussed above. Finally, upon binding of 7-deaza-GTP changes in region C including positioning of the 5-helix bundle and curvature of the β -barrel are observed. Here, region C bends outwards, towards the active site and the protein inside expands in comparison to the apo structure (Figure 31 EF). This movement is opposite to the observed conformational change in the inhibitory complex.

Effect of allosteric inhibitor binding - inhibitory trajectory From one co-crystallization campaign, surprisingly we obtained two independent structures of allosterically inhibited GCH1: One fully inhibited form (xtal-GCH1-allosteric) with all allosteric sites occupied by inhibitor, and a partially inhibited form (xtal-GCH1-allosteric2), in which only two of five allosteric pockets in each GCH1 pentamer were occupied with cpd 1. We do not see any major differences between the cryo-EM structure of the BH4-GFRP inhibited GCH1 and the X-ray structure of cpd 1inhibited GCH1. In particular, the quaternary structural changes in region C are replicated in the X-ray structure, namely the shift of the central α -helices. The shrinking of the β -barrel radius is even more pronounced and the radius of the β -barrel decreases by 5Å, when compared to apo GCH1 (Figure 31 EG). Thus, the major trigger for the large change in quaternary structure and compaction of the GCH1 interior is binding of ligands into the allosteric pocket.

The partially occupied structure xtal-GCH1+allosteric2 allows to delineate the atomic details of the structural transition. Strikingly, the GCH1 structure in the xtal-GCH1+allosteric2 crystal does not adopt the five-fold symmetry as usual, but is shifted to an asymmetric state (Figure 32A). Cpd 1 binds to two allosteric sites, which are located in the interface of chain A and B and of chain D and E. The three remaining allosteric sites remain unoccupied. Binding of inhibitors into the allosteric site, which is spanned by two distinct protomers, trigger different processes in the respective subunits. Interactions of residues of one subunit (chains A or D, right) trigger conformational rearrangements of the respective subunit,

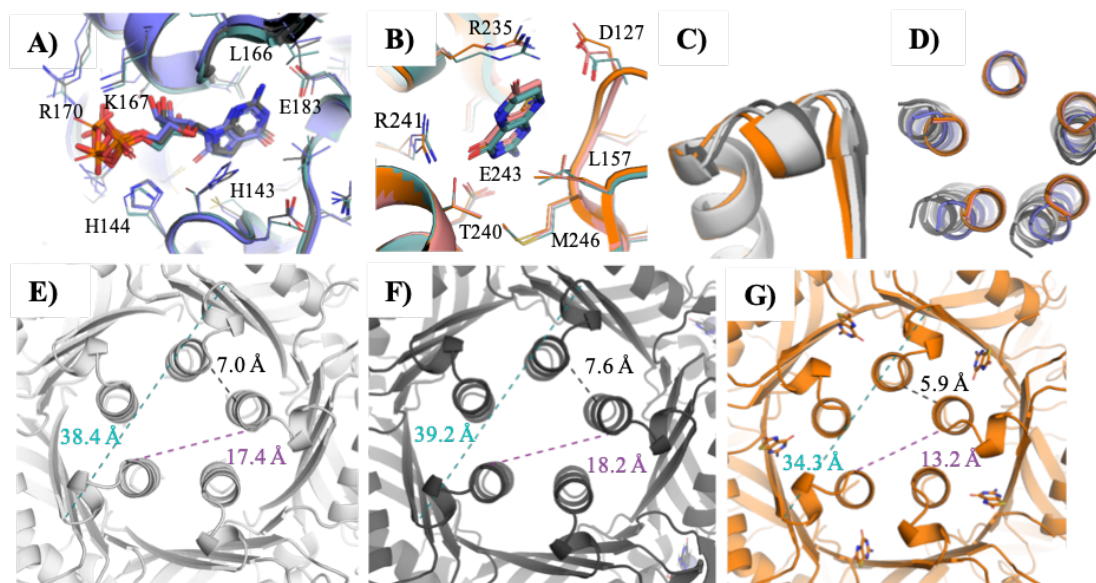


Figure 31: Overall conformational changes upon binding of compounds: **A)** Comparison of substrate analogue binding mode in EM-hGCH1+hGFRP+Phe+active (blue), the xtal-GCH1+ active (dark grey) and the published substrate-bound *E. coli* structure (1A8R) (turquoise). **B)** Inhibitor recognition in the allosteric pocket of the EM-hGCH1+hGFRP+allosteric (red) structure, the xtal-GCH1+allosteric (orange) structure and the published structure of the inhibitory rat complex (1WPL) (turquoise). **C)** Movements of region A towards the interior of the protein upon binding of allosteric inhibitors and opposing motion upon binding of substrate analogues. Comparison between the xtal-GCH1 (light grey), xtal-GCH1+active (dark grey) and xtal-GCH1+allosteric (orange) structures. **D)** 5-helix bundle overlay of all human GCH1 and GCH1-GFRP structures, showing a perfect overlay of the EM-hGCH1+hGFRP+allosteric (red) and the xtal-GCH1+allosteric (orange) structures, as well as the xtal-GCH1 (light grey) and xtal-GCH1+active (dark grey) structures. The structures cluster into three distinct conformations: active (light grey, dark grey) stimulated (blue) and inhibited (red, orange). The coloring of the structures is according to the colors listed in Table 1. Distance measurements show the changes of the radius of the β -barrel and the 5-helix bundle between **E)** xtal-GCH1 (light grey), **F)** xtal-GCH1+active (dark grey) and **G)** xtal-GCH1+allosteric (orange) structures.

while the conformation of the other subunit (chains B and E, left) does not change (Figure 32AE).

Figure 32A shows the top view on the allosteric site. Binding of cpd 1 induces concomitant approximation of the C-terminal helices and β -strands of subunits A and B (D and E, respectively) while distances between helices B-D, C-D and A-E remain unchanged relative to the active state of the enzyme. Analysis of

the conformational states of all protomers show that chain A and D exhibit an inhibitory xtal-GCH1+allosteric-like state, while protomers B, C and E are in an apo-like conformation in terms of helix-bundle and β -barrel positioning and curvature (Figure 32E). Region A is ordered in protomers A, C and D, but is highly flexible in chains B and E. This observation agrees with the also drastically increased flexibility of region A in the remaining allosteric ligand bound EM and X-ray structures.

Binding of an allosteric inhibitor to the allosteric pocket triggers a cascade of conformational changes of proximal residues. E243 (chain B) is the recognition motif for the amino-pyrimidone substructure of inhibitors to this site. It does not need to move much in order to coordinate the 2-aminopyrimidine moiety of BH4 and analogues. In contrast, R241 (chain A) moves back and counter clockwise by 1.5Å (alignment of xtal-GCH1+allosteric2 and xtal-GCH1+active on chains A+B) to form a hydrogen bond to the carbonyl group of BH4 or cpd 1. At the same time, the neighboring R235 (chain A) also moves towards the protein interior, facilitating cation- π -stacking of its guanidine group and the biopterin heterocycle (Figure 32B). Here the backbone shifts by 2Å. Due to these rearrangements and changes in the hydrogen network, the entire backbone of the residues 230-240 of region A shifts by 0.8-2.4Å. From our analysis it remains unknown whether R241 or R235 is the main trigger for conformational rearrangement or if a joint movement of both residues is necessary.

Change of position of R235 as well as the steric requirements of the ligand BH4 in the pocket leads to further local structural changes. E128 is pushed out of its position in the active state in which it forms a hydrogen bond to the backbone NH of M230 of the C-terminal β -strand of the neighboring subunit. Removed from its old position, it allows closure of the top part of the β -barrel, which triggers the compaction of the barrel by formation of a tight hydrogen network between both neighboring strands as discussed above (Figure 32DG). D127 is recruited by R235 to form a charge reinforced hydrogen bond of their side chains. This movement completes the closure and formation of the final shape of the allosteric pocket.

These two rearrangements involving D127 and E128 trigger further changes in the structure of the residues 120-126 that lie on the path toward the active site. In particular, H126 is displaced to a new position pointing toward E183, the guanine

recognition residue in the active site (Figure 32F). The exchange of positions of the H126 and E128 side chains in the inhibitory state leads to a loosening of the 115-125 loop structure by two amino acids. This may be the structural basis for increased loop flexibility observed in the inhibited protomers in the xtal-GCH1+allosteric (chains A, B, C, D, E) and xtal-GCH1+allosteric2 structures (chains B and E).

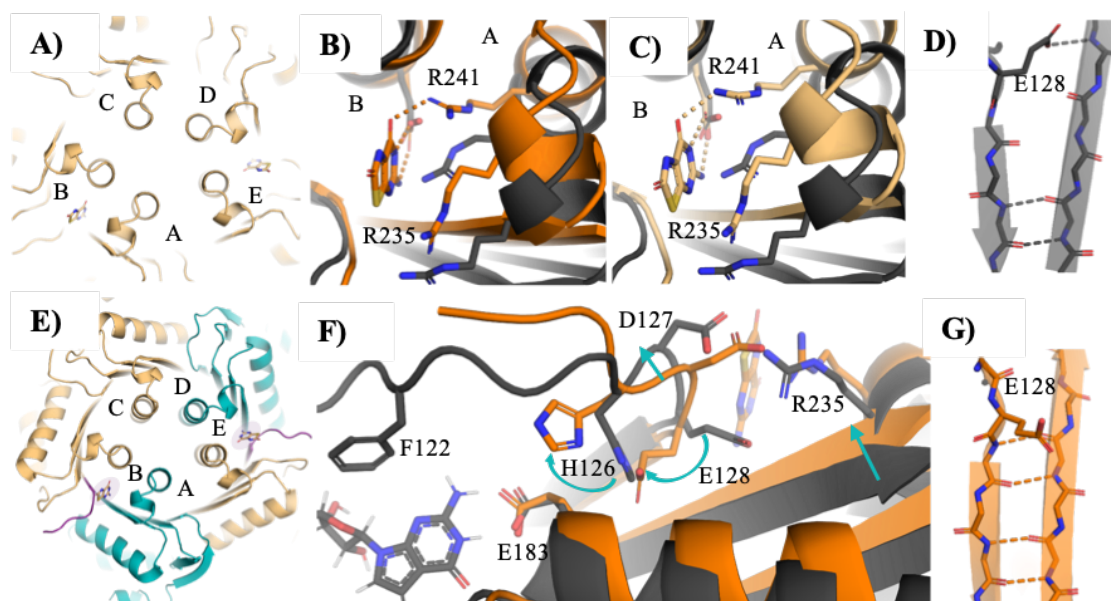


Figure 32: Details of conformational rearrangement upon binding of AXSP0056BS to GCH1: **A)** Cartoon representation of the view of xtal-GCH1+allosteric2 shows the asymmetric rearrangement of the 5-helix bundles. Panel **B+C)** shows a top view on the allosteric site of **B)** xtal-GCH1+allosteric2 (light orange) (chain A+B) and **C)** xtal-GCH1+allosteric (orange) in comparison to the active structure xtal-GCH1+active (dark grey) (alignment on chain B). **E)** Cartoon representation of the top view of xtal-GCH1+allosteric2. The regions that are in active conformations are colored in light orange, while the teal protomers show the quaternary characteristics of the inhibited conformation. The purple colored loops (protomer B and E) indicate the loop regions, in which we observed a high degree of disorder and are therefore thought to be flexible. **F)** Rearrangements in loop 115-130 upon binding of an allosteric inhibitor in xtal-GCH1+allosteric. **D+G)** Interface between two protomers forming the β -barrel.

3.3.3 X-ray structures of hGCH1-hGFRP ligand bound complexes

In parallel to studying the hGCH1-hGFRP complex using cryo-EM we also conducted crystallization trials with the hGCH1-hGFRP complexes. We were very

interested in the question on whether a substrate analogue was still able to bind into the active site and if the binding mode in the inhibitory complex differed from that in the stimulatory complex. Therefore, both, the stimulatory and the inhibitory complex, was crystallized in presence of 7-deaza-GTP. Table 10 shows the ensemble of generated hGCH1 structures and the names with which we will refer to them in the following.

Table 10: Summary of obtained hGCH1-hGFRP ligand bound complex crystal structures. The colors indicated correspond to the colors in all following figures.

	crystal name	method	crystal #	PDB code	cpd	resolution
complex	xtal-GCH1+GFRP+Phe+active	 X-Ray	43868	7ALB	Phe + 7-deaza-GTP	2.0 Å
	xtal-GCH1+GFRP+allosteric+active	 X-Ray	1053707	7ALQ	BH4 + 7-deaza-GTP	2.2 Å

Crystallization and structure determination of hGCH1-hGFRP complexes In order to set up crystallization trials, the protein complexes were formed in presence of the effector molecules BH4 and Phenylalanine using the optimized buffers as described previously. The purified hGCH1-hGFRP complexes were concentrated up to 6 mg/mL. For the generation of the substrate analogue bound structures, the protein was mixed with 1 mM 7-deaza-GTP (100 mM stock ; TriLink N-1044-10) and incubated at 4 °C for 1h. Screening for crystallization conditions was carried out as previously described in the Method section. Crystal conditions for all complex structures determined by X-ray crystallography are listed in Table 4.

We determined structures of the human stimulatory (xtal-GCH1+GFRP+Phe+active) and inhibitory (xtal-GCH1+GFRP+allosteric+active)GCH1-GFRP complex, in presence of the substrate analogue 7-deaza-GTP, which is supposed to bin the active site of hGCH1. Table 10 shows the ensemble of generated hGCH1 structures and the names with which we will refer to them in the following. The data collection and refinement statistics of all crystals are summarized in Table 11.

The two datasets were collected on the X06SA (PX I), X06DA (PXIII) or the X10SA X06SA (PX II) beamline (SLS, Villigen, Switzerland). For each structure diffraction data was collected from a single crystal. The diffraction patterns showed sharp well separated spots (diffraction pattern not shown). The diffraction data were processed using the autoPROC toolbox [122]. The data was cut elliptically

using STARANISO and the criteria used for the determination of diffraction limits was local $(I/\sigma I) \geq 1.20$. The space groups and unit cell parameters of the four datasets are indicated in Table 11. Molecular replacement using the published rat complex structures (1IS8,1WPL) was performed using BALBES [62] or Phaser [11]. Crystallographic data statistic and refinement evaluation is given in Table 11. Data statistics show a high completeness and precision of collected reflections. The signal of the spots can be well differentiated from the background even in the highest resolution shell. The models were iteratively fitted into the electron density in Coot [24] and refined using BUSTER [107].

Both hGCH1-hGFRP complexes crystallized in the same monoclinic space group but with distinct cell parameters. The asymmetric unit of both 7-deaza-GTP co-crystals contained twenty copies of hGCH1 and twenty protomers of hGFRP. Ten hGCH1 and ten hGFRP molecules accumulate, forming two functional decamers of hGCH1 of which each GCH1 decamer is sandwiched by two hGFRP pentamers.

Table 11: Data collection and refinement statistics for GCH1-hGFRP ligand bound complex crystals Values in parentheses represent outer resolution shell.

Experimental data		
PDB code	7ALB	7ALQ
Crystal ID	43868	1053707
Protein species	hGCH1-hGFRP	hGCH1-hGFRP
Experiment setup	co-crystal	co-crystal
Ligand	Phe + 7-deaza-GTP	BH4 + 7-deaza-GTP
Data collection		
Wavelength (Å)	1.00000	0.99988
Space group	P12 ₁ 1	P12 ₁ 1
Unit cell parameters		
a, b, c (Å)	160.7 116.1 177.3	106.1 185.4 184.2
α , β , γ (°)	90 94.9 90	90 97.9 90
Resolution (Å)	160.059-1.985 (2.139-1.985)	182.466-2.207 (2.464-2.207)
Observed reflections	2125175 (346319)	780103 (39461)
Unique reflections	399464 (66277)	223942 (11196)
Completeness (spherical) (%)	89.4 (74.4)	63.5 (11.3)
Completeness (ellipsoidal) (%)	93.4 (68.9)	93.9 (69.0)
Redundancy	5.3 (5.2)	3.5 (3.5)
R_{merge} (I)	0.167 (1.805)	0.113 (0.902)
R_{pim} (I)	0.079 (0.854)	0.071 (0.565)
$I/\sigma(I)$	6.8 (0.9)	9.3 (1.6)
$CC_{1/2}$	0.996 (0.412)	0.996 (0.466)
Refinement		
Resolution (Å)	160.2-2.0	182.5-2.2
R_{work} (%)	20.6	18.1
R_{free} (%)	22.4	21.2
rmsd bond lengths (Å)	0.008	0.008
rmsd bond angles (°)	0.98	1.09
mean/Wilson B (Å ²)	33/29	45/43
Ramachandran plot		
Favored (%)	98.40	97.70
Outliers (%)	0.04	0.48
Side chain Outliers (%)	1.75	4.08

Molecular details of hGCH1-hGFRP complexes crystal structures We were able to determine the substrate analogue bound structure of the inhibitory and of the stimulatory human GCH-GFRP complexes at high resolution. The newly obtained structures show no differences in the quaternary structure compared to the already published EM structures. Consistent with these structures, a large domain movement can be observed, which includes the approaching of the 5-helix bundle and a reduction of the diameter of the β -barrel.

For the first time, the binding of 7-deaza-GTP, a medium affinity substrate analogue inhibitor of GCH1, to the inactive inhibitory complex is shown. Figure 33 AB compares the binding mode of the substrates in the active and inhibited enzyme complex. Surprisingly, the binding mode and interaction details of the substrate analogue in both complexes are very similar. This finding devalidates previous hypotheses that reduced substrate affinity or steric inhibition of the substrate binding is the reason for the reduced activity of the inhibitory complex.

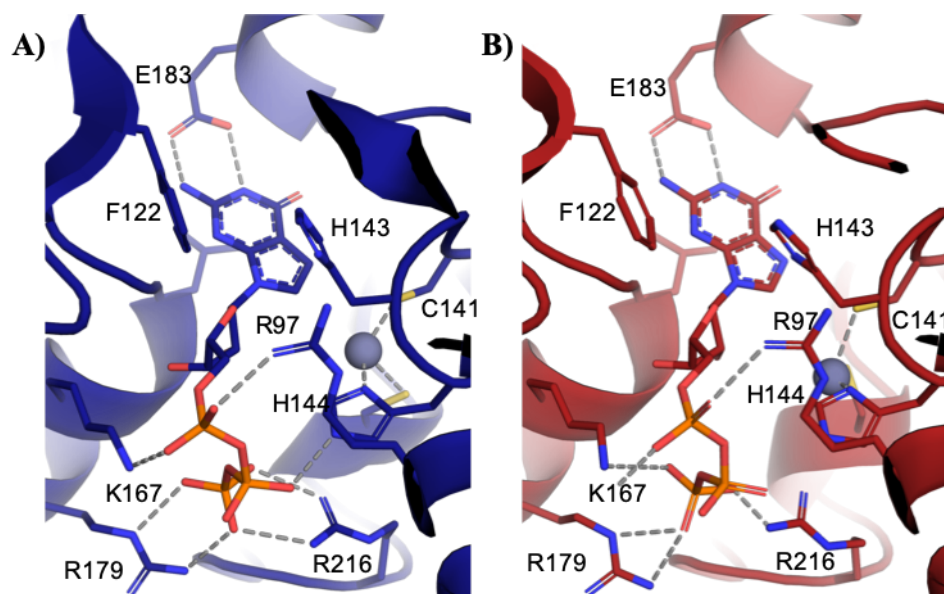


Figure 33: Substrate binding in the active and inactive GCH1-GFRP complex: A) Stick and cartoon representation of the 7-deaza binding in the stimulatory complex (blue). **B)** Stick and cartoon representation of the 7-deaza binding in the inhibitory complex (red).

3.3.4 X-ray structures of hGFRP

Furthermore, the first structure of human GFRP in absence and presence of its effector molecule phenylalanine is presented within this work. The following analysis of the crystal structures allows us to draw origin effect relationships to determine the role of effector molecules on the conformation of GFRP also in comparison GFRP which is in complex with GCH1. Table 12 shows an overview of the structures presented here.

Table 12: Summary of obtained hGFRP crystal structures. The colors indicated correspond to the colors in all following figures.

	crystal name	method	crystal #	PDB code	cpd	resolution
GFRP	xtal-hGFRP	X-Ray	6655	7ACC	-	2.0 Å
	xtal-hGFRP+Phe	X-Ray	41726	7AL9	Phe	1.7 Å

Crystallization and structure determination of hGFRP In order to set up crystallization trials, hGFRP in SEC buffer (20 mM Tris pH 7.4, 150 mM NaCl) was concentrated up to 10 mg/mL. For the generation of compound bound structures, hGFRP at 10 mg/ml was mixed with 20 mM Phenylalanine (200 mM stock, in PBS) and incubated at 4 °C for 1h. Screening for crystallization conditions was carried out as previously described in the Method section. Crystal conditions for all GFRP structures are listed in Table 4.

We determined structures of the human GFRP in absence (xtal-hGFRP) and presence (xtal-hGFRP+Phe) of the effector molecule Phenylalanine. Table 12 shows the ensemble of generated hGFRP structures and the names with which we will refer to them in the following. The data collection and refinement statistics of all crystals are summarized in Table 13.

Both hGFRP datasets were collected on the X06SA (PX I), X06DA (PXIII) or the X10SA X06SA (PX II) beamline (SLS, Villigen, Switzerland). For each structure diffraction data was collected from a single crystal. The diffraction patterns showed sharp well separated spots (diffraction pattern not shown). The diffraction data were processed using the autoPROC toolbox [122]. The data was cut elliptically using STARANISO and the criteria used for the determination of diffraction limits was local $(I/\sigma I) \geq 1.20$. The space groups and unit cell

parameters of the four datasets are indicated in Table 13. Molecular replacement using the published rGFRP structure (1JG5) was performed using BALBES [62] or Phaser [11]. Crystallographic data statistic and refinement evaluation is given in Table 13. Data statistics show a high completeness and precision of collected reflections. The signal of the spots can be well differentiated from the background even in the highest resolution shell. The models were iteratively fitted into the electron density in Coot [24] and refined using BUSTER [107].

The tetragonal hGFRP apo crystal contained ten copies of hGCH1 within the asymmetric unit. five protomers accumulate, forming two functional pentamers of hGFRP in the asymmetric unit. In each unit cell, of the monoclinic Phenylalanine co-crystal there are five hGFRP monomers forming two functional GCH1 pentamers. In both structures the pentamers are facing each other with their bottom side, which is pointing towards GCH1 in GCH1-GFRP complexes.

Table 13: Data collection and refinement statistics for hGFRP co- and apo crystals Values in parentheses represent outer resolution shell.

Experimental data		
PDB code	7ACC	7AL9
Crystal ID	6655	41726
Protein species	hGFRP	hGFRP
Experiment setup	apo	co-crystal
Ligand	-	Phenylalanine
Data collection		
Wavelength (Å)	0.99988	0.99986
Space group	P4 ₃ 2 ₁ 2	P12 ₁ 1
Unit cell parameters		
a, b, c (Å)	107.3 107.3 143.0	66.9 98.1 67.5
α , β , γ (°)	90.0 90.0 90.0	90.0 102.5 90.0
Resolution (Å)	142.98-2.04 (2.15-2.04)	54.7-1.8 (1.980-1.781)
Observed reflections		227243 (56173)
Unique reflections	53495	56173 (16863)
Completeness (spherical) (%)	100.0 (100.0)	82.7 (76.3)
Completeness (ellipsoidal) (%)		84.6 (63.9)
Redundancy	13.2	3.4 (3.3)
R_{merge} (I)	8.3 (50.4)	0.083 (1.920)
R_{pim} (I)	8.6 (14.2)	0.099 (2.285)
$I/\sigma(I)$	25.2 (5.6)	9.1 (0.6)
$CC_{1/2}$		0.999 (0.344)
Refinement		
Resolution (Å)	85.8-2.0	54.7-1.7
R_{work} (%)	16.7	20.3
R_{free} (%)	19.1	23.5
rmsd bond lengths (Å)	0.008	0.008
rmsd bond angles (°)	0.92	0.90
mean/Wilson B (Å ²)	33/28	32/26
Ramachandran plot		
Favored (%)	99.03	97.65
Outliers (%)	0.00	0.00
Side chain Outliers (%)	0.9	2.4

Molecular details of hGFRP crystal structures In addition to the already published structure of rat GFRP, we were able to solve the first human GFRP structures in the presence and absence of phenylalanine. Isolated hGFRP assembles in a pentameric ring of five subunits the quaternary structure of which is highly similar to the rGRPR and the recently published hGCH1-hGFRP complex structures. Likewise, the rmsd of C atoms between the free and the Phenylalanine bound hGFRP structures is small 0.12 Å comparing monomers and 0.23 Å for pentamers. However, local structural differences near the phenylalanine binding site, within residues 9-11 and 74-76, were observed (Figure 34). Ile10 is flipped towards the hydrophobic cavity, in the unbound structure, while it is displaced by the phenyl ring of phenylalanine in the phenylalanine co-structure. The displacement of Ile10 upon binding of phenylalanine leads to a change in the conformation of loop 9-11 and the induction of a cis-peptide. Upon movement of Ile10, Gln75 is able to form hydrogen bonds to the amino and carboxyl groups of phenylalanine, which is further coordinated by backbone interactions of Ile10 and Gln75 and Thr76 of the neighboring chain (Figure 34 B).

We observed binding of an ion, which was previously described as a potassium ion, in both hGFRP structures [65, 133]. The potassium coordination by Thr7 and the peptide backbone of Ile10, Arg11 and Val13 does not differ in both structures. Similarly, in inhibitory and stimulatory hGCH1-hGFRP complexes loop 7-13 of hGFRP coordinates a potassium ion in the same manner. This leads to the conclusion that potassium binding is neither influenced by complexation with GCH1 nor by the binding of effector molecules. Comparison of the structures of GFRP alone with GFRP the complex with GCH1 shows that GFRP in the stimulatory complex is almost identical to the phenylalanine bound GFRP structure, while non-ligand bound GFRP is very similar to GFRP in the inhibitory complex. This together with the fact that the GCH1-GFRP interface is formed by only a few direct contacts suggests that the introduction of the cis-peptide and loop 9-1 conformation is induced solely by the binding of phenylalanine. GCH1 seems to have little or no influence on GFRP conformation. In general, GFRP appears to be a very stable protein, showing only minor changes in loop 37-45 upon binding of GCH1. This is in line with the discussed role of GFRP as scaffolding protein [66, 133].

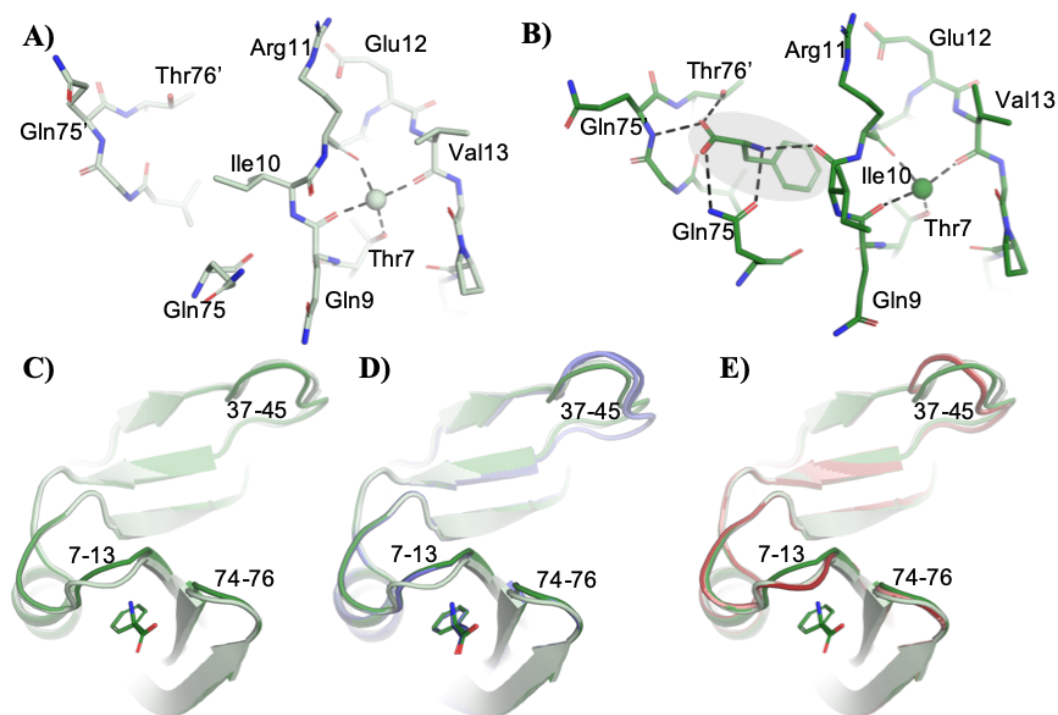


Figure 34: Conformational rearrangements in free and complexed GFRP: **A)** Stick representation of the phenylalanine binding site in the GFRP crystal structure (light green). Ile10 is blocking the binding site. **B)** The GFRP-Phe crystal structure (green) shows the coordination of phenylalanine in its binding pocket. Superimposition of **C)** GFRP (light green) and GFRP-Phe, **D)** GFRP (light green), GFRP-Phe and GFRP of stimulatory complex (blue) and **E)** GFRP (light green), GFRP-Phe and GFRP of inhibitory complex (red).

3.4 GCH mutagenesis study

In order to test the role of the key residues H126, D127, E128, R235 and R241 involved in allosteric inhibitor binding and conformational change, various point mutants were prepared and tested for their ability to be stimulated and inhibited by effector molecules in the presence or absence of GFRP. Mutants were quality controlled by SDS-PAGE, size exclusion chromatography (SEC) and by using Differential Scanning Fluorimetry (DSF), which demonstrated that the mutated proteins are natively folded and show merely a slightly reduced melting point compared to the wild-type protein (Table 14). Enzyme activity was evaluated using an activity assay measuring the formation of the product H₂NTP at 330 nm with increasing GTP concentrations.

With one exception (see below) all discussed GCH1 mutants are still functionally active, but show slightly reduced basal activity compared to wild type protein (Figure 36). R241A-GCH1 and R235A-GCH1 lost the sensitivity to BH4 in absence and presence of GFRP and cannot be inhibited (Figure 36). This indicates that these residues are essential for binding of BH4 and the adoption of the inhibitory complex, and that the conformational change is essential for the formation of the inhibitory complex. R235A-GCH1 cannot be stimulated by GFRP-Phe (Figure 36), consistent with the fact that in the stimulatory complex the side chain of R235 is involved in a hydrogen bonding interaction with the carbonyl oxygen of L40 of GFRP, which apparently is essential for complex formation.

Finally, the F122A mutant was generated and characterized to check whether the structurally observed, F122 dependent closure of the active site plays a key role in GCH1 function. The F122A mutant is able to form GFRP complexes with BH4 and phenylalanine, elutes as one sharp peak from SEC corresponding to a 350kDa complex and shows a sharp melting transition in DSF measurement (Figure 35 AB). Further, we see an increased thermal stability upon binding of GTP, comparable to wild-type protein (Table 14). This indicates that the protein is properly folded and able to bind substrate and GFRP. Therefore, it was surprising that F122A is completely inactive in enzymatic assays, indicating the importance of F122 in the regulatory mechanism (Figure 36 AB).

Table 14: Differential scanning fluorimetry (DSF) measurement TM values of GCH1 and mutated GCH1 variants. The protein melting points were determined in presence and absence of GTP.

protein	TM [°C]	Δ TM WT [°C]	TM + GTP [°C]	Δ TM WT [°C]
WT	76.5	-	83.2	7.0
F122A	71.0	-5.5	75.2	4.2
R235A	70.7	-5.8	81.2	11.2
D127A	73.5	-3.0	78.0	5.0
E128A	76.0	-0.5	78.5	4.3
H126A	74.2	-2.3	80.0	6.0
R241A	69.3	-7.2	86.2	17.7

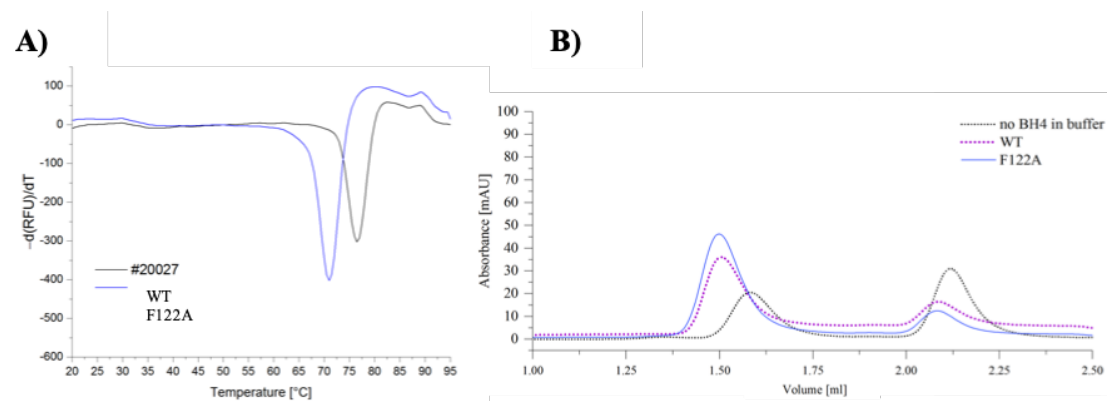


Figure 35: Characterization of F122A mutant using DSF and analytical SEC: **A)** Determination of protein melting points using DSF. T_M of wtGCH1 is 76.5 °C and a T_M of 71.0 °C was measured for F122A-GCH1. **B)** Analytical size exclusion protein shows that both proteins (wtGCH1 (purple) F122A-GCH1 (blue)) are able to form hGFRP complexes in presence of BH4. The black curve shows the mixture of hGFRP and wtGCH1 in absence of BH4 in all buffers.

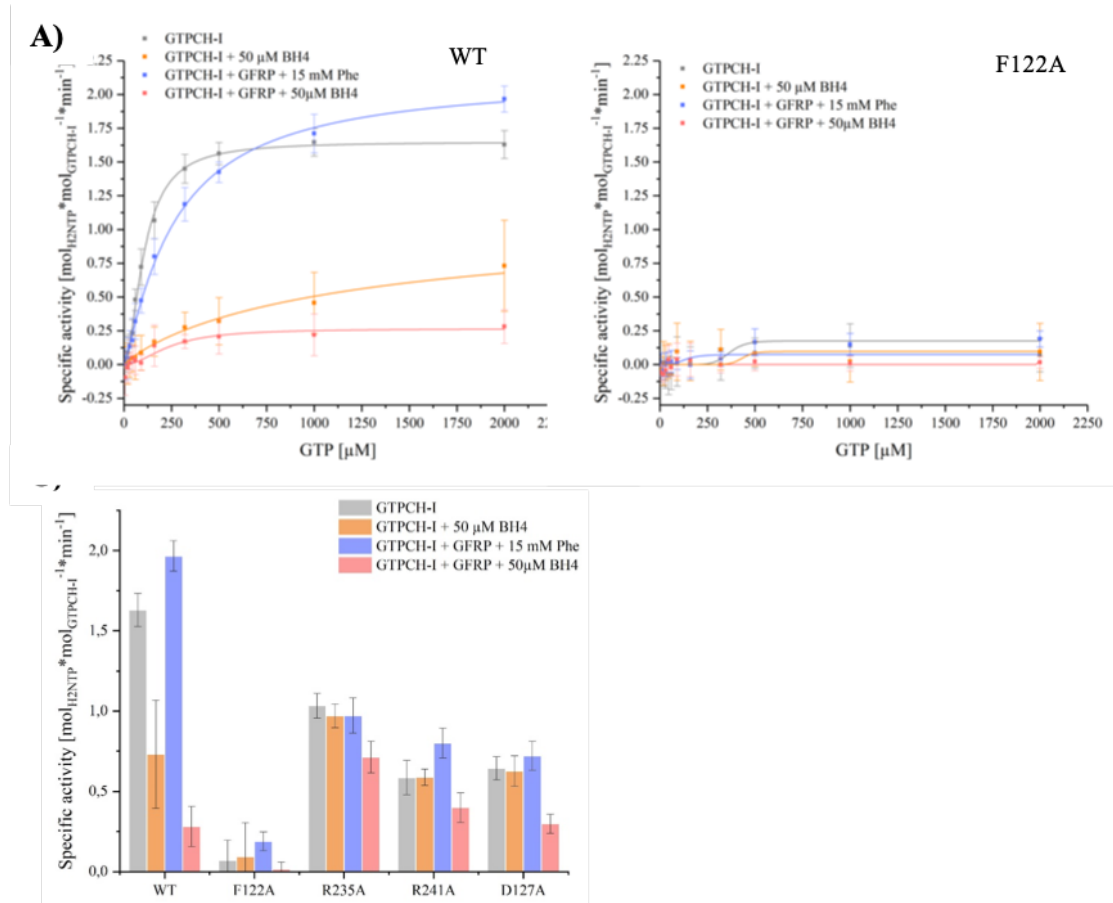


Figure 36: Substrate binding in the active and inactive GCH1-GFRP complex: Specific enzyme activity of **A)** wild-type GCH1 and **B)** F122 using various protein and effector molecule combinations and a substrate concentration from 1-2000 μM GTP. Specific activity GCH1 plotted versus substrate concentration. Fitted by using the Hill equation ($n = 3$) (line-plot). **F)** Bar-plot of the specific enzyme activity at 2000 μM GTP compares the basal activity of the enzymes (grey), the ability to be stimulated (blue) and the ability to be allosterically inhibited in presence (red) and absence (orange) of GRFP. **C)** Bar-plot of the specific enzyme activity at 2000 μM GTP compares the basal activity of the enzymes (grey), the ability to be stimulated (blue) and the ability to be allosterically inhibited in presence (red) and absence (orange) of hGRFP. Graph compares GCH1, F122A-GCH1, R235A-GCH1 and R241A-GCH1 ($n = 3$).

3.5 Determination of binding affinities and kinetics using NMR.

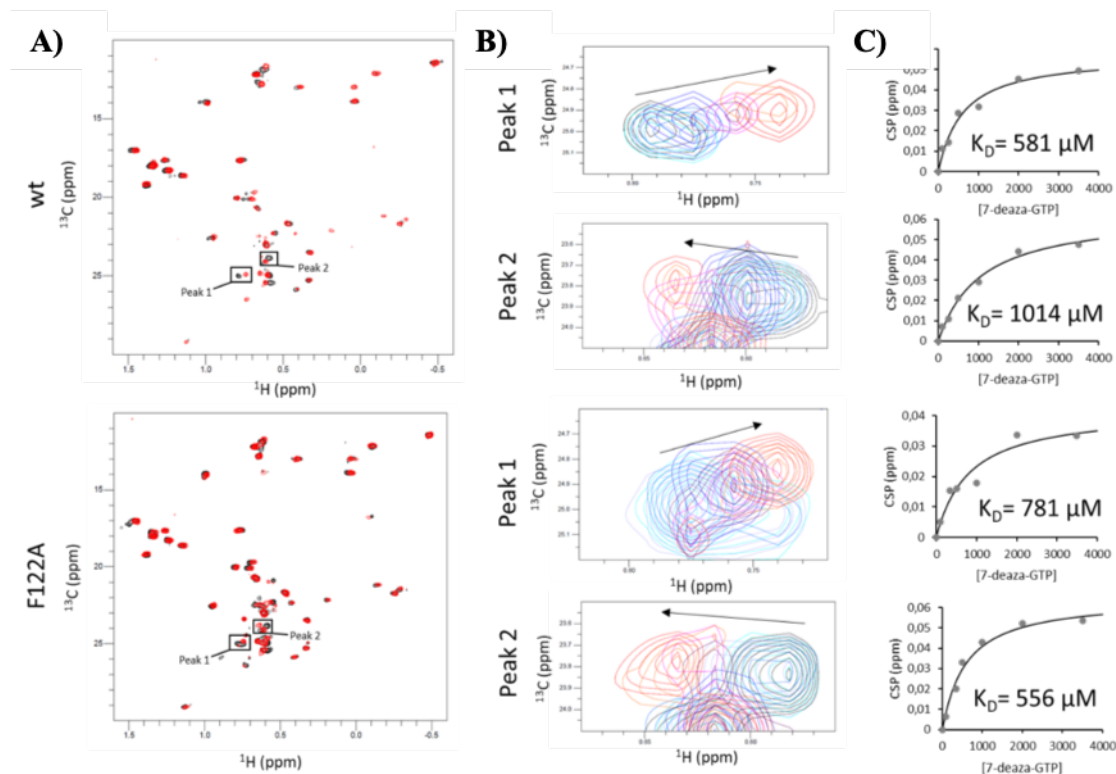


Figure 37: K_D determination of 7-deaza-GTP using protein NMR: **A)** ^1H , ^{13}C correlation spectra of GCH1 wt (upper panel) or F122A (lower panel) free (black) and in presence of 3.5 mM 7-deaza-GTP (red). Boxes mark the peaks used for fitting the titration curves. **B)** Peak 1 and Peak 2 from A in the presence of increasing concentrations of 7-deaza-GTP. **C)** Chemical shift perturbation extracted from spectra in B is plotted against the 7-deaza-GTP concentration (dots). The fitting curve is depicted as black line and the dissociation constant is indicated.

To shed more light onto the absence of any enzymatic activity of the key mutant F122A, we investigated whether substrate binding was impacted by the mutation.

We used Saturation Transfer Difference (STD) NMR spectroscopy to study binding of the substrate analog 7-deaza-GTP to wtGCH1 and the F122A mutant. This technique allows to make qualitative statements about the change of the binding kinetics within a system [68, 74, 69]. 7-deaza-GTP was added in increasing concentration to proteins. We then compared the K_D values and the STD

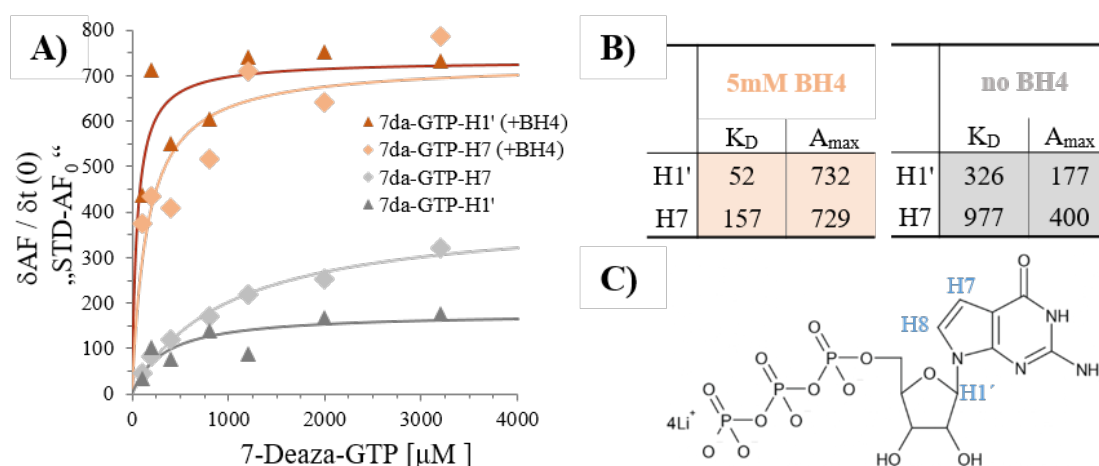


Figure 38: K_D determination using initial slopes from STD NMR build up curves: **A)** For each ligand concentration a set of measurements was recorded applying different saturation times (t_{sat}). To obtain STD AF_{max} values and the saturation rate constants k_{sat} from STD NMR build up curves experimental STD AF values were fit to a rising exponential: $\text{STD AF} = \text{STD AF}_{\text{max}} (-1 \exp(-k_{\text{sat}} t_{\text{sat}}))$. From the fitting parameters initial build up slopes ($t_{\text{sat}} = 0$) were calculated: $\text{STD AF}_0 = \text{STD AF}_{\text{max}} k_{\text{sat}}$. These STD AF_0 values were plotted against the ligand concentration yielding a binding isotherm from which K_D can be derived by fitting the Langmuir binding model: $\text{STD AF}_0 = A_{\text{max}} / (1 + (K_D/c))$. A_{max} is a scaling factor representing the maximum STD amplification. Two different 7 deaza-GTP protons (H1' and H7) were monitored in these experiments. **B)** All K_D and A_{max} values are summarized in the table. **C)** Assignment of relevant protons on structural formula of 7 deaza-GTP.

enhancement factors for F122A-GCH1 with wtGCH1 and its complexes in presence and absence of effector molecules. Further K_D s were determined by protein NMR (Figure 37).

The STD amplification factor data show that the affinities of substrate to all proteins used do not vary beyond a factor of two (Figure 37). However, determination of the maximal STD amplification factor for 7-deaza-GTP (Figure 37B) showed drastically higher factors for BH4-inhibited wtGCH1, either alone or in complex with GFRP, compared to uninhibited enzyme (Figure 38). In contrast, the F122A mutant shows no differences. Enhancements in the maximal STD amplification factor are indicative of enhanced ligand binding kinetics. We thus conclude that highly accelerated substrate binding kinetics in wtGCH1 are induced by BH4 binding, both in the absence and presence of GFRP. Since F122A-GCH1 is not

affected, we presume that for this mutant substrate binding kinetics are fast due to the absence of the F122 side chain, which forms a lid over the active site in substrate complexes of GCH1. Addition of BH4 does not further accelerate substrate dissociation in this case.

To shed more light onto the mechanism of BH4 induced inhibition of GCH1, we used Saturation Transfer Difference (STD) NMR spectroscopy to study binding of the substrate analog 7-deaza-GTP to GCH1. STD NMR can be used to determine the K_D of ligands (feasible in the range between 10^{-2} and 10^{-6} M) and allows to make qualitative statements about the change of ligand binding kinetics [68, 74, 69]. STD NMR experiments were based on a titration of 7 deaza-GTP to GCH1 in the presence or absence of BH4. We measured a series of STD build up curves (i. e. STD effects at a constant ligand concentration but increasing saturation times) at each 7 deaza-GTP concentration for the protons H7 and H1' of the substrate analogue. From the concentration dependence of the initial build up slopes the dissociation constant as well as the maximum STD amplification for the monitored proton signal can be derived (Figure 38AB).

The binding isotherms derived from the STD experiments resulted in a comparable affinity of GCH1 to 7 deaza-GTP as determined by protein NMR (Figure 37) and showed that the BH4-bound, inhibited GCH1 is able to bind substrate in a similar affinity range to the active form of the enzyme. In fact, paradoxically the affinity of the substrate analog appears to be about six-fold higher for the inhibited enzyme. We concluded that BH4-induced inhibition of GCH1 must be triggered by another, non-affinity-driven mechanism. Determination of the maximum STD amplification (A_{max}) for 7-deaza-GTP (Figure 38AB) showed an increase by a factor of about 3 for BH4-inhibited GCH1 compared to the uninhibited enzyme. This enhanced STD response is indicative of accelerated ligand binding kinetics, if the effect of changes in the proton network in the environment of the ligand binding site can be excluded [3]. We thus conclude that highly accelerated substrate binding kinetics in GCH1 are induced by BH4 binding and thereby could cause the inhibition of GCH1 in presence of BH4.

3.6 Formation of the stimulatory hGCH1-hGFRP complex upon binding of aromatic amino acids

GCH1's downstream product BH4 is an essential cofactor for the aromatic amino acid hydroxylases (phenylalanine hydroxylase, tyrosine-3-hydroxylase, and tryptophan-5-hydroxylase). Feed-forward activation of GCH1 via phenylalanine induced GFRP-GCH1 complex formation enhances GCH1's enzymatic activity and eliminates substrate cooperativity. It has not yet been investigated whether other aromatic amino acids, such as tyrosine or tryptophan, can induce the formation of the stimulatory complex and thus modulate GCH1 activity.

Figure 39A depicts the melting curves for the GCH1 and GFRP as well as GCH1 and GFRP mixtures in presence and in absence of BH4. The fusion of the individual protein signals into one single melting point clearly indicates an interaction of the two proteins, which is only observed in the presence of 0.1 mM BH4. The same effect can also be observed in the presence of 20 mM phenylalanine, whereby the melting point of this stimulatory complex shows a higher thermal stability than the inhibitory complex induced by BH4 (Figure 39 B). Strikingly, there seems to be no interaction between GCH1 and GFRP in the presence of 20 mM tyrosine or tryptophan Figure 39 CD. This suggests that the stimulatory complex is formed exclusively in presence of phenylalanine and that phenylalanine is the only aromatic amino acid capable of modulating GCH1 activity. No complex formation occurs in the absence of the small effector molecules Phe and BH4.

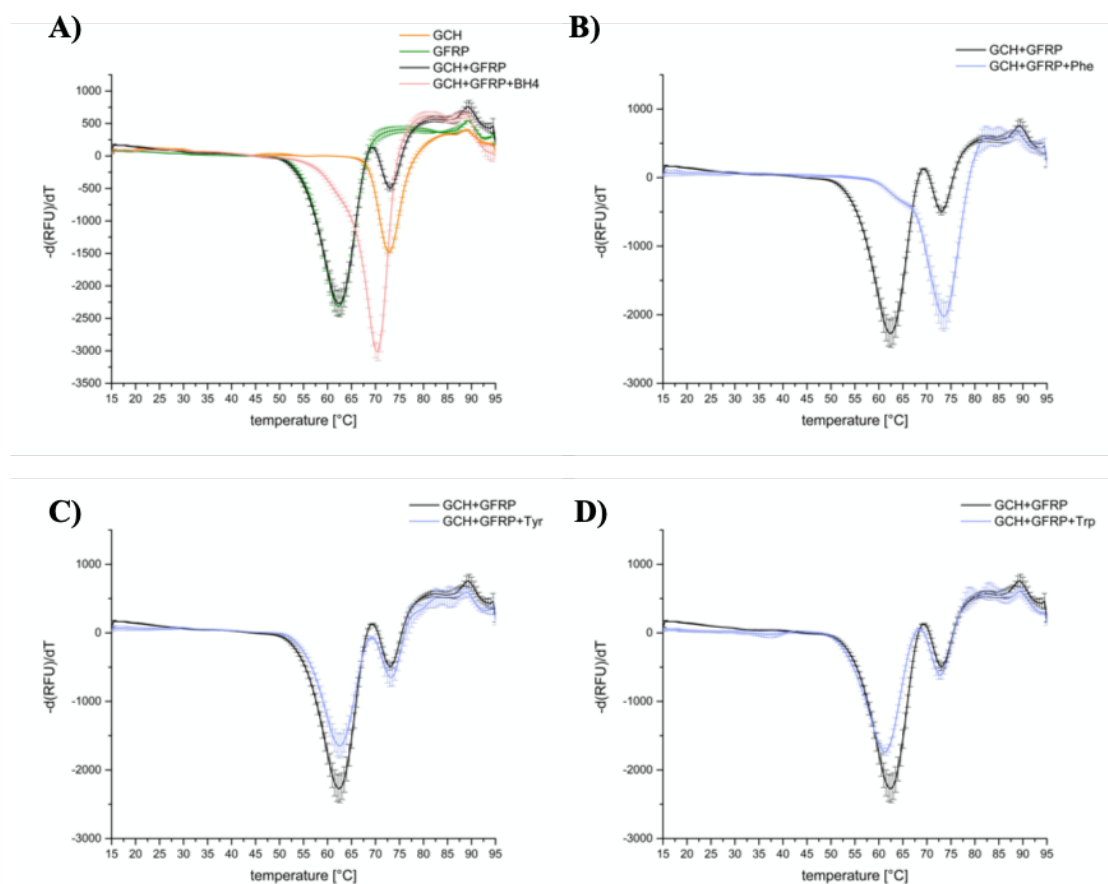


Figure 39: DSF analysis of the GCH1-GFRP complex formation induced by aromatic amino acids: **A)** Determination of protein melting points using DSF. TMs of GCH1 (orange), GFRP (green), GCH + GFRP (black), GCH + GFRP + 0.1mM BH4 (red) are 73 $^{\circ}\text{C}$, 62.5 $^{\circ}\text{C}$, 73 and 62.5 $^{\circ}\text{C}$ and 70.5 $^{\circ}\text{C}$ respectively. **B)** TM of 75 $^{\circ}\text{C}$ was measured for the GCH1 + GFRP + 20 mM Phenylalanine (blue). The black melting curve derives from mixture of GCH1 and GFRP in absence of small effector molecules. The same setup is shown for GCH1 and GFRP in presence of **C)** 20 mM Tyrosine (blue) or **D)** 20 mM Tryptophan (blue).

3.7 SPR analysis of hGCH1-hGFRP complex formation

The DSF data shown above, together with previously published size exclusion chromatography and crystallographic data already showed that the allosteric regulators Phe or BH4, are essential for the formation of stable stimulatory and inhibitory complexes. Our SPR data confirm the basic features of GCH1-GFRP complex formation and offer further insights into binding kinetics and protein

interaction affinity.

hGCH1 was immobilized on the CM5 biosensor using standard amino coupling chemistry. Formation of the stimulatory complex GCH1-GFRP occurs exclusively in the presence of high concentrations of L-phenylalanine (Figure 40A). The concentration of Phe that is necessary to obtain the completely saturated formation of free GCH decamers with GFPR pentamers, was determined in a titration experiment (Figure 40 A), where Phe concentration was analyzed in the concentration range of 78.1 μM to 10 mM. No or minor formation of hGCH1-hGFRP complex was observed at low Phe concentration. Significant formation of stimulatory complex was observed at concentration of 625 μM and saturation of hGCH1 with hGFRP was reached at 10 mM. The apparent EC50 of complex formation is 2000 μM .

The dependence of the formation of the stimulatory complex on hGFRP concentration was determined by measuring the response of full-length hGCH to rising hGFRP concentrations in the presence of 10 mM phenylalanine (Figure 41 A). The ternary complexes form with 413 pM affinity. Absence of Phe in the running buffer results in extremely rapid off-rates. In contrast, we observed very slow dissociation of the complex in the presence of Phenylalanine in the running buffer (Figure 41 B). Table 15 shows k_{off} , k_{on} and K_{D} values for the formation of the stimulatory complex.

For the inhibitory complex, a similar picture emerged. We observed binding of hGFRP to full-length hGCH1 only in the presence of allosteric regulator BH4. Formation of tertiary complex of GCH1-GFRP-BH4 depends on the BH4 concentration and saturation of hGFRP binding to hGCH1 appears at BH4 concentrations above 500 μM (Figure 40 B). The apparent EC50 of complex formation is 125 μM . Dissociation of tertiary complex of hGCH1/hGFRP/BH4 occurs rapidly in the absence of BH4 (Figure 41C). The ternary complexes form with 108 pM affinity. As expected, the dissociation of the hGCH/hGFRP complex is very slow in the presence of BH4 in the running buffer (Figure 41D). Dissociation of the complex is about 20-fold faster in comparison with stimulatory complex.

In conclusion, the presence of the allosteric binders BH4 or Phe is absolutely necessary for the formation of inhibitory or stimulatory complex, respectively. Dissociation of both complexes in the absence of any of allosteric substrates occurs immediately. Observed fast dissociation of the complex in the absence of any

allosteric substrate is most probably driven by the fast dissociation of the weakly binding allosteric effector molecules from each complex. Kinetic and thermodynamic data for stimulatory and inhibitory complexes, determined in the presence of the allosteric binders show very tight binding in the picomolar range. Both complexes are very stable and show extremely slow dissociation. Dissociation of stimulatory complex is slower than of inhibitory complex.

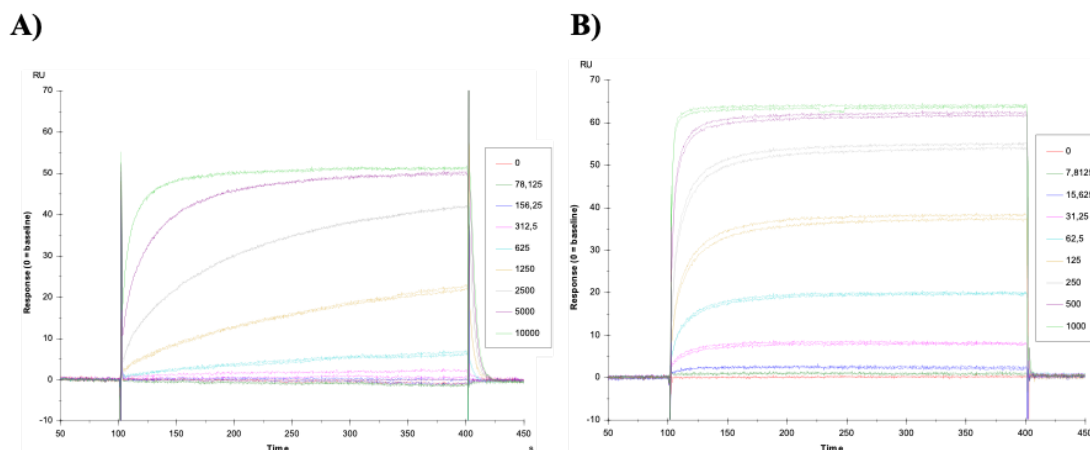


Figure 40: hGCH1-hGFRP complex formation in dependence of the effector molecules Phenylalanine and BH4: A) Binding of GFRP at 2 μM to hGCH1 in the presence of Phenylalanine. Concentration of Phenylalanine was varied in the range of 10.0 mM to 78.1 μM . **B)** Binding of GFRP at 2 μM to hGCH1 in the presence of BH4. Concentration of BH4 was analyzed in the range of 1.00 mM to 7.81 μM .

Table 15: Determined values for k_{on} , k_{off} and K_{D} SPR measurements. The values were collected in triplicates

	running buffer	k_{on}	k_{off}	K_{D}
FL-stimulatory complex	with Phe	$4.24. \times 10^4$	$4.58. \times 10^{-6}$	108.0 pM
	without Phe	n.d.	0.26	n.d.
FL-inhibitory complex	with BH4	$2.24. \times 10^5$	$9.23. \times 10^{-5}$	412.7 pM
	without BH4	n.d.	0.52	n.d.
$\Delta 42$ -stimulatory complex	with Phe	$6.52. \times 10^4$	1.00×10^{-6}	15.4 pM
	without Phe	n.d.	0.15	n.d.
$\Delta 42$ -inhibitory complex	with BH4	$3.22. \times 10^5$	8.80×10^{-5}	265.0 pM
	without BH4	n.d.	0.31	n.d.

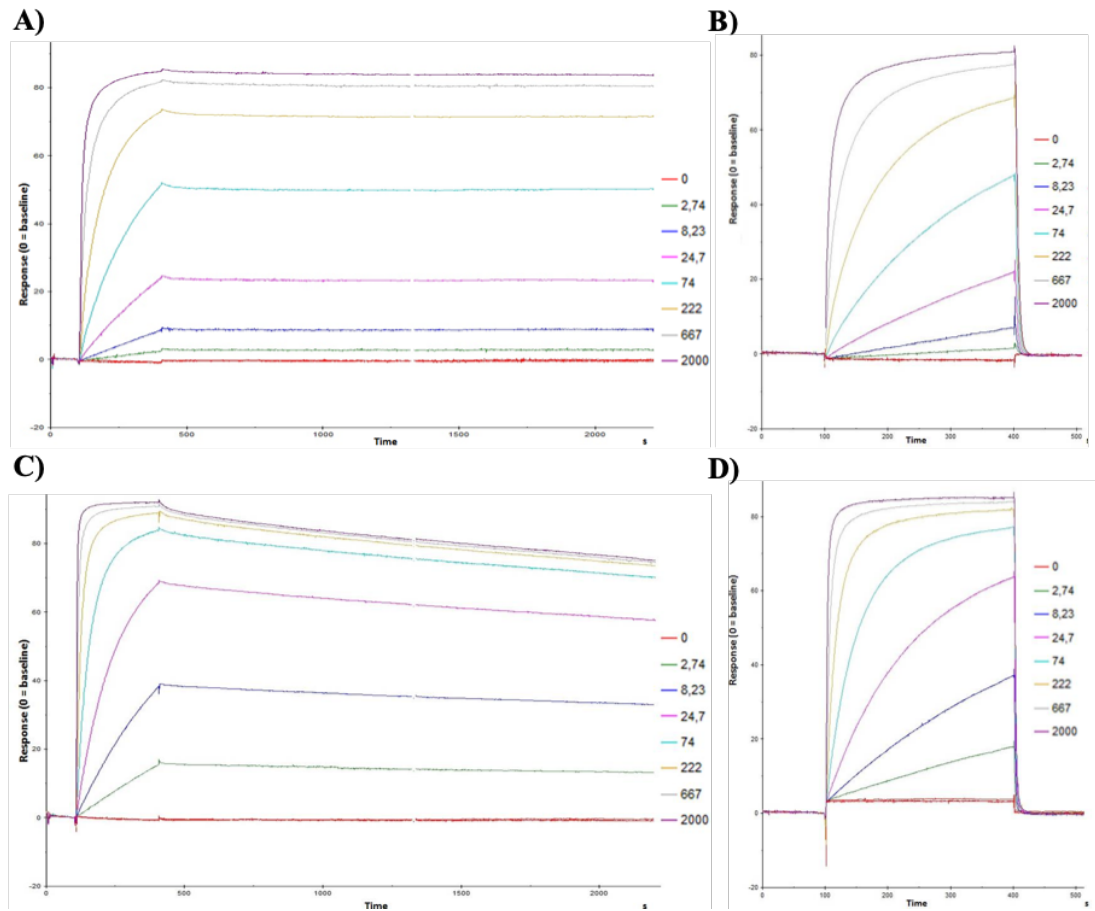


Figure 41: SPR analysis of the complex formation using different hGFRP concentrations and full-length hGCH1: **A)** Binding of hGFRP to FL-hGCH1 in the presence of 10 mM Phe. Binding of hGFRP was tested in the concentration range of 2.74 nM to 2000 nM. **B)** Binding of hGFRP to FL-hGCH1 in the presence of 1 mM BH4. Binding of GFRP was tested in the concentration range of 2.74 nM to 2000 nM. **C)** Same experimental setup than in A) but with 10 mM Phe in running buffer. **D)** Same experimental setup than in B) but with 1mM BH4 in running buffer.

3.8 Role of GCH1's N-terminus on enzyme activity and complex formation

In addition to the analysis of the full-length protein (Figure 41), the same analysis of complex formation as a dependence of hGFRP was performed with the truncated $\Delta 42$ -hGCH1 variant (Figure 42). The $\Delta 42$ -hGCH1 showed the same behavior as the full-length protein: without a small molecule in the running buffer, the complex

disintegrated almost instantly (Figure 42AC). In contrast, the small molecule containing buffer induced a high-affinity binding of the complex partners and almost no dissociation of hGFRP (Figure 42BD). As with full length, the association with BH4 seemed to be faster, but dissociation with phenylalanine seemed slower than with BH4. Comparing the associations between FL- and $\Delta 42$ -hGCH1, the associations of $\Delta 42$ -hGCH1 appeared to be faster than those of FL-hGCH1. Beside this, the full-length and N-terminal truncated hGCH1 show no significant difference.

In the enzyme activity assays we found a higher activity for the truncated enzyme both alone and in the stimulated complex (Figure 43) similar to previously published data on the rat enzyme [41]. However, the specific activity was only approximately 20% higher and the differences in K_M and Hill coefficients were similarly small.

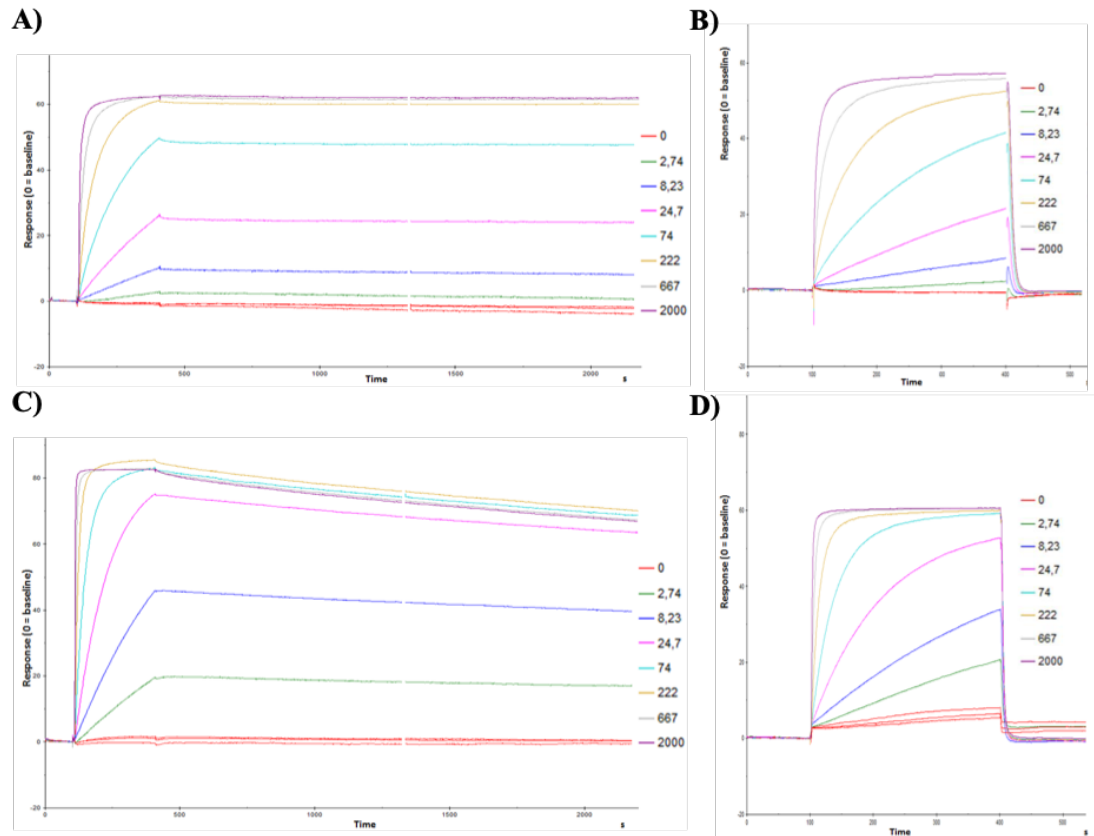


Figure 42: SPR analysis of the complex formation using different hGFRP concentrations and $\Delta 42$ -hGCH1: **A)** Binding of hGFRP to $\Delta 42$ -hGCH1 in the presence of 10 mM Phe. Binding of hGFRP was tested in the concentration range of 2.74 nM to 2000 nM. **B)** Binding of hGFRP to $\Delta 42$ -GCH1 in the presence of 1 mM BH4. Binding of GFRP was tested in the concentration range of 2.74 nM to 2000 nM. **C)** Same experimental setup than in A) but with 10 mM Phe in running buffer. **D)** Same experimental setup than in B) but with 1 mM BH4 in running buffer.

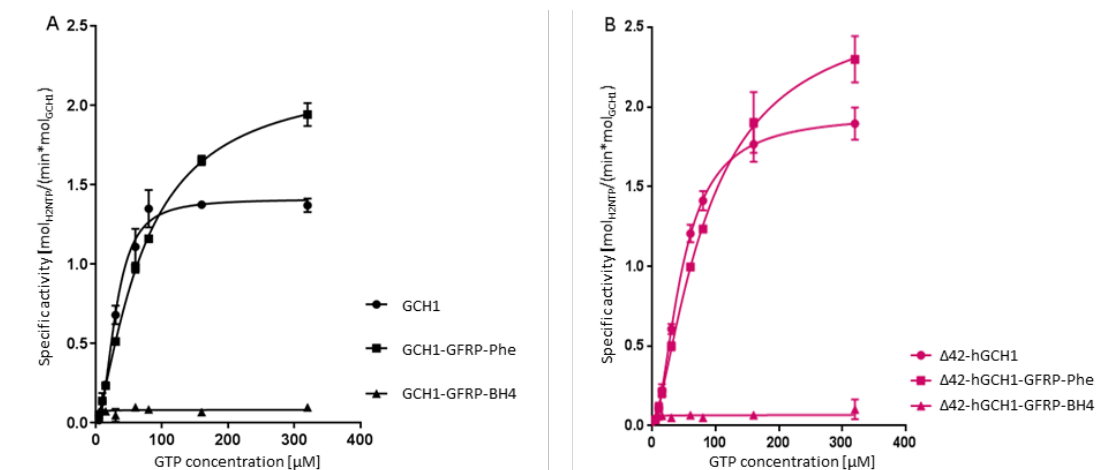


Figure 43: Specific activity of full-length and $\Delta 42$ -hGCH1: **A)** Binding of hGFRP to $\Delta 42$ -hGCH1 in the presence of 10 mM Phe. Binding of hGFRP was tested in the concentration range of 2.74 nM to 2000 nM. **B)** Binding of hGFRP to $\Delta 42$ -GCH1 in the presence of 1 mM BH4. Binding of GFRP was tested in the concentration range of 2.74 nM to 2000 nM. **C)** Same experimental setup than in A) but with 10 mM Phe in running buffer. **D)** Same experimental setup than in B) but with 1mM BH4 in running buffer. Specific activity of fl-hGCH1 **A)**, black colors) and $\Delta 42$ -hGCH1 **B)**, red colors) with effects of GFRP mediated stimulation or inhibition. Both protein variants show largely similar behavior.

3.9 Small molecule effectors change conformations of GCH1 or GFRP

To understand and visualize how the binding of low molecular weight effectors can modulate the affinity of two proteins so drastically as seen in the SPR measurements shown above, we analyzed the protein-protein interfaces of all proteins in the apo, ligated and complex-bound state. When analyzing the rGCH1-rGFRP structures Maita et al. claimed that by binding of phenylalanine to GFRP the total buried surface accessible surface area of each GFRP-GCH1 interface is significantly increased, when compared to the same structure without phenylalanine [66]. They conclude that the increase the contact area between GFRP and GCH1 by the binding of phenylalanine to GFRP explains the change in affinity. We used PISA [50] to calculate the interface surface area of the stimulatory and inhibitory human complexes and a hypothetical modelled “stimulatory complex” using non-liganded GFRP instead of GFRP-Phe. The interfaces of the human complexes span an area of 1,951 Å² and 1,950 Å² while the surface area of the hypothetical, unliganded complex is 1,806 Å². We conclude that it is not the change in size of the buried surface area that gives rise to the observed association behavior characterized by a switch from no to picomolar affinity.

We went on to closely analyze the conformational changes observed in GCH1 and GFRP as well as the associated changes in protein surface topology upon small molecule effector binding and any close contacts formed between the small molecules, BH4 bound to GCH1 and Phe bound to GFRP, respectively, and the corresponding two protein binding partners (Figure 44). We found that binding of phenylalanine to GFRP induces the same GFRP conformation, which GFRP takes on in the stimulatory complex (Figure 44BC). Thus, it is clear that this conformational state is caused by phenylalanine alone. In this case, it is mainly changes in Ile10, Gln9 and Gln75 that alter the surface of GFRP. The effector molecule Phe does not directly interact with GCH1. The corresponding modulation of the surface of GFRP-Phe now facilitates the interaction with GCH1. GCH1 hardly undergoes any conformal changes and its GFRP facing surface remains largely in the non-liganded state (Figure 44EG).

The same applies to the conformational changes in the inhibitory complex. The

change in quaternary structure of GCH1 in the GFRP complex is very similar to changes induced by BH4 derivatives alone (Figure 44FH) [21]. There are also no direct interactions between BH4 and GFRP in the inhibitory complex. The BH4 induced large conformational changes in GCH1 alter its surface structure. Conformational rearrangements mainly involve the region 231-239 and 195-200. GFRP remains in the apo state (Figure 44AD).

In summary, small molecule effectors change conformations of GCH1 or GFRP and their surface structures and electrostatics facilitating high affinity molecular recognition. The effector molecules are not involved in the complex formation but are essential for the induction of the specific protein surface structures that are capable of forming the observed protein-protein interaction. The presence of the effector molecules is therefore a pre-requisite for high affinity binding between GCH1 and GFRP. Without an effector molecule, both proteins are present in the 'apo' conformations, which do not present compatible surfaces for mutual binding. The extremely fast dissociation of the complexes in the absence of BH4 or Phe is likewise explained by the structural findings.

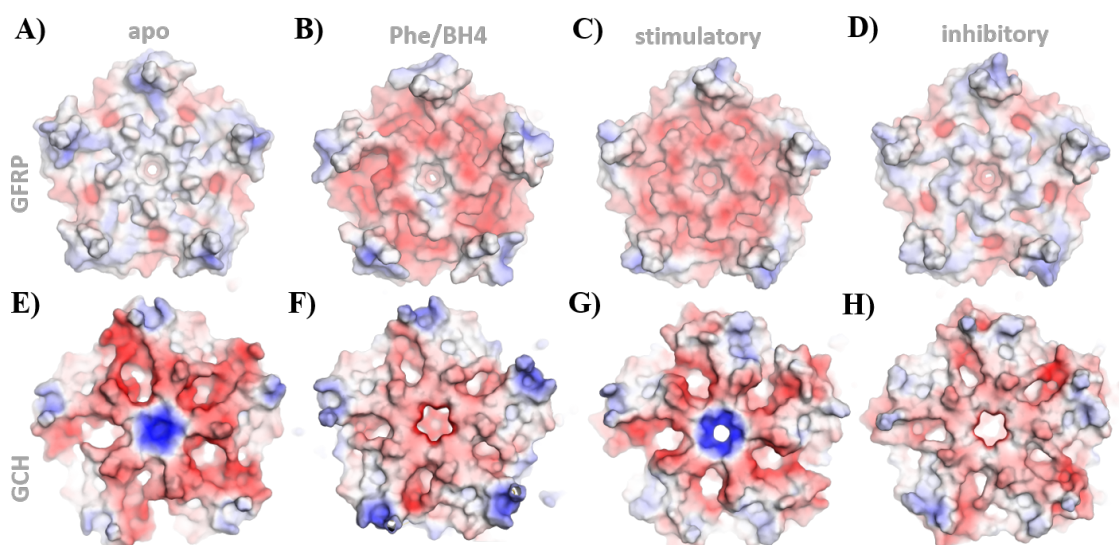


Figure 44: Surface representation of different conformational states in GCH1 and GFRP colored by electrostatics: A) GFRP. B) GFRP-Phe. C) GFRP-Phe in stimulatory complex. D) GFRP in inhibitory complex. E) GCH1. F) GCH1-allosteric binder. G) GCH1 in stimulatory complex. H) GCH1-BH4 in inhibitory complex.

3.10 Characterization of allosteric binders

A fragment based screening (FBS) campaign was conducted (not part of this work) to find novel inhibitors for GCH1. The hit-finding cascade mainly included biophysical methods for ligand binding detection, such as NMR and DSF. In general, there are many proteins that bind nucleotides so it is considered difficult to find selective binders for GCH1 that bind to the active site. Therefore, it was avoided to target the active side and the screening focused on allosteric binders only. All studies were conducted with addition of an high affinity active site binder (8-oxo-GTP) in order to block the active site and limit the search to allosteric compounds only. Approximately 20 substances could be identified that bind to hGCH1 in presence on substrate analogues.

Within this work, we aimed to characterize the identified binders and identify their mode of action. It was tested whether the compounds are inhibiting the activity of GCH1 using an enzymatic assay. Figure 45 AB shows the specific activity GCH1 plotted versus substrate concentration.

The enzymatic data generated here clearly shows that cpd2 compound has an inhibitory effect, while cpd3 has no influence on enzyme activity (Figure 45). Further, they were tested on their ability to form hGCH1-GFRP complexes, using a DSF assay. Analogous to BH4, cpd2 induces the complex formation, while the inactive fragment cpd3 does not form a GCH1-GFRP complex.

Crystal structures of this fragments (Figure 46) reveal the binding mode and therefore help to understand the mode of action of this compounds. Here, the formation of a salt bridge between Arg235 and Asp127 is prevented by sterically demanding fragments, thus disturbing the integrity of the inhibitory conformation. In summary, we were able to distinguish between binders and inhibitory fragment-like molecules and threfor diliver starting points for the development of allosteric inhibitors and compounds that preserve GCH1's activity.

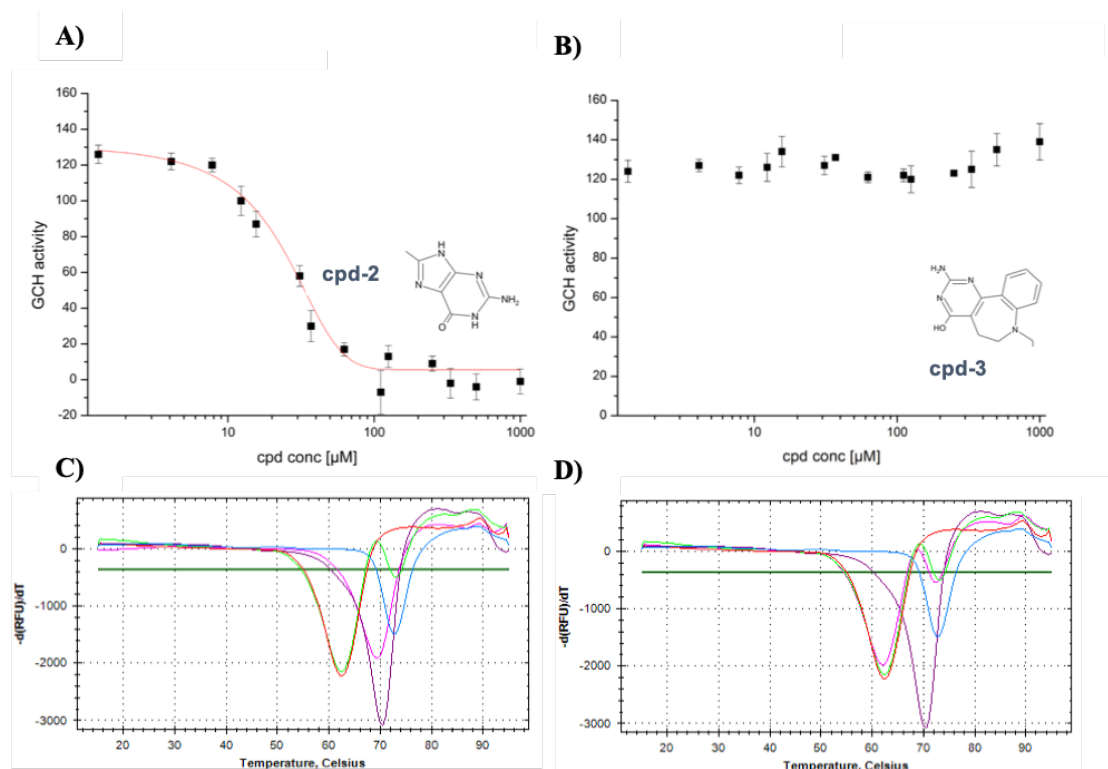


Figure 45: Characterization of allosteric binder using an enzyme assay and DSF: Specific enzyme activity of **A)** hGCH1 and cpd2 and **B)** cpd3 using various compound concentrations and a substrate concentration varying from 1-2000 μM GTP. Specific activity GCH1 plotted versus substrate concentration. Fitted by using the Hill equation ($n = 3$) (line-plot). DSF assay monitoring the complex formation of hGCH1 and hGFRP in presence of **C)** cpd2 and **D)** cpd3. First derivatives of melting traces of hGCH (red), hGFRP (blue), hGCH + hGFRP (green), hGCH + hGFRP + BH4 (dark violet) and hGCH + hGFRP + cpd2/3 (light violet).

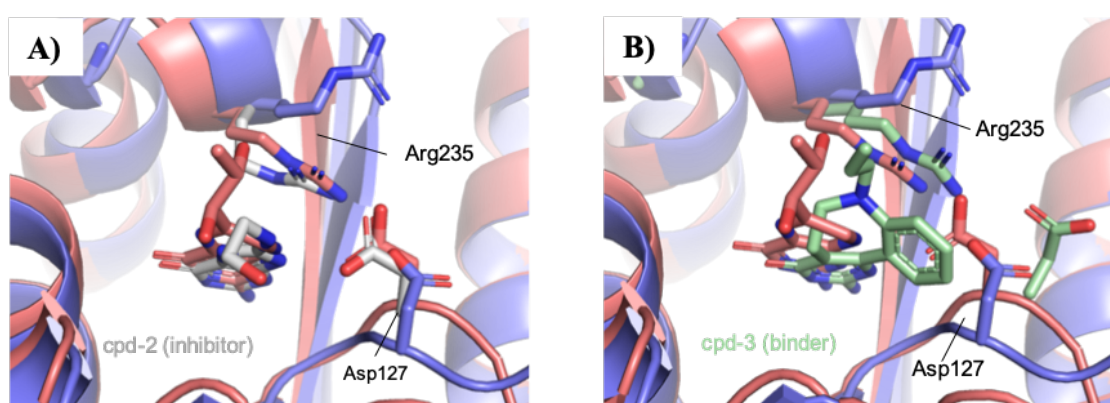


Figure 46: Co-structures of hGCH1-hGFRP complexes with cpd-2 and cpd-3: Allosteric pocket of the inhibitory hGCH1-hGFRP complex (salmon) overlaid with the stimulatory hGCH1-hGFRP complex (light blue). **A)** Superimposition with the cpd-2 (grey) hGCH-hGFRP structure. **B)** Superimposition with the cpd-3 (green) hGCH-hGFRP structure. A salt bridge is formed between Arg235 and Asp127 in the inhibitory (salmon) and the cpd-2 soaked (grey) complex, while it is not formed in the stimulatory (light blue) and the cpd-3 soaked (green) complex.

4 Discussion and Conclusions

4.1 Preparation of high quality proteins

The structural analysis of hGCH1 and hGFRP depends on large amounts of protein with high purity to carry out biophysical and crystallographic experiments. Full-length and N-terminal truncated ($\Delta 42$ -hGCH1) hGCH1, including several point mutated variants, as well as hGFRP were successfully expressed and purified. The hGFRP and hGCH constructs were expressed in *E.coli*. High to medium amounts, up to 10-4 mg protein per liter culture medium were obtained for all proteins. All hGCH and hGFRP proteins were purified up to 98-95 % purity. Size exclusion chromatography showed one sharp peak corresponding to the expected size. Overall, the purified proteins exhibited good stability and showed no tendency for aggregation or degradation, even after several weeks. Further protein activity, stability and the ability to form complexes and bind the substrate GTP was tested in order to guarantee highest protein quality and to avoid batch-to-batch variations.

4.2 Novel structures and hybrid approaches

Here, we describe a comprehensive structural study, which aims to advance the current knowledge on the allosteric regulation of GCH1.

Table 16: Summary of derived structures within this work.

	structure name	method	PDB code	cpd
GCH	GCH1	X-ray	6Z87	-
	GCH1+allosteric	X-ray	6Z88	AXSP0056BS
	GCH1+allosteric2	X-ray	6Z89	AXSP0056BS (partially occupied)
	GCH1+active	X-ray	6Z86	7-deaza-GTP
GFRP	GFRP	X-ray	7ACC	-
	GFRP+Phe	X-ray	7AL9	Phe
complex	GCH1+GFRP+Phe	X-ray	7ALC	Phe
	GCH1+GFRP+Phe+active	X-ray	7ALB	7-deaza-GTP + Phe
	GCH1+GFRP+allosteric	X-ray	7ALA	DI00613584
	GCH1+GFRP+allosteric+active	X-ray	7ALQ	7-deaza-GTP + BH4
	GCH1+GFRP+allosteric	cryo-EM	6Z85	BH4
	GCH1+GFRP+Phe+active	cryo-EM	6Z80	8-oxo-GTP + Phe

We crystallized hGCH1 in the presence and absence of allosteric and active site ligands. In order to allow the protein to arrange in its preferred conformation,

all crystals were generated by co-crystallization. We obtained crystal structures of different conformational states and varying levels of occupancy of ligand binding. These structural snapshots helped to delineate the consequences of ligand binding to the GCH1 allosteric site and their influence on the protein conformation. Table 16 shows the ensemble of generated structures. This work shows for the first time the structure of the human GCH1-GFRP complexes and the human GFRP, both in different regulatory states. In addition, the effect of allosteric inhibitors on GCH1 in absence of its regulator protein GFRP has never been structurally investigated before. This aspect is elaborated by the determination two structures that show GCH1 in fully and partially inhibited states. The obtained details were essential for understanding both, the mode of action of allosteric inhibitor and the role of GFRP in inhibition of GCH1.

In contrast to all previous publications, in which only one structural method was used, we are using a hybrid approach, utilizing cryo-EM, X-ray crystallography and several biophysical methods. We suspected from analysis of the crystal structures of the rGCH1-rGFRP complexes [66, 65]. that important functional regions on the protein surface undergo order-disorder transitions on the trajectory from active to inactive or substrate-bound states and could be impacted by crystal packing. Therefore, we decided to use cryo-EM as a complementary approach to resolve the structures of hGCH1-hGFRP complexes in an aqueous environment, unbiased by crystal contacts.

4.3 Identification of allosteric binders and inhibitors

In contrast to potent orthosteric inhibitors, there is little evidence of potent allosteric inhibitors. To achieve selectivity, however, allosteric modulators are more promising than molecules that address the nucleotide binding site, since these pockets are found in many proteins and are usually highly conserved. Besides identifying initial starting points addressing the allosteric site and providing structural data, we further characterized those compound and determined their modes of action. We have found allosteric compounds that have an inhibitory effect on GCH1 and substances that only bind to GCH1. This discovery could be essential and not only drive the development of more potent GCH1 inhibitors, but also the unique

approach of inhibiting inhibition by BH4 and thus maintaining the activity of GCH1. Both types of modulators are the first structurally, enzymatically and biophysically characterised allosteric compounds in the context of GCH1 and therefore set promising milestones in the development of potential drugs to modulate GCH1 activity and thus BH4 levels in the cell.

4.4 Stimulation of GCH1-GFRP is exclusively triggered by L-Phenylalanine

BH4 is involved as an essential cofactor for the aromatic amino acid hydroxylases, which catalyze the conversion of L-phenylalanine to L-tyrosine, L-tyrosine to L-DOPA and L-tryptophan to 5-hydroxy-L-tryptophan [47]. So far, it was known that phenylalanine can bind to GFRP, which triggers the formation of the stimulatory complex and thereby leads to a reduction in cooperativity and thereby to an increase in the activity of GCH1. It was unknown whether other aromatic amino acids like tyrosine or tryptophan also address the same feedback mechanism and can bind GFRP, allow formation of GCH1-GFRP complexes and thus stimulate GCH1. In this study we show by DSF experiments that the stimulatory complex is only formed in presence of phenylalanine but not upon addition of tyrosine or tryptophan. Therefore, feedback stimulation seems to be exclusively triggered by phenylalanine.

4.5 The N-terminus of hGCH1 does not influence hGFRP binding and enzymatic activity

The C-terminal domain of GCH1, which is directly involved in catalysis and is responsible for oligomerization of the protomers, has evolved very conservatively. For instance, the terminal 120 residues exhibit a 60% identity between the *E. coli* and the human enzymes suggesting that both the catalytic mechanisms as well as the quaternary structures of GCH1 are very similar across species [64, 86, 113]. In contrast, much greater sequence variability is found at the N-termini of known sequences, indicating that any functional role of the GCH1 N-terminus is unrelated to oligomerisation or catalysis. Further, biochemical and structural data indicate

instability of this part of the human and rat GCH1 sequence and its propensity to proteolytic cleavage [66, 65, 4]. Analysis of the nature of the sequence suggests that it constitutes a low complexity region and is most probably disordered in the isolated GCH1 structure [130]. In fact, in the published rat complexes the N-terminal domain is not visible in the electron density most probably due to dynamic disorder [66]. Possible functional roles of the N-termini of mammalian GCH1s include the binding of accessory proteins such as SH3 domains or Aha1 [110].

Previous work has delivered conflicting data about effects of the presence of the N-terminal sequence stretch comprising amino acids 1-42 of hGCH1 on enzymatic activity and GFRP recruitment [110, 41, 42]. In order to shed light on the potential role of the N-terminus on these parameters, we first ensured the availability of high quality protein material of both full-length (FL)-hGCH1 and the truncated Δ 42-hGCH1 variants and performed SPR and enzyme activity assays described above for both species.

In the SPR setup, Δ 42-hGCH1 showed the same behavior as the FL protein: without a small molecule effector in the running buffer, the complex disintegrated almost instantly. In contrast, the small molecule containing buffer induced a high-affinity binding of the complex partners and almost no dissociation of hGFRP. Comparing quantitative binding data, highly similar on- and off-rates as well as dissociation constants are determined for both hGCH1 variants (highest difference of factor 5) and similar trends with respect to BH4 vs. Phe binding. The absence of significant differences in the protein interactions suggest that the presence of the N-terminal domain does not have any impact on GFRP recruitment.

In the enzyme activity assays we found a higher activity for the truncated enzyme both alone and in the stimulated complex similar to previously published data on the rat enzyme [41]. However, the specific activity was only approximately 20% higher and the differences in K_M and Hill coefficients were similarly small.

We further provide unequivocal evidence about the role of the GCH1 N-terminus on enzymatic activity as well as in GCH1-GFRP complex formation. While Hussein et al. and Higgins and Gross, [42, 41] suggest that the N-terminal region confers higher activity, induces GFRP binding in the absence of small molecule effectors and may even function as an autoinhibitory element, our data clearly show very little effect and thus suggest that the physiological role of the N-terminal region may

indeed be unrelated to the enzymatic function and its allosteric control, but may rather lie in establishing interactions between GCH1 and other binding partners as suggested by a yeast-two-hybrid study [110].

4.6 Small molecule effectors facilitate pico-molar recognition of hGCH1 and hGFRP

Small molecule effectors change conformations of GCH1 or GFRP and their surface structures facilitating high affinity molecular recognition. The effector molecules are not directly involved in the complex formation but are essential for the induction of complementary, interlocking surfaces. The presence of the effector molecules is therefore a pre-requisite for high affinity, picomolar binding between GCH1 and GFRP. Without effector molecules, both proteins adopt the "apo" conformations, which do not provide compatible surfaces for mutual binding and therefore lack affinity to each other. A consequence is the extremely fast dissociation of the complexes in the absence of BH4 or Phe, which is most probably driven by the fast dissociation of the weakly binding allosteric effector molecules from each complex and swiftly followed by GFRP dissociation. These observations strengthen the hypothesis of GFRP's role as a scaffolding protein that functions by either stabilizing the apo or BH4 bound states of GCH1. The stabilization of the inactive state of GCH1 in the presence of GFRP causes an increase of BH4 affinity and a boost of its inhibitory potency. This supports GFRP's biological role as metabolic sensor and enables rapid and effective modulation of GCH1's activity. In previous reports, evidence has been provided that GCH1 and GFRP may interact tightly in the absence of small molecule effectors [42, 41]. Our data clearly show that this is not the case. It is difficult to speculate what may be the reason for the discrepancy. We also observed complex formation in the absence of BH4 and Phe when GTP was present in the buffer system (data not shown). We speculate that presence of GTP in the assays may have caused the production of product H2NTP, which can likewise be able to trigger complex formation, since it features the identical diaminohydroxypyrimidine pharmacophore. It is possible that the literature observations can be traced back to this phenomenon. Further, while Hussein et al. had published the first SPR data on this protein-protein interaction

(PPI) and measured K_D 's in the 10nM range, our careful analysis of the PPI based on high quality SPR data has shown that the interaction between GCH1 and GFRP is in fact in the 100pM range and thus 100-fold tighter [42].

4.7 GFRP acts as a scaffolding protein that sensitizes GCH1 to react to physiological levels of effector molecules BH4 and phenylalanine

Our study strengthens the hypothesis that GFRP functions as a scaffolding protein that stabilizes the active or inactive conformations of the GCH1 decamer by direct GFRP-GCH1 interactions and by enhancing the binding affinity of allosteric inhibitors. This notion fits well with the relatively small effects of GFRP on enzyme kinetics and the conformational rearrangements. GCH1 alone can be fully inhibited by allosteric inhibitors. In presence of GFRP, the K_i of allosteric inhibitors is decreased by a factor of 10 [135]. Binding of GFRP does not change the overall conformation of GCH1 significantly as found in the presence of allosteric inhibitors. On the stimulatory branch, from enzyme kinetics we know that GFRP-Phe merely reduces the positive cooperativity of GCH1 and, as a result, slightly stimulates the enzyme's activity in the presence of sub-saturating concentrations of GTP without an effect on V_{max} [3, 6] [35, 36]. Comparison of the inhibitory GCH1-GFRP-BH4 complex with allosterically inhibited GCH1 shows that binding of GFRP does not change the overall conformation of GCH1 significantly. Concerning GCH1 stimulation by GFRP, from enzyme kinetics we know that GFRP-Phe merely reduces the positive cooperativity of GCH1 and, as a result, slightly stimulates the enzyme's activity in the presence of sub-saturating concentrations of GTP without an effect on V_{max} [35, 36]. Again, conformational changes of the catalytically active GCH1 decamer between active GCH1 and the stimulatory GCH1-GFRP-Phe complex are small. GFRP seems to help to stabilize the active conformation in each of the ten individual active sites of GCH1, thereby reducing the cooperativity between the active sites and allowing for independent binding of substrate. Although the effects of GFRP on the GCH1 activity appear to be small in terms of enzyme kinetics and structural rearrangements, it has dramatic effects on the response of GCH1 to physiological concentrations of effector molecules BH4 and phenylalanine

as originally described by Harada et al. [35]. In fact, continuous variation of tetrahydrobiopterin and phenylalanine concentration in the cellular milieu allows dynamic formation of stimulatory and inhibitory complexes and thus dynamic allosteric regulation of the cellular biopterin homeostasis.

4.8 Allosteric inhibition of GCH1-GFRP does not alter substrate recognition

High resolution crystal structures of the human stimulatory and inhibitory GCH1-GFRP complexes, each in the liganded and unliganded state, reveal that the substrate analogue 7-deaza-GTP binds to both stimulatory and the inhibitory complexes and adopts an identical binding mode. Structural differences in the catalytically relevant residues are negligible between both complex structures. Upon binding of substrate analogue both complexes undergo the same disorder-order transition in the F122-loop, which transitions from a disordered to a structurally well defined inward facing state and thereby shields the substrate and locks it in the active site. Based on their rat GCH1-GFRP structures, Maita et al. postulate that the inhibitory regulation is controlled by two defined conformations of the F122 loop. In the inhibitory state, the F122 loop is claimed to have an open conformation, while it is in a closed state in the stimulatory complex [65]. Furthermore, they observed that in the inhibitory complex the side chain of Leu154/165 (rat and human sequence numbering) is shifted towards the active site, thereby decreasing the depth of the GTP binding pocket. Taking these observations together the authors suggest that the reasons for the reduced GCH1 activity in the inhibitory complex is due to the fact that the guanosine base of the substrate GTP cannot be positioned in the correct orientation in the active site. Our human GCH1-GFRP crystal structures demonstrate that the mode of substrate binding to the inhibitory complex is identical to that to the active enzyme. Furthermore, the topology of the active site pocket and the conformation of the catalytically relevant residues do not differ. This leads us to conclude that the reduced enzyme activity of the inhibitory complex cannot be explained by the inability of binding the substrate. Additionally, both complexes seem to allow for closure of the active site upon substrate binding by conversion of F122 loop from a flexible state to an ordered closed conformation.

These observations are consistent with the postulation that the substrate affinity of the stimulated and inhibited complexes are very similar and rather the binding kinetics of the substrate is accelerated in the inhibited enzyme, which reduces the residence time of the substrate and precludes conversion to product [21]. This is probably mainly caused by BH4 induced compression and rigidification of the GCH1 central core, which affects the kinetics of the order-disorder transitions of peripheral regions, such as the F122 loop.

4.9 Combination of cryo-EM and Xray structures help to develop a model of allosteric inhibition

We describe here a comprehensive structural study of allosteric regulation of GCH1 and determined two structures of human GCH1-GRFP complexes by cryo-EM. One structure comprises the substrate bound, allosterically stimulated form of the GCH1-GRFP complex, the other the allosterically inhibited, substrate free form. Further, we describe a series of crystallographically determined structures of basally active, non-regulated and allosterically inhibited GCH1. All structures combined show different aspects of allosteric regulation in unprecedented complexity and detail. From the numerous structures and different functional and biophysical experiments a model for the allosteric regulation of GCH1 can be developed. To enable the binding of BH4 and coordinate the allosteric inhibitor at the interface of two monomers, the residues R235 and R241 change position and trigger large movements in region C, which include displacement of the central α -helix and change in β -barrel curvature. These rearrangements in a concerted fashion first lead to the shrinking of the central 5 helix bundle of the functional oligomer and to a reduction of the β -barrel radius. Secondly, they induce conformational changes in the neighboring subunit, which include displacement of H126 and E128 and formation of a salt bridge between D127 and R235 and thereby repositioning of D127. This altered conformation in residues 126-128 changes the dynamics of the N-terminally preceding residues 115-125. Loop 115-130 (region A) is the only direct connection between the allosteric and the active site and therefore functions as a transmitter of the allosteric signal. In the experimental structures, it transitions from a tight, stable and closed conformation for the substrate bound stimulated

GCH1, via a more flexible, yet conformationally restrained state in active, substrate-free GCH1 to a state of enhanced flexibility triggered by BH4 binding. Thus two distinct but concerted structural rearrangements occur upon inhibitor binding to the allosteric site, which lead to (1) increased rigidity and decreased mobility in the protein center and (2) enhanced flexibility at the peripheral region A in proximity to the active site. The loosening of the loop structure results in a protein structure that is held in a conformational state that exhibits a distinctly more accessible active site compared to the active state. The absence of any catalytic activity of GCH1 mutant F122A provides further evidence that the nature of the side chain of residue F122, the F122 loop and region A play a major role in determining enzyme activity.

Our data therefore extend the more simplistic postulate by Maita et al. [65], who proposed a transition of a closed, active to an open, inactive conformation upon allosteric inhibition. In contrast, we unambiguously show that disorder-order transitions and changes in the degree of flexibility of the signal transducing structural element of region A occur, which differentiate active from inactive GCH1. Further, Maita et al. proposed steric hindrance of substrate binding to be the ultimate cause for the loss of enzymatic activity, while we could clearly show that substrate binding is not at all compromised and the binding site geometry is unchanged between active and inhibited states.

4.10 Novel dissociation rate controlled allosteric inhibition of GCH1

The observed structural features are strongly reminiscent of the classical models of Monod, Wyman, and Changeux [79] and Koshland, Nemethy, and Filmer [49] of allosteric regulation. These models describe the transition from a rigid, tense (T), less active state with low affinity for the ligand, to a mobile, relaxed (R) high affinity state [78]. More recently, based on experimental data on structure, protein dynamics and thermodynamics, more complex descriptions for allostery have been developed [80, 19]. The largely qualitative, static images of end point protein structures have been replaced by more quantitative, dynamic views of allostery, which, unlike static structural models, are more difficult to describe. Allosteric mechanisms can include

intrinsic disorder and local unfolding [29], remodeling of the energy landscape or can work without any conformational change [17]. We show here that in allosterically inhibited GCH1 substrate binding is not sterically hindered but occurs with similar affinities to the active states of the enzyme. This finding suggests a mechanism of non-competitive inhibition for GCH1. However, since we do not observe any structural differences of residues relevant for substrate turnover between active and inactive GCH1 and in fact all catalytically relevant residues are identical in position and poised for substrate conversion, it remains unclear why substrate would not be turned over by the inhibited state. We conclude that BH4-induced inhibition of GCH1 must be triggered by another, non-affinity-driven mechanism and propose here a novel mechanism of allosteric regulation that involves accelerated substrate binding kinetics. In this model, inhibition is caused by 'dissociation before turnover' which in turn requires that the residence time of substrate in the active site of the enzyme is shorter than the time required for initiation of substrate conversion.

GCH1 is a very tardy enzyme and conversion of GTP to H2NTP proceeds extremely slow. Turnover rates were described for GCH1 from bacterial species and is in the range of 0.05 s^{-1} /subunit [10]. The initiating step of purine ring hydrolysis to the first reaction intermediate, 2,5-diamino-5-ribofuranosylamino-4(3H)-pyrimidinone-triphosphate (I1), commences at higher turnover rates of 5 s^{-1} , while the catalytic steps that occur later, Amadori rearrangement and dihydropyrazine ring closure, are rate limiting. Such slow turnover requires a minimum residence time of substrate in the active site of $>0.2 \text{ s}$ for formate and I1 formation and $>20 \text{ s}$ for product formation in order to provide sufficient time for catalysis to occur. Using a functional ^1H -NMR based assay that detects formate as the first reaction product of GCH1 we show that allosteric inhibition of GCH1 leads to complete abolishment of enzyme activity including the fast initial purine ring hydrolysis, suggesting that the relevant parameter for inhibition is the substrate residence time required for this conversion.

Michaelis constants have been determined for mammalian GCH1 to be in the two-digit micromolar range [35]. Using the substrate analog 7 deaza-GTP we determined K_D 's of approximately 100 and 600 μM for BH4-bound inhibited and free, active hGCH1. The slightly higher values for 7 deaza-GTP may be explained by the difference in molecular structure, ie. the replacement of the N7-atom by a

carbon atom. Assuming a substrate binding affinity of 100 μM and diffusion limited association rates ($10^6 \text{ M}^{-1} \text{ s}^{-1}$) an unrealistically high dissociation rate constant of 100 s^{-1} would be required, way too fast compared to the 5 s^{-1} rate required for purine ring hydrolysis. Therefore, it is more likely that substrate association occurs on a slower timescale ($\sim 10^4 \text{ M}^{-1} \text{ s}^{-1}$) by assuming that GTP folds slowly into the active site pocket of catalytically active GCH1 after rapid electrostatically driven triphosphate binding. Dissociation would then occur in the $\sim 1 \text{ s}^{-1}$ timescale. These slower binding kinetics would roughly correspond to the above described target range of residence times of $\sim 1 \text{ s}$ needed for the substrate conversion.

Here, we provided evidence for enhanced substrate dissociation rates in allosterically inhibited GCH1 using STD NMR data, which show a threefold STD response enhancement (A_{max} increase) for the allosterically inhibited form of GCH1 corresponding to an increase in dissociation rate constants by factors between 10 and 100-fold [3]. In the light of the required residence time of substrate in the GCH1 active site such an acceleration of substrate dissociation could thus lead to a switch between active and completely inactive states by reduction of the substrate residence time from $\sim 1 \text{ s}$ to ~ 0.01 to $\sim 0.1 \text{ s}$. We have further shown that the substrate analog 7-deaza-GTP binds in fact slightly more tightly to the allosterically inhibited GCH1 (factor of ~ 6). In order to satisfy thermodynamics, assuming acceleration of dissociation by factors of 10-100 requires that the corresponding association rates must increase by this factor multiplied by the increase in binding affinity, as such 60-600-fold. These effects on association and dissociation rates can be plausibly explained by our structural findings. Allosteric inhibition by BH4 leads to enhanced flexibility of region A, the F122-containing loop. The loop structure acts as a lid above the active site, which effectively traps GTP during its turnover and shields the reaction chamber from bulk solvent [65]. None of the residues in region A are directly involved in the catalysis or recognition of substrate. A change in the intrinsic flexibility of this lid region should have direct influence on substrate binding kinetics. The enhanced flexibility observed in the allosterically inhibited state will enable a faster formation of the GTP bound state of GCH1 and result in faster association rates. Likewise, faster dissociation rates are triggered by the higher tendency of the F122-loop to open up due to the less rigid attachment to neighboring amino acid stretches. Thus, the interpretation of our structural data

is consistent with the hypothesis that a strong acceleration of the association of substrate overcompensates the acceleration of the dissociation of substrate leading to the observed inverted binding affinities.

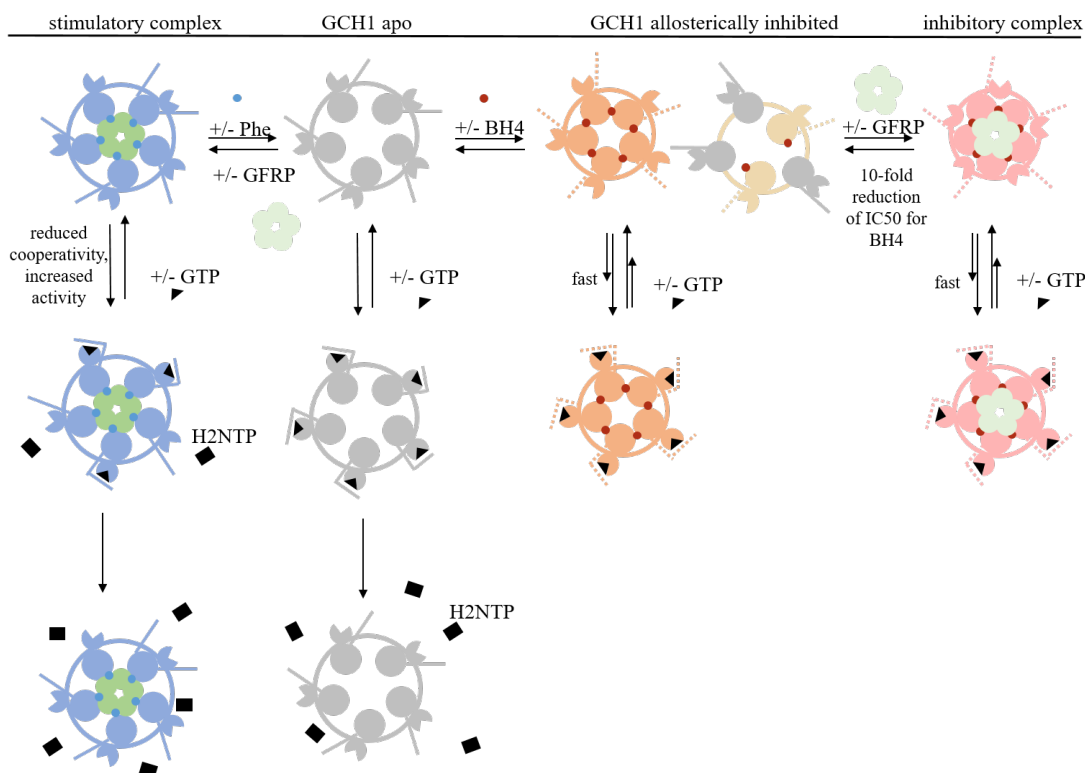


Figure 47: Schematic representation of proposed mechanism of allosteric regulation of GCH1: Schematic representation of distinct regulatory states of GCH1, namely non-regulated GVH1 (grey), inhibited GCH1 (orange), stimulated GCH1-GFRP complex (blue) and inhibited GCH1-GFRP complex (red).

The absence of activity of the F122A mutant may in part be explained by a similar mechanism. While we would not expect the mutant to trigger the same quaternary structural rearrangements observed for the allosterically inhibited enzyme, absence of the bulky aromatic side chain at the center of the lid loop will have similar effects on the accessibility of the active site and substrate binding kinetics, explaining the inability of this point mutant of GCH1 to generate product, while its substrate binding affinity is identical to the wild-type enzyme as shown here by ^1H , ^{13}C HMQC NMR. While negative allosteric modulators are generally believed to shift the equilibrium distribution of enzyme conformations to favor

a catalytically incompetent structure, the kinetics of conformational exchange or substrate binding is barely addressed in the literature. For IMP Dehydrogenase kinetic control of allosteric activation was described [98]. In this case the positive control functions via a > 65 fold increase of k_{cat} in presence of the effector molecule K^+ . Riera, T.V., et al. use the term ‘kinetic control’ to describe a change in enzyme kinetics and not for a regulation of the enzyme via altering the binding kinetics as it is used in this study [98]. Allosteric regulation by binding kinetic control as proposed here, triggered by an increase in the k_{cat} and driving the substrate residence time below the threshold of the turnover rate, is so far not described in literature.

4.11 Outlook and concluding words

This scientific work is the first to address the structural details of the human GCH1-GFRP complex. It is the combination of various methods that allows the GCH1 to be studied in unprecedented depth.

A highlight of this work is the experimentally well supported postulation that the enzymatic activity is not a result of hinderance of substrate binding, but rather a consequence of accelerated substrate binding kinetics. A similar kinetically controlled, mechanism of allosteric regulation has not yet been published to our knowledge and is therefore particularly important for the scientific community and the general understanding of allosteric enzymes.

This study characterizes the details of the GCH1-GFRP interaction and elucidates how effector molecules induce conformational changes in order to facilitate picomolar interaction of GCH1 and GFRP. We postulate that GFRP acts as a metabolic sensor, which increases the affinity of BH4, reduces the cooperativity of GCH1 and stabilizes the inhibitory and stimulatory conformation. BH4 and Phe hereby, act as molecular glues, which faccilitate high-affinity recognition of the two proteins.

In conclusion, this comprehensive structural and mechanistic study shows GCH1, GFRP and the GCH1-GFRP complexes in an ensemble of structures as well as biophysical experiments and thereby provides insights into the mechanism of allosteric regulation of GCH1 in unprecedented detail. Furthermore, the indentification of

positive and negative allosteric GCH1 modulators set promising milestones in the development of potential drugs to modulate GCH1 activity and thus BH4 levels in the cell. Since the BH4 pathway is currently perceived as an attractive target to treat pain disorders [53, 76, 116] with GCH1 being the target with human genetics validation, the understanding of the details of allosteric GCH1 inhibition as well as the methods used here will prove highly useful to develop potential drug candidates that selectively modulate its activity.

References

- [1] ACKERS, Gary K. ; DOYLE, Michael L. ; MYERS, David ; DAUGHERTY, Margaret A.: Molecular code for cooperativity in hemoglobin. In: *Science* 255 (1992), Nr. 5040, S. 54–63
- [2] AFONINE, Pavel V. ; POON, Billy K. ; READ, Randy J. ; SOBOLEV, Oleg V. ; TERWILLIGER, Thomas C. ; URZHUMTSEV, Alexandre ; ADAMS, Paul D.: Real-space refinement in PHENIX for cryo-EM and crystallography. In: *Acta Crystallographica Section D: Structural Biology* 74 (2018), Nr. 6, S. 531–544
- [3] ARETZ, Jonas ; RADEMACHER, Christoph: Ranking Hits From Saturation Transfer Difference Nuclear Magnetic Resonance–Based Fragment Screening. In: *Frontiers in chemistry* 7 (2019), S. 215
- [4] AUERBACH, G. ; HERRMANN, A. ; BRACHER, A. ; BADER, G. ; GUTLICH, M. ; FISCHER, M. ; NEUKAMM, M. ; GARRIDO-FRANCO, M. ; RICHARDSON, J. ; NAR, H. ; HUBER, R. ; BACHER, A.: Zinc plays a key role in human and bacterial GTP cyclohydrolase I. In: *Proc Natl Acad Sci U S A* 97 (2000), Nr. 25, S. 13567–72. – URL <https://www.ncbi.nlm.nih.gov/pubmed/11087827>. – ISSN 0027-8424 (Print) 0027-8424 (Linking)
- [5] AUERBACH, G. ; NAR, H.: The pathway from GTP to tetrahydrobiopterin: three-dimensional structures of GTP cyclohydrolase I and 6-pyruvoyl tetrahydropterin synthase. In: *Biol Chem* 378 (1997), Nr. 3-4, S. 185–92. – URL <https://www.ncbi.nlm.nih.gov/pubmed/9165069>. – ISSN 1431-6730 (Print) 1431-6730 (Linking)
- [6] BARAD, Benjamin A. ; ECHOLS, Nathaniel ; WANG, Ray Yu-Ruei ; CHENG, Yifan ; DIMAIO, Frank ; ADAMS, Paul D. ; FRASER, James S.: EMRinger: side chain–directed model and map validation for 3D cryo-electron microscopy. In: *Nature methods* 12 (2015), Nr. 10, S. 943–946
- [7] BATTYE, T. G. ; KONTOGIANNIS, L. ; JOHNSON, O. ; POWELL, H. R. ; LESLIE, A. G.: iMOSFLM: a new graphical interface for diffraction-image processing with MOSFLM. In: *Acta Crystallogr D Biol Crystallogr* 67 (2011), Nr. Pt

- 4, S. 271–81. – URL <http://www.ncbi.nlm.nih.gov/pubmed/21460445>. – ISSN 1399-0047 (Electronic) 0907-4449 (Linking)
- [8] BEPLER, Tristan ; MORIN, Andrew ; RAPP, Micah ; BRASCH, Julia ; SHAPIRO, Lawrence ; NOBLE, Alex J. ; BERGER, Bonnie: Positive-unlabeled convolutional neural networks for particle picking in cryo-electron micrographs. In: *Nature methods* (2019), S. 1–8
- [9] BRACHER, Andreas ; EISENREICH, Wolfgang ; SCHRAMEK, Nicholas ; RITZ, Harald ; GÖTZE, Eva ; HERRMANN, Anja ; GÜTLICH, Markus ; BACHER, Adelbert: Biosynthesis of pteridines NMR studies on the reaction mechanisms of GTP cyclohydrolase I, pyruvoyltetrahydropterin synthase, and sepiapterin reductase. In: *Journal of Biological Chemistry* 273 (1998), Nr. 43, S. 28132–28141
- [10] BRACHER, Andreas ; FISCHER, Markus ; EISENREICH, Wolfgang ; RITZ, Harald ; SCHRAMEK, Nicholas ; BOYLE, Peter ; GENTILI, Patrizia ; HUBER, Robert ; NAR, Herbert ; AUERBACH, Günter u. a.: Histidine 179 mutants of GTP cyclohydrolase I catalyze the formation of 2-amino-5-formylamino-6-ribofuranosylamino-4 (3H)-pyrimidinone triphosphate. In: *Journal of Biological Chemistry* 274 (1999), Nr. 24, S. 16727–16735
- [11] BUNKOCZI, G. ; ECHOLS, N. ; MCCOY, A. J. ; OEFFNER, R. D. ; ADAMS, P. D. ; READ, R. J.: Phaser.MRage: automated molecular replacement. In: *Acta Crystallogr D Biol Crystallogr* 69 (2013), Nr. Pt 11, S. 2276–86. – URL <https://www.ncbi.nlm.nih.gov/pubmed/24189240>. – ISSN 1399-0047 (Electronic) 0907-4449 (Linking)
- [12] BURG, Alan W. ; BROWN, Gene M.: The biosynthesis of folic acid VIII. Purification and properties of the enzyme that catalyzes the production of formate from carbon atom 8 of guanosine triphosphate. In: *Journal of Biological Chemistry* 243 (1968), Nr. 9, S. 2349–2358
- [13] CHARI, Ashwin ; HASELBACH, David ; KIRVES, Jan-Martin ; OHMER, Juer-gen ; PAKNIA, Elham ; FISCHER, Niels ; GANICHKIN, Oleg ; MÖLLER, Vanessa ; FRYE, Jeremiah J. ; PETZOLD, Georg u. a.: ProteoPlex: stability

- optimization of macromolecular complexes by sparse-matrix screening of chemical space. In: *Nature methods* 12 (2015), Nr. 9, S. 859–865
- [14] CHEN, James Z. ; GRIGORIEFF, Nikolaus: SIGNATURE: a single-particle selection system for molecular electron microscopy. In: *Journal of structural biology* 157 (2007), Nr. 1, S. 168–173
- [15] COLEMAN, John W.: Nitric oxide in immunity and inflammation. In: *International immunopharmacology* 1 (2001), Nr. 8, S. 1397–1406
- [16] CONG, Yao ; LUDTKE, Steven J.: Single particle analysis at high resolution. In: *Methods in enzymology* Bd. 482. Elsevier, 2010, S. 211–235
- [17] COOPER, A ; DRYDEN, DTF: Allostery without conformational change. In: *European Biophysics Journal* 11 (1984), Nr. 2, S. 103–109
- [18] COSTA, Tiago R. ; IGNATIOU, Athanasios ; ORLOVA, Elena V.: Structural analysis of protein complexes by cryo electron microscopy. In: *Bacterial Protein Secretion Systems*. Springer, 2017, S. 377–413
- [19] CUI, Qiang ; KARPLUS, Martin: Allostery and cooperativity revisited. In: *Protein science* 17 (2008), Nr. 8, S. 1295–1307
- [20] DU, J. ; WEI, N. ; XU, H. ; GE, Y. ; VASQUEZ-VIVAR, J. ; GUAN, T. ; OLDHAM, K. T. ; PRITCHARD, Jr. ; SHI, Y.: Identification and functional characterization of phosphorylation sites on GTP cyclohydrolase I. In: *Arterioscler Thromb Vasc Biol* 29 (2009), Nr. 12, S. 2161–8. – URL <https://www.ncbi.nlm.nih.gov/pubmed/19762783>. – ISSN 1524-4636 (Electronic) 1079-5642 (Linking)
- [21] EBENHOCH, Rebecca ; PRINZ, Simone ; KALTWASSER, Susann ; MILLS, Deryck J. ; MEINECKE, Robert ; RÜBBELKE, Martin ; REINERT, Dirk ; BAUER, Margit ; WEIXLER, Lisa ; ZEEB, Markus u. a.: A hybrid approach reveals the allosteric regulation of GTP cyclohydrolase I. In: *Proceedings of the National Academy of Sciences* (2020)

- [22] EL YACOUBI, B. ; BONNETT, S. ; ANDERSON, J. N. ; SWAIRJO, M. A. ; IWATA-REUYL, D. ; CRECY-LAGARD, V. de: Discovery of a new prokaryotic type I GTP cyclohydrolase family. In: *J Biol Chem* 281 (2006), Nr. 49, S. 37586–93. – URL <https://www.ncbi.nlm.nih.gov/pubmed/17032654>. – ISSN 0021-9258 (Print) 0021-9258 (Linking)
- [23] ELMLUND, Dominika ; ELMLUND, Hans: Cryogenic electron microscopy and single-particle analysis. In: *Annual review of biochemistry* 84 (2015), S. 499–517
- [24] EMSLEY, P. ; LOHKAMP, B. ; SCOTT, W. G. ; COWTAN, K.: Features and development of Coot. In: *Acta Crystallogr D Biol Crystallogr* 66 (2010), Nr. Pt 4, S. 486–501. – URL <https://www.ncbi.nlm.nih.gov/pubmed/20383002>. – ISSN 1399-0047 (Electronic) 0907-4449 (Linking)
- [25] ENGELHARDT, Harold ; BOLLSCHWEILER, Daniel: Cryo-Electron Microscopy of Extremely Halophilic Microbes. In: *Methods in Microbiology* Bd. 45. Elsevier, 2018, S. 323–354
- [26] EVANS, P.: Scaling and assessment of data quality. In: *Acta Crystallogr D Biol Crystallogr* 62 (2006), Nr. Pt 1, S. 72–82. – URL <http://www.ncbi.nlm.nih.gov/pubmed/16369096>. – ISSN 0907-4449 (Print) 0907-4449 (Linking)
- [27] EVANS, P.: Scaling and assessment of data quality. In: *Acta Crystallogr D Biol Crystallogr* 62 (2006), Nr. Pt 1, S. 72–82. – URL <http://www.ncbi.nlm.nih.gov/pubmed/16369096>. – ISSN 0907-4449 (Print) 0907-4449 (Linking)
- [28] FRIEDRICH, Heiner ; JONGH, Petra E. de ; VERKLEIJ, Arie J. ; JONG, Krijn P. de: Electron tomography for heterogeneous catalysts and related nanostructured materials. In: *Chemical reviews* 109 (2009), Nr. 5, S. 1613–1629
- [29] GARCIA-PINO, Abel ; BALASUBRAMANIAN, Sreeram ; WYNS, Lode ; GAZIT, Ehud ; DE GREVE, Henri ; MAGNUSON, Roy D. ; CHARLIER, Daniel ;

- NULAND, Nico A. van ; LORIS, Remy: Allostery and intrinsic disorder mediate transcription regulation by conditional cooperativity. In: *Cell* 142 (2010), Nr. 1, S. 101–111
- [30] GIACOVAZZO, Carmelo: *Fundamentals of crystallography*. 3rd. Oxford ; New York : Oxford University Press, 2011 (IUCr texts on crystallography). – xxi, 842 p. S. – ISBN 9780199573660 (pbk.) 0199573662 (pbk.) 9780199573653 (hbk.) 0199573654 (hbk.)
- [31] GODOY-RUIZ, Raquel ; GUO, Chenyun ; TUGARINOV, Vitali: Alanine methyl groups as NMR probes of molecular structure and dynamics in high-molecular-weight proteins. In: *Journal of the American Chemical Society* 132 (2010), Nr. 51, S. 18340–18350
- [32] GRÄWERT, Tobias ; FISCHER, Markus ; BACHER, Adelbert: Structures and reaction mechanisms of GTP cyclohydrolases. In: *IUBMB life* 65 (2013), Nr. 4, S. 310–322
- [33] GÜTLICH, Markus ; SCHOTT, Karin ; WERNER, Thomas ; BACHER, Adelbert ; ZIEGLER, Irmgard: Species and tissue specificity of mammalian GTP cyclohydrolase I messenger RNA. In: *Biochimica et Biophysica Acta (BBA)-Gene Structure and Expression* 1171 (1992), Nr. 2, S. 133–140
- [34] HAIDER, Maximilian ; UHLEMANN, Stephan ; SCHWAN, Eugen ; ROSE, Harald ; KABIUS, Bernd ; URBAN, Knut: Electron microscopy image enhanced. In: *Nature* 392 (1998), Nr. 6678, S. 768–769
- [35] HARADA, T. ; KAGAMIYAMA, H. ; HATAKEYAMA, K.: Feedback regulation mechanisms for the control of GTP cyclohydrolase I activity. In: *Science* 260 (1993), Nr. 5113, S. 1507–10. – URL <https://www.ncbi.nlm.nih.gov/pubmed/8502995>. – ISSN 0036-8075 (Print) 0036-8075 (Linking)
- [36] HATAKEYAMA, K. ; HARADA, T. ; SUZUKI, S. ; WATANABE, Y. ; KAGAMIYAMA, H.: Purification and characterization of rat liver GTP cyclohydrolase I. Cooperative binding of GTP to the enzyme.

- In: *J Biol Chem* 264 (1989), Nr. 36, S. 21660–4. – URL <https://www.ncbi.nlm.nih.gov/pubmed/2557335>. – ISSN 0021-9258 (Print) 0021-9258 (Linking)
- [37] HEEL, Marin van ; HARAUZ, George: Resolution criteria for three dimensional reconstruction. In: *Optik (Stuttgart)* 73 (1986), Nr. 3, S. 119–122
- [38] HENDERSON, Richard ; BALDWIN, Joyce M. ; CESKA, Thomas A. ; ZEMLIN, Friedrich ; BECKMANN, Erich ; DOWNING, Kenneth H.: Model for the structure of bacteriorhodopsin based on high-resolution electron cryo-microscopy. In: *Journal of molecular biology* 213 (1990), Nr. 4, S. 899–929
- [39] HENDERSON, Richard ; SALI, Andrej ; BAKER, Matthew L. ; CARRAGHER, Bridget ; DEVKOTA, Batsal ; DOWNING, Kenneth H. ; EGELMAN, Edward H. ; FENG, Zukang ; FRANK, Joachim ; GRIGORIEFF, Nikolaus u. a.: Outcome of the first electron microscopy validation task force meeting. In: *Structure* 20 (2012), Nr. 2, S. 205–214
- [40] HENDERSON, Richard ; UNWIN, P Nigel T.: Three-dimensional model of purple membrane obtained by electron microscopy. In: *Nature* 257 (1975), Nr. 5521, S. 28–32
- [41] HIGGINS, C. E. ; GROSS, S. S.: The N-terminal peptide of mammalian GTP cyclohydrolase I is an autoinhibitory control element and contributes to binding the allosteric regulatory protein GFRP. In: *J Biol Chem* 286 (2011), Nr. 14, S. 11919–28. – URL <https://www.ncbi.nlm.nih.gov/pubmed/21163945>. – ISSN 1083-351X (Electronic) 0021-9258 (Linking)
- [42] HUSSEIN, D. ; STARR, A. ; HEIKAL, L. ; MCNEILL, E. ; CHANNON, K. M. ; BROWN, P. R. ; SUTTON, B. J. ; MCDONNELL, J. M. ; NANDI, M.: Validating the GTP-cyclohydrolase 1-feedback regulatory complex as a therapeutic target using biophysical and in vivo approaches. In: *Br J Pharmacol* 172 (2015), Nr. 16, S. 4146–57. – URL <https://www.ncbi.nlm.nih.gov/pubmed/26014146>. – ISSN 1476-5381 (Electronic) 0007-1188 (Linking)

- [43] HWANG, Tsang-Lin ; SHAKA, AJ: Water suppression that works. Excitation sculpting using arbitrary waveforms and pulsed field gradients. In: *Journal of magnetic resonance. Series A (Print)* 112 (1995), Nr. 2, S. 275–279
- [44] ICHINOSE, Hiroshi ; OHYE, Tamae ; TAKAHASHI, Ei-ichi ; SEKI, Naohiko ; HORI, Tada-aki ; SEGAWA, Masaya ; NOMURA, Yoshiko ; ENDO, Kotaro ; TANAKA, Hajime ; TSUJI, Shoji u. a.: Hereditary progressive dystonia with marked diurnal fluctuation caused by mutations in the GTP cyclohydrolase I gene. In: *Nature genetics* 8 (1994), Nr. 3, S. 236–242
- [45] KABSCH, W.: Xds. In: *Acta Crystallogr D Biol Crystallogr* 66 (2010), Nr. Pt 2, S. 125–32. – URL <http://www.ncbi.nlm.nih.gov/pubmed/20124692>. – ISSN 1399-0047 (Electronic) 0907-4449 (Linking)
- [46] KAUFMAN, Seymour: Properties of the pterin-dependent aromatic amino acid hydroxylases. In: *Aromatic amino acids in the brain* (1974), S. 85–108
- [47] KAUFMAN, Seymour ; LEVENBERG, Bruce: Further studies on the phenylalanine-hydroxylation cofactor. In: *J Biol Chem* 234 (1959), Nr. 10, S. 2683–2688
- [48] KIDOKORO, K. ; SATOH, M. ; CHANNON, K. M. ; YADA, T. ; SASAKI, T. ; KASHIHARA, N.: Maintenance of endothelial guanosine triphosphate cyclohydrolase I ameliorates diabetic nephropathy. In: *J Am Soc Nephrol* 24 (2013), Nr. 7, S. 1139–50. – URL <https://www.ncbi.nlm.nih.gov/pubmed/23620395>. – ISSN 1533-3450 (Electronic) 1046-6673 (Linking)
- [49] KOSHLAND JR, DE ; NEMETHY, G ; FILMER, D.: Comparison of experimental binding data and theoretical models in proteins containing subunits. In: *Biochemistry* 5 (1966), Nr. 1, S. 365–385
- [50] KRISSINEL, Evgeny ; HENRICK, Kim: Inference of macromolecular assemblies from crystalline state. In: *Journal of molecular biology* 372 (2007), Nr. 3, S. 774–797

- [51] KWON, N S. ; NATHAN, CF ; STUEHR, DJ: Reduced biopterin as a cofactor in the generation of nitrogen oxides by murine macrophages. In: *Journal of Biological Chemistry* 264 (1989), Nr. 34, S. 20496–20501
- [52] LANGLOIS, Robert ; PALLESEN, Jesper ; FRANK, Joachim: Reference-free particle selection enhanced with semi-supervised machine learning for cryo-electron microscopy. In: *Journal of structural biology* 175 (2011), Nr. 3, S. 353–361
- [53] LATREMOLIERE, A. ; COSTIGAN, M.: GCH1, BH4 and pain. In: *Curr Pharm Biotechnol* 12 (2011), Nr. 10, S. 1728–41. – URL <https://www.ncbi.nlm.nih.gov/pubmed/21466440>. – ISSN 1873-4316 (Electronic) 1389-2010 (Linking)
- [54] LATREMOLIERE, Alban ; COSTIGAN, Michael: GCH1, BH4 and pain. In: *Current pharmaceutical biotechnology* 12 (2011), Nr. 10, S. 1728–1741
- [55] LENZ, F: Fourier electron optics. In: *Electron Microscopy and Analysis*. Institute of Physics London, 1971, S. 224–229
- [56] LEPRE, Christopher A. ; MOORE, Jonathan M. ; PENG, Jeffrey W.: Theory and applications of NMR-based screening in pharmaceutical research. In: *Chemical reviews* 104 (2004), Nr. 8, S. 3641–3676
- [57] LI, L. ; REZVAN, A. ; SALERNO, J. C. ; HUSAIN, A. ; KWON, K. ; JO, H. ; HARRISON, D. G. ; CHEN, W.: GTP cyclohydrolase I phosphorylation and interaction with GTP cyclohydrolase feedback regulatory protein provide novel regulation of endothelial tetrahydrobiopterin and nitric oxide. In: *Circ Res* 106 (2010), Nr. 2, S. 328–36. – URL <https://www.ncbi.nlm.nih.gov/pubmed/19926872>. – ISSN 1524-4571 (Electronic) 0009-7330 (Linking)
- [58] LI, Li ; REZVAN, Amir ; SALERNO, John C. ; HUSAIN, Ahsan ; KWON, Kihwan ; JO, Hanjoong ; HARRISON, David G. ; CHEN, Wei: GTP cyclohydrolase I phosphorylation and interaction with GTP cyclohydrolase feedback regulatory protein provide novel regulation of endothelial tetrahydrobiopterin and nitric oxide. In: *Circulation research* 106 (2010), Nr. 2, S. 328–336

- [59] LI, Xueming ; MOONEY, Paul ; ZHENG, Shawn ; BOOTH, Christopher R. ; BRAUNFELD, Michael B. ; GUBBENS, Sander ; AGARD, David A. ; CHENG, Yifan: Electron counting and beam-induced motion correction enable near-atomic-resolution single-particle cryo-EM. In: *Nature methods* 10 (2013), Nr. 6, S. 584–590
- [60] LI, Xueming ; ZHENG, Shawn Q. ; EGAMI, Kiyoshi ; AGARD, David A. ; CHENG, Yifan: Influence of electron dose rate on electron counting images recorded with the K2 camera. In: *Journal of structural biology* 184 (2013), Nr. 2, S. 251–260
- [61] LIU, Maili ; MAO, Xi-an ; YE, Chaohui ; HUANG, He ; NICHOLSON, Jeremy K. ; LINDON, John C.: Improved WATERGATE pulse sequences for solvent suppression in NMR spectroscopy. In: *Journal of Magnetic Resonance* 132 (1998), Nr. 1, S. 125–129
- [62] LONG, Fei ; VAGIN, Alexei A. ; YOUNG, Paul ; MURSHUDOV, Garib N.: BALBES: a molecular-replacement pipeline. In: *Acta Crystallographica Section D: Biological Crystallography* 64 (2008), Nr. 1, S. 125–132
- [63] LUDTKE, Steven J. ; BALDWIN, Philip R. ; CHIU, Wah: EMAN: semiautomated software for high-resolution single-particle reconstructions. In: *Journal of structural biology* 128 (1999), Nr. 1, S. 82–97
- [64] MAIER, Josef ; WITTER, Klaus ; GUTLICH, Markus ; ZIEGLER, Irmgard ; WERNER, Thomas ; NINNEMANN, Helga: Homology Cloning of GTP-Cyclohydrolase-I from Various Unrelated Eukaryotes by Reverse-Transcription Polymerase Chain-Reaction Using a General Set of Degenerate Primers. In: *Biochemical and biophysical research communications* 212 (1995), Nr. 2, S. 705–711
- [65] MAITA, N. ; HATAKEYAMA, K. ; OKADA, K. ; HAKOSHIMA, T.: Structural basis of biopterin-induced inhibition of GTP cyclohydrolase I by GFRP, its feedback regulatory protein. In: *J Biol Chem* 279 (2004), Nr. 49, S. 51534–40. – URL <https://www.ncbi.nlm.nih.gov/pubmed/15448133>. – ISSN 0021-9258 (Print) 0021-9258 (Linking)

- [66] MAITA, N. ; OKADA, K. ; HATAKEYAMA, K. ; HAKOSHIMA, T.: Crystal structure of the stimulatory complex of GTP cyclohydrolase I and its feedback regulatory protein GFRP. In: *Proc Natl Acad Sci U S A* 99 (2002), Nr. 3, S. 1212–7. – URL <https://www.ncbi.nlm.nih.gov/pubmed/11818540>. – ISSN 0027-8424 (Print) 0027-8424 (Linking)
- [67] MAITA, N. ; OKADA, K. ; HIROTSU, S. ; HATAKEYAMA, K. ; HAKOSHIMA, T.: Preparation and crystallization of the stimulatory and inhibitory complexes of GTP cyclohydrolase I and its feedback regulatory protein GFRP. In: *Acta Crystallogr D Biol Crystallogr* 57 (2001), Nr. Pt 8, S. 1153–6. – URL <https://www.ncbi.nlm.nih.gov/pubmed/11468403>. – ISSN 0907-4449 (Print) 0907-4449 (Linking)
- [68] MAYER, M. ; MEYER, B.: Group epitope mapping by saturation transfer difference NMR to identify segments of a ligand in direct contact with a protein receptor. In: *J Am Chem Soc* 123 (2001), Nr. 25, S. 6108–17. – URL <https://www.ncbi.nlm.nih.gov/pubmed/11414845>. – ISSN 0002-7863 (Print) 0002-7863 (Linking)
- [69] MAYER, Moriz ; MEYER, Bernd: Characterization of ligand binding by saturation transfer difference NMR spectroscopy. In: *Angewandte Chemie International Edition* 38 (1999), Nr. 12, S. 1784–1788
- [70] MAYER, Moriz ; MEYER, Bernd: Group epitope mapping by saturation transfer difference NMR to identify segments of a ligand in direct contact with a protein receptor. In: *Journal of the American Chemical Society* 123 (2001), Nr. 25, S. 6108–6117
- [71] MCLEOD, Robert A. ; KOWAL, Julia ; RINGLER, Philippe ; STAHLBERG, Henning: Robust image alignment for cryogenic transmission electron microscopy. In: *Journal of structural biology* 197 (2017), Nr. 3, S. 279–293
- [72] McMULLAN, G ; FARUQI, AR ; HENDERSON, R: Direct electron detectors. In: *Methods in enzymology* Bd. 579. Elsevier, 2016, S. 1–17
- [73] MEININGER, C. J. ; MARINOS, R. S. ; HATAKEYAMA, K. ; MARTINEZ-ZAGUILAN, R. ; ROJAS, J. D. ; KELLY, K. A. ; WU, G.: Impaired nitric oxide

production in coronary endothelial cells of the spontaneously diabetic BB rat is due to tetrahydrobiopterin deficiency. In: *Biochem J* 349 (2000), Nr. Pt 1, S. 353–6. – URL <https://www.ncbi.nlm.nih.gov/pubmed/10861247>. – ISSN 0264-6021 (Print) 0264-6021 (Linking)

- [74] MEYER, Bernd ; KLEIN, Jens ; MAYER, Moritz ; MEINECKE, Robert ; MÖLLER, H ; NEFFE, A ; SCHUSTER, O ; WÜLFKEN, Jan ; DING, Yili ; KNAIE, O u. a.: Saturation transfer difference NMR spectroscopy for identifying ligand epitopes and binding specificities. In: *Leucocyte trafficking*. Springer, 2004, S. 149–167
- [75] MEYER, J. T. ; SPARLING, B. A. ; MCCARTY, W. J. ; ZHANG, M. ; SOTO, M. ; SCHNEIDER, S. ; CHEN, H. ; ROBERTS, J. ; TAN, H. ; KORNECOOK, T. ; ANDREWS, P. ; KNUTSON, C. G.: Pharmacological assessment of sepiapterin reductase inhibition on tactile response in the rat. In: *J Pharmacol Exp Ther* (2019). – URL <https://www.ncbi.nlm.nih.gov/pubmed/31110114>. – ISSN 1521-0103 (Electronic) 0022-3565 (Linking)
- [76] MEYER, James T. ; SPARLING, Brian A. ; MCCARTY, William J. ; ZHANG, Maosheng ; SOTO, Marcus ; SCHNEIDER, Stephen ; CHEN, Hao ; ROBERTS, Jonathan ; TAN, Helming ; KORNECOOK, Thomas u. a.: Pharmacological assessment of sepiapterin reductase inhibition on tactile response in the rat. In: *Journal of Pharmacology and Experimental Therapeutics* 371 (2019), Nr. 2, S. 476–486
- [77] MICROSCOPYAUSTRALIA: *MyScope*. 2013. – URL <https://myscope.training/legacy/tem/introduction/>. – Zugriffsdatum: 2020-09-30
- [78] MIHAILESCU, Mihaela-Rita ; RUSSU, Irina M.: A signature of the T→ R transition in human hemoglobin. In: *Proceedings of the National Academy of Sciences* 98 (2001), Nr. 7, S. 3773–3777
- [79] MONOD, Jacque ; WYMAN, Jeffries ; CHANGEUX, Jean-Pierre: On the nature of allosteric transitions: a plausible model. In: *J Mol Biol* 12 (1965), Nr. 1, S. 88–118

- [80] MOTLAGH, Hesam N. ; WRABL, James O. ; LI, Jing ; HILSER, Vincent J.: The ensemble nature of allostery. In: *Nature* 508 (2014), Nr. 7496, S. 331–339
- [81] MUELLER, Peter: *Crystal structure refinement : a crystallographers guide to SHELXL*. Oxford ; New York : Oxford University Press, 2006 (IUCR texts on crystallography). – xvii, 213 p. S. – URL Publisher description <http://www.loc.gov/catdir/enhancements/fy0635/2006011794-d.html>. – ISBN 0198570767 (alk. paper) 9780198570769 (alk. paper)
- [82] NAGATSU, T. ; NAKASHIMA, A. ; ICHINOSE, H. ; KOBAYASHI, K.: Human tyrosine hydroxylase in Parkinson’s disease and in related disorders. In: *J Neural Transm (Vienna)* (2018). – URL <https://www.ncbi.nlm.nih.gov/pubmed/29995172>. – ISSN 1435-1463 (Electronic) 0300-9564 (Linking)
- [83] NAKANE, Takanori ; KOTECHEA, Abhay ; SENTE, Andrija ; MCMULLAN, Greg ; MASIULIS, Simonas ; BROWN, Patricia M. ; GRIGORAS, Ioana T. ; MALINAUSKAITE, Lina ; MALINAUSKAS, Tomas ; MIEHLING, Jonas u. a.: Single-particle cryo-EM at atomic resolution. In: *BioRxiv* (2020)
- [84] NAR, H. ; HUBER, R. ; AUERBACH, G. ; FISCHER, M. ; HOSL, C. ; RITZ, H. ; BRACHER, A. ; MEINING, W. ; EBERHARDT, S. ; BACHER, A.: Active site topology and reaction mechanism of GTP cyclohydro-lase I. In: *Proc Natl Acad Sci U S A* 92 (1995), Nr. 26, S. 12120–5. – URL <https://www.ncbi.nlm.nih.gov/pubmed/8618856>. – ISSN 0027-8424 (Print) 0027-8424 (Linking)
- [85] NAR, H. ; HUBER, R. ; HEIZMANN, C. W. ; THONY, B. ; BUR-GISSER, D.: Three-dimensional structure of 6-pyruvoyl tetrahy-dropterin synthase, an enzyme involved in tetrahydrobiopterin biosyn-thesis. In: *EMBO J* 13 (1994), Nr. 6, S. 1255–62. – URL <https://www.ncbi.nlm.nih.gov/pubmed/8137809>. – ISSN 0261-4189 (Print) 0261-4189 (Linking)
- [86] NAR, H. ; HUBER, R. ; MEINING, W. ; SCHMID, C. ; WEINKAUF, S. ; BACHER, A.: Atomic structure of GTP cyclohydro-lase I. In: *Structure* 3 (1995),

Nr. 5, S. 459–66. – URL <https://www.ncbi.nlm.nih.gov/pubmed/7663943>.
– ISSN 0969-2126 (Print) 0969-2126 (Linking)

- [87] NAR, Herbert: *GTP Cyclohydrolase I*. In: *Handbook of Metalloproteins*, American Cancer Society, 2006. – URL <https://onlinelibrary.wiley.com/doi/abs/10.1002/0470028637.met007>.
– ISBN 9780470028636
- [88] NG, J. T. ; DEKKER, C. ; REARDON, P. ; DELFT, F. von: Lessons from ten years of crystallization experiments at the SGC. In: *Acta Crystallogr D Struct Biol* 72 (2016), Nr. Pt 2, S. 224–35. – URL <http://www.ncbi.nlm.nih.gov/pubmed/26894670>. – ISSN 2059-7983 (Electronic) 2059-7983 (Linking)
- [89] NICHOL, Charles A. ; SMITH, Gary K. ; DUCH, David S.: Biosynthesis and metabolism of tetrahydrobiopterin and molybdopterin. In: *Annual review of biochemistry* 54 (1985), Nr. 1, S. 729–764
- [90] NICHOL, Charles A. ; SMITH, Gary K. ; DUCH, David S.: Biosynthesis and metabolism of tetrahydrobiopterin and molybdopterin. In: *Annual review of biochemistry* 54 (1985), Nr. 1, S. 729–764
- [91] NIEDERWIESER, A ; BLAU, N ; WANG, M ; JOLLER, P ; ATARES, M ; CARDESA-GARCIA, JGTP: GTP cyclohydrolase I deficiency, a new enzyme defect causing hyperphenylalaninemia with neopterin, biopterin, dopamine, and serotonin deficiencies and muscular hypotonia. In: *European journal of pediatrics* 141 (1984), Nr. 4, S. 208–214
- [92] PENCZEK, Pawel A.: Fundamentals of three-dimensional reconstruction from projections. In: *Methods in enzymology* Bd. 482. Elsevier, 2010, S. 1–33
- [93] PENCZEK, Pawel A.: Resolution measures in molecular electron microscopy. In: *Methods in enzymology* Bd. 482. Elsevier, 2010, S. 73–100
- [94] PENCZEK, Pawel A. ; GRASSUCCI, Robert A. ; FRANK, Joachim: The ribosome at improved resolution: new techniques for merging and orienta-

- tion refinement in 3D cryo-electron microscopy of biological particles. In: *Ultramicroscopy* 53 (1994), Nr. 3, S. 251–270
- [95] PIOTTO, Martial ; SAUDEK, Vladimir ; SKLENÁŘ, Vladimir: Gradient-tailored excitation for single-quantum NMR spectroscopy of aqueous solutions. In: *Journal of biomolecular NMR* 2 (1992), Nr. 6, S. 661–665
- [96] REBELO, J. ; AUERBACH, G. ; BADER, G. ; BRACHER, A. ; NAR, H. ; HOSL, C. ; SCHRAMEK, N. ; KAISER, J. ; BACHER, A. ; HUBER, R. ; FISCHER, M.: Biosynthesis of pteridines. Reaction mechanism of GTP cyclohydrolase I. In: *J Mol Biol* 326 (2003), Nr. 2, S. 503–16. – URL <https://www.ncbi.nlm.nih.gov/pubmed/12559918>. – ISSN 0022-2836 (Print) 0022-2836 (Linking)
- [97] REIMER, Ludwig: *Elektronenmikroskopische Untersuchungs-und Präparationsmethoden*. Springer-Verlag, 2013
- [98] RIERA, Thomas V. ; ZHENG, Lianqing ; JOSEPHINE, Helen R. ; MIN, Donghong ; YANG, Wei ; HEDSTROM, Lizbeth: Allosteric activation via kinetic control: potassium accelerates a conformational change in IMP dehydrogenase. In: *Biochemistry* 50 (2011), Nr. 39, S. 8508–8518
- [99] ROHOU, Alexis ; GRIGORIEFF, Nikolaus: CTFFIND4: Fast and accurate defocus estimation from electron micrographs. In: *Journal of structural biology* 192 (2015), Nr. 2, S. 216–221
- [100] ROSENTHAL, Peter B. ; HENDERSON, Richard: Optimal determination of particle orientation, absolute hand, and contrast loss in single-particle electron cryomicroscopy. In: *Journal of molecular biology* 333 (2003), Nr. 4, S. 721–745
- [101] RUPP, Bernhard: *Biomolecular crystallography : principles, practice, and application to structural biology*. New York : Garland Science, 2010. – xxi, 809 p. S. – ISBN 9780815340812 0815340818
- [102] SCHERES, Sjors H.: A Bayesian view on cryo-EM structure determination. In: *Journal of molecular biology* 415 (2012), Nr. 2, S. 406–418

- [103] SCHERF, Tali ; ANGLISTER, Jacob: A T1 rho-filtered two-dimensional transferred NOE spectrum for studying antibody interactions with peptide antigens. In: *Biophysical journal* 64 (1993), Nr. 3, S. 754
- [104] SCHRAMEK, Nicholas ; BRACHER, Andreas ; BACHER, Adelbert: Ring opening is not rate-limiting in the GTP cyclohydrolase I reaction. In: *Journal of Biological Chemistry* 276 (2001), Nr. 4, S. 2622–2626
- [105] SCHRAMEK, Nicholas ; BRACHER, Andreas ; FISCHER, Markus ; AUERBACH, Günter ; NAR, Herbert ; HUBER, Robert ; BACHER, Adelbert: Reaction mechanism of GTP cyclohydrolase I: single turnover experiments using a kinetically competent reaction intermediate. In: *Journal of molecular biology* 316 (2002), Nr. 3, S. 829–837
- [106] SHEN, Rong-Sen ; ALAM, Aftab ; ZHANG, Yixian: Human liver GTP cyclohydrolase I: purification and some properties. In: *Biochimie* 71 (1989), Nr. 3, S. 343–349
- [107] SMART, O. S. ; WOMACK, T. O. ; FLENSBURG, C. ; KELLER, P. ; PACIOREK, W. ; SHARFF, A. ; VONRHEIN, C. ; BRICOGNE, G.: Exploiting structure similarity in refinement: automated NCS and target-structure restraints in BUSTER. In: *Acta Crystallogr D Biol Crystallogr* 68 (2012), Nr. Pt 4, S. 368–80. – URL <https://www.ncbi.nlm.nih.gov/pubmed/22505257>. – ISSN 1399-0047 (Electronic) 0907-4449 (Linking)
- [108] STROES, E. ; KASTELEIN, J. ; COSENTINO, F. ; ERKELENS, W. ; WEVER, R. ; KOOMANS, H. ; LUSCHER, T. ; RABELINK, T.: Tetrahydrobiopterin restores endothelial function in hypercholesterolemia. In: *J Clin Invest* 99 (1997), Nr. 1, S. 41–6. – URL <https://www.ncbi.nlm.nih.gov/pubmed/9011574>. – ISSN 0021-9738 (Print) 0021-9738 (Linking)
- [109] SWANSON, LW ; SCHWIND, GA: A review of the cold-field electron cathode. In: *Advances in imaging and electron physics* 159 (2009), S. 63–100
- [110] SWICK, L. ; KAPATOS, G.: A yeast 2-hybrid analysis of human GTP cyclohydrolase I protein interactions. In: *J Neurochem* 97 (2006), Nr. 5,

S. 1447–55. – URL <https://www.ncbi.nlm.nih.gov/pubmed/16696853>. – ISSN 0022-3042 (Print) 0022-3042 (Linking)

- [111] TANAKA, Yoko ; NAKAGAWA, Noriko ; KURAMITSU, Seiki ; YOKOYAMA, Shigeyuki ; MASUI, Ryoji: Novel reaction mechanism of GTP cyclohydrolase I. High-resolution X-ray crystallography of *Thermus thermophilus* HB8 enzyme complexed with a transition state analogue, the 8-oxoguanine derivative. In: *Journal of biochemistry* 138 (2005), Nr. 3, S. 263–275
- [112] TAYEH, MA ; MARLETTA, MA: Macrophage oxidation of L-arginine to nitric oxide, nitrite, and nitrate. Tetrahydrobiopterin is required as a cofactor. In: *Journal of Biological Chemistry* 264 (1989), Nr. 33, S. 19654–19658
- [113] TAZAWA, Masahiro ; OHTSUKI, Masatsugu ; SUMI-ICHINOSE, Chiho ; SHIRAIISHI, Hiroaki ; KURODA, Risa ; HAGINO, Yasumichi ; NAKASHIMA, Shigeru ; NOZAWA, Yoshinori ; ICHINOSE, Hiroshi ; NAGATSU, Toshiharu u. a.: GTP cyclohydrolase I from *Tetrahymena pyriformis*: cloning of cDNA and expression. In: *Comparative Biochemistry and Physiology Part B: Biochemistry and Molecular Biology* 127 (2000), Nr. 1, S. 65–73
- [114] TEGEDER, I. ; COSTIGAN, M. ; GRIFFIN, R. S. ; ABELE, A. ; BELFER, I. ; SCHMIDT, H. ; EHNERT, C. ; NEJIM, J. ; MARIAN, C. ; SCHOLZ, J. ; WU, T. ; ALLCHORNE, A. ; DIATCHENKO, L. ; BINSHTOK, A. M. ; GOLDMAN, D. ; ADOLPH, J. ; SAMA, S. ; ATLAS, S. J. ; CARLEZON, W. A. ; PARSEGAN, A. ; LOTSCH, J. ; FILLINGIM, R. B. ; MAIXNER, W. ; GEISLINGER, G. ; MAX, M. B. ; WOOLF, C. J.: GTP cyclohydrolase and tetrahydrobiopterin regulate pain sensitivity and persistence. In: *Nat Med* 12 (2006), Nr. 11, S. 1269–77. – URL <https://www.ncbi.nlm.nih.gov/pubmed/17057711>. – ISSN 1078-8956 (Print) 1078-8956 (Linking)
- [115] TEGEDER, Irmgard ; COSTIGAN, Michael ; GRIFFIN, Robert S. ; ABELE, Andrea ; BELFER, Inna ; SCHMIDT, Helmut ; EHNERT, Corina ; NEJIM, Jemiel ; MARIAN, Claudiu ; SCHOLZ, Joachim u. a.: GTP cyclohydrolase and tetrahydrobiopterin regulate pain sensitivity and persistence. In: *Nature medicine* 12 (2006), Nr. 11, S. 1269–1277

- [116] TEGEDER, Irmgard ; COSTIGAN, Michael ; GRIFFIN, Robert S. ; ABELE, Andrea ; BELFER, Inna ; SCHMIDT, Helmut ; EHNERT, Corina ; NEJIM, Jemiel ; MARIAN, Claudiu ; SCHOLZ, Joachim u. a.: GTP cyclohydrolase and tetrahydrobiopterin regulate pain sensitivity and persistence. In: *Nature medicine* 12 (2006), Nr. 11, S. 1269–1277
- [117] TIE, L. ; CHEN, L. Y. ; CHEN, D. D. ; XIE, H. H. ; CHANNON, K. M. ; CHEN, A. F.: GTP cyclohydrolase I prevents diabetic-impaired endothelial progenitor cells and wound healing by suppressing oxidative stress/thrombospondin-1. In: *Am J Physiol Endocrinol Metab* 306 (2014), Nr. 10, S. E1120–31. – URL <https://www.ncbi.nlm.nih.gov/pubmed/24644242>. – ISSN 1522-1555 (Electronic) 0193-1849 (Linking)
- [118] TOGARI, Akifumi ; ARAI, Michitsugu ; MOGI, Makio ; KONDO, Ayami ; NAGATSU, Toshiharu: Coexpression of GTP cyclohydrolase I and inducible nitric oxide synthase mRNAs in mouse osteoblastic cells activated by proinflammatory cytokines. In: *FEBS letters* 428 (1998), Nr. 3, S. 212–216
- [119] VAN HEEL, Marin: Angular reconstitution: a posteriori assignment of projection directions for 3D reconstruction. In: *Ultramicroscopy* 21 (1987), Nr. 2, S. 111–123
- [120] VILAS, J. L. ; GOMEZ-BLANCO, J. ; CONESA, P. ; MELERO, R. ; ROSA-TREVIN, J. Miguel de la ; OTON, J. ; CUENCA, J. ; MARABINI, R. ; CARAZO, J. M. ; VARGAS, J. ; SORZANO, C. O. S.: MonoRes: Automatic and Accurate Estimation of Local Resolution for Electron Microscopy Maps. In: *Structure* 26 (2018), Nr. 2, S. 337–344 e4. – URL <https://www.ncbi.nlm.nih.gov/pubmed/29395788>. – ISSN 1878-4186 (Electronic) 0969-2126 (Linking)
- [121] VILAS, Jose L. ; GÓMEZ-BLANCO, Josué ; CONESA, Pablo ; MELERO, Roberto ; ROSA-TREVÍN, José M. de la ; OTÓN, Joaquin ; CUENCA, Jesús ; MARABINI, Roberto ; CARAZO, José M. ; VARGAS, Javier u. a.: MonoRes: automatic and accurate estimation of local resolution for electron microscopy maps. In: *Structure* 26 (2018), Nr. 2, S. 337–344

- [122] VONRHEIN, C. ; FLENSBURG, C. ; KELLER, P. ; SHARFF, A. ; SMART, O. ; PACIOREK, W. ; WOMACK, T. ; BRICOGNE, G.: Data processing and analysis with the autoPROC toolbox. In: *Acta Crystallogr D Biol Crystallogr* 67 (2011), Nr. Pt 4, S. 293–302. – URL <http://www.ncbi.nlm.nih.gov/pubmed/21460447>. – ISSN 1399-0047 (Electronic) 0907-4449 (Linking)
- [123] VOSS, NR ; YOSHIOKA, CK ; RADERMACHER, M ; POTTER, CS ; CARRAGHER, B: DoG Picker and TiltPicker: software tools to facilitate particle selection in single particle electron microscopy. In: *Journal of structural biology* 166 (2009), Nr. 2, S. 205–213
- [124] VRANKEN, Wim F. ; BOUCHER, Wayne ; STEVENS, Tim J. ; FOGH, Rasmus H. ; PAJON, Anne ; LLINAS, Miguel ; ULRICH, Eldon L. ; MARKLEY, John L. ; IONIDES, John ; LAUE, Ernest D.: The CCPN data model for NMR spectroscopy: development of a software pipeline. In: *Proteins: structure, function, and bioinformatics* 59 (2005), Nr. 4, S. 687–696
- [125] VULOVIC, M ; RIEGER, B ; VAN VLIET, LJ ; KOSTER, AJ ; RAVELLI, RBG: A toolkit for the characterization of CCD cameras for transmission electron microscopy. In: *Acta Crystallographica Section D: Biological Crystallography* 66 (2010), Nr. 1, S. 97–109
- [126] WEI, Chin-Chuan ; CRANE, Brian R. ; STUEHR, Dennis J.: Tetrahydrobiopterin radical enzymology. In: *Chemical reviews* 103 (2003), Nr. 6, S. 2365–2384
- [127] WEI, T. ; ZHAO, L. ; JIA, J. ; XIA, H. ; DU, Y. ; LIN, Q. ; LIN, X. ; YE, X. ; YAN, Z. ; GAO, H.: Metabonomic analysis of potential biomarkers and drug targets involved in diabetic nephropathy mice. In: *Sci Rep* 5 (2015), S. 11998. – URL <https://www.ncbi.nlm.nih.gov/pubmed/26149603>. – ISSN 2045-2322 (Electronic) 2045-2322 (Linking)
- [128] WIDDER, J. D. ; CHEN, W. ; LI, L. ; DIKALOV, S. ; THONY, B. ; HATAKEYAMA, K. ; HARRISON, D. G.: Regulation of tetrahydrobiopterin biosynthesis by shear stress. In: *Circ Res* 101 (2007), Nr. 8, S. 830–8.

- URL <https://www.ncbi.nlm.nih.gov/pubmed/17704208>. – ISSN 1524-4571 (Electronic) 0009-7330 (Linking)
- [129] WILLIAMS, Christopher J. ; HEADD, Jeffrey J. ; MORIARTY, Nigel W. ; PRISANT, Michael G. ; VIDEAU, Lizbeth L. ; DEIS, Lindsay N. ; VERMA, Vishal ; KEEDY, Daniel A. ; HINTZE, Bradley J. ; CHEN, Vincent B. u. a.: MolProbity: More and better reference data for improved all-atom structure validation. In: *Protein Science* 27 (2018), Nr. 1, S. 293–315
- [130] WOOTTON, John C.: Non-globular domains in protein sequences: automated segmentation using complexity measures. In: *Computers & chemistry* 18 (1994), Nr. 3, S. 269–285
- [131] YIM, JOHN J. ; BROWN, GENE M.: Characteristics of guanosine triphosphate cyclohydrolase I purified from *Escherichia coli*. In: *Journal of Biological Chemistry* 251 (1976), Nr. 16, S. 5087–5094
- [132] YONEYAMA, T. ; BREWER, J. M. ; HATAKEYAMA, K.: GTP cyclohydrolase I feedback regulatory protein is a pentamer of identical subunits. Purification, cDNA cloning, and bacterial expression. In: *J Biol Chem* 272 (1997), Nr. 15, S. 9690–6. – URL <https://www.ncbi.nlm.nih.gov/pubmed/9092499>. – ISSN 0021-9258 (Print) 0021-9258 (Linking)
- [133] YONEYAMA, T. ; HATAKEYAMA, K.: Decameric GTP cyclohydrolase I forms complexes with two pentameric GTP cyclohydrolase I feedback regulatory proteins in the presence of phenylalanine or of a combination of tetrahydrobiopterin and GTP. In: *J Biol Chem* 273 (1998), Nr. 32, S. 20102–8. – URL <https://www.ncbi.nlm.nih.gov/pubmed/9685352>. – ISSN 0021-9258 (Print) 0021-9258 (Linking)
- [134] YONEYAMA, T. ; HATAKEYAMA, K.: Ligand binding to the inhibitory and stimulatory GTP cyclohydrolase I/GTP cyclohydrolase I feedback regulatory protein complexes. In: *Protein Sci* 10 (2001), Nr. 4, S. 871–8. – URL <https://www.ncbi.nlm.nih.gov/pubmed/11274478>. – ISSN 0961-8368 (Print) 0961-8368 (Linking)

- [135] YONEYAMA, T. ; WILSON, L. M. ; HATAKEYAMA, K.: GTP cyclohydrolase I feedback regulatory protein-dependent and -independent inhibitors of GTP cyclohydrolase I. In: *Arch Biochem Biophys* 388 (2001), Nr. 1, S. 67–73. – URL <https://www.ncbi.nlm.nih.gov/pubmed/11361142>. – ISSN 0003-9861 (Print) 0003-9861 (Linking)
- [136] ZEMLIN, F ; WEISS, K ; SCHISKE, P ; KUNATH, W ; HERRMANN, K-H: Coma-free alignment of high resolution electron microscopes with the aid of optical diffractograms. In: *Ultramicroscopy* 3 (1978), S. 49–60
- [137] ZHANG, K.: *Gautomatch*. 2017. – URL <https://www2.mrc-lmb.cam.ac.uk/research/locally-developed-software/zhang-software> – Zugriffsdatum: 2020-08-11
- [138] ZHANG, Xing ; ZHOU, Z H.: Limiting factors in atomic resolution cryo electron microscopy: no simple tricks. In: *Journal of structural biology* 175 (2011), Nr. 3, S. 253–263
- [139] ZHENG, Shawn Q. ; PALOVCAK, Eugene ; ARMACHE, Jean-Paul ; VERBA, Kliment A. ; CHENG, Yifan ; AGARD, David A.: MotionCor2: anisotropic correction of beam-induced motion for improved cryo-electron microscopy. In: *Nature methods* 14 (2017), Nr. 4, S. 331–332
- [140] ZIVANOV, Jasenko ; NAKANE, Takanori ; FORSBERG, Björn O ; KIMANIUS, Dari ; HAGEN, Wim J. ; LINDAHL, Erik ; SCHERES, Sjors H.: New tools for automated high-resolution cryo-EM structure determination in RELION-3. In: *Elife* 7 (2018), S. e42166
- [141] ZOU, Xiaodong ; HOVMÖLLER, Sven ; OLEYNIKOV, Peter: *Electron crystallography: electron microscopy and electron diffraction*. Bd. 16. Oxford University Press, 2011

Appendices

Sequences of protein constructs

hGCH1- Δ 42-NHis

MGSHHHHHHSGENLYFQGRPEAKSAQPADGWKGERPRSEEDNELNLPNLAAAYSSILSSLGENPQRQGLL
KTPWRAASAMQFFTKGYQETISDVLNDAIFDEDHDEMVIKIDIDMFSMCEHHLVPFVGKVHIGYLPNKQV
LGLSKLARIVEIYSRRLQVQERLTKQIAVAITEALRPAGVGVVVEATHMCMVMRGVQKMNSKTVTSTMLG
VFREDPKTREEFLTLIRS

hGCH1-FL-NMBP

MKIEEGKLVIIWINGDKGYNGLAIEVGGKFEKDTGIKVTVEHPDKLEEKFPQVAATGDGPDIIFWAHDRFGG
YAQSGLLAEITPDKAFQDKLYPFTWDAVRYNGKLIAYPIAVEALSLEYNKDLLPNPPKTWEEIPALDKEL
KAKGKSALMFNLQEPYFTWPLIAADGGYAFKYENGGYDIKDVGVNAGAKAGLTFVLVDLIKHKHMNADTD
YSIAEAAFNKGETAMTINGPWAWSNIDTSKVNYGVTVLPTFKGQPSKPFVGVLSAGINAASPNKELAKEF
LENYLLTDEGLEAVNKDKPLGAVALKSYYEELAKDPRIAATMENAQKGEIMPNIQMSAFWYAVRTAVIN
AASGRQTVDEALKDAQTNSSSLGENLYFQGEKGPVRAPAEKPRGARCSNGFPERDPPRPGPSRPAEKPPR
PEAKSAQPADGWKGERPRSEEDNELNLPNLAAAYSSILSSLGENPQRQGLLKTPWRAASAMQFFTKGYQE
TISDVLNDAIFDEDHDEMVIKIDIDMFSMCEHHLVPFVGKVHIGYLPNKQVLGLSKLARIVEIYSRRLQV
QERLTKQIAVAITEALRPAGVGVVVEATHMCMVMRGVQKMNSKTVTSTMLGVFREDPKTREEFLTLIRS

hGFRP-FL-NHis

MGSSHHHHHSSGLVPRGSHMPYLLISTQIRMEVGPTVMGDEQSDPELMQHLGASKRRALGNNFYEYYVD
DPPRIVLDKLERRGFRVLSMTGVGQTLVWCLHKE

hGCH1-F122A- Δ 42-NHis

MGSHHHHHHSGENLYFQGRPEAKSAQPADGWKGERPRSEEDNELNLPNLAAAYSSILSSLGENPQRQGLL
KTPWRAASAMQFFTKGYQETISDVLNDAIADEDHDEMVIKIDIDMFSMCEHHLVPFVGKVHIGYLPNKQV
LGLSKLARIVEIYSRRLQVQERLTKQIAVAITEALRPAGVGVVVEATHMCMVMRGVQKMNSKTVTSTMLG
VFREDPKTREEFLTLIRS

hGCH1-R235A- Δ 42-NHis

MGSHHHHHHSGENLYFQGRPEAKSAQPADGWKGERPRSEEDNELNLPNLAAAYSSILSSLGENPQRQGLL

KTPWRAASAMQFFTKGYQETISDVLNDAIFDEDHDEMVIKIDIDMFSMCEHHLVPFVGKVHIGYLPNKQV
LGLSKLARIVEIYSRRLQVQERLTKQIAVAITEALRPAGVGVVVEATHMCMVMRGVQKMNSKTVTSTMLG
VFAEDPKTREEFLTLIRS

hGCH1-R241A- Δ 42-NHis

MGSHHHHHHSGENLYFQGRPEAKSAQPADGWKGERPRSEEDNELNLPNLAAAYSSILSSLGENPQRQGLL
KTPWRAASAMQFFTKGYQETISDVLNDAIFDEDHDEMVIKIDIDMFSMCEHHLVPFVGKVHIGYLPNKQV
LGLSKLARIVEIYSRRLQVQERLTKQIAVAITEALRPAGVGVVVEATHMCMVMRGVQKMNSKTVTSTMLG
VFREDPKTAEFLTLIRS

hGCH1-D127A- Δ 42-NHis

MGSHHHHHHSGENLYFQGRPEAKSAQPADGWKGERPRSEEDNELNLPNLAAAYSSILSSLGENPQRQGLL
KTPWRAASAMQFFTKGYQETISDVLNDAIFDEDHAEMVIKIDIDMFSMCEHHLVPFVGKVHIGYLPNKQV
LGLSKLARIVEIYSRRLQVQERLTKQIAVAITEALRPAGVGVVVEATHMCMVMRGVQKMNSKTVTSTMLG
VFREDPKTREEFLTLIRS

